

University of Alabama in Huntsville

**LOUIS**

---

Dissertations

UAH Electronic Theses and Dissertations

---

2012

## Numerical studies of supersonic jet impingement on a flat plate

Michael R. Brown

Follow this and additional works at: <https://louis.uah.edu/uah-dissertations>

---

### Recommended Citation

Brown, Michael R., "Numerical studies of supersonic jet impingement on a flat plate" (2012).

*Dissertations*. 308.

<https://louis.uah.edu/uah-dissertations/308>

This Dissertation is brought to you for free and open access by the UAH Electronic Theses and Dissertations at LOUIS. It has been accepted for inclusion in Dissertations by an authorized administrator of LOUIS.

**NUMERICAL STUDIES OF SUPERSONIC JET  
IMPINGEMENT ON A FLAT PLATE**

**by**

**MICHAEL R. BROWN**

**A DISSERTATION**

**Submitted in partial fulfillment of the requirements  
for the degree of Doctor Philosophy  
in  
The Department of Mechanical & Aerospace Engineering  
to  
The School of Graduate Studies  
of  
The University of Alabama in Huntsville**

**HUNTSVILLE, ALABAMA**

**2012**

In presenting this dissertation in partial fulfillment of the requirements for a doctoral degree from The University of Alabama in Huntsville, I agree that the Library of this University shall make it freely available for inspection. I further agree that permission for extensive copying for scholarly purposes may be granted by my advisor or, in his absence, by the Chair of the Department or the Dean of the School of Graduate Studies. It is also understood that due recognition shall be given to me and to The University of Alabama in Huntsville in any scholarly use which may be of any material in this dissertation.

Michael R Brown  
(student signature)

6/29/12  
(date)

## DISSERTATION APPROVAL FORM

Submitted by Michael R. Brown in partial fulfillment of the requirements for the degree of Doctor of Philosophy in Mechanical Engineering and accepted on behalf of the Faculty of the School of Graduate Studies by the dissertation committee.

We, the undersigned members of the Graduate Faculty of The University of Alabama in Huntsville, certify that we have advised and/or supervised the candidate on the work described in this dissertation. We further certify that we have reviewed the dissertation manuscript and approve it in partial fulfillment of the requirements of the degree of Doctor of Philosophy in Mechanical Engineering.

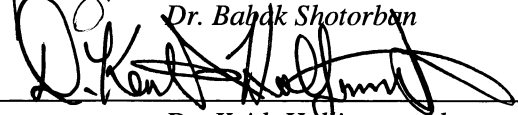
 6/29/12 Committee Chair  
Dr. Kader Frendi (Date)

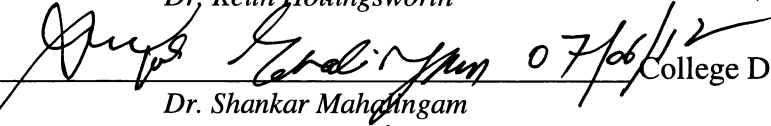
 7/5/12  
Dr. Hugh W. Coleman

 6/29/2012  
Dr. Sarma Rani

 7/5/12  
Dr. S. Ravindran

 6,29,2012  
Dr. Bahak Shotorban

 Department Chair  
Dr. Keith Hollingsworth

 07/06/12 College Dean  
Dr. Shankar Mahalingam

 8/3/12 Graduate Dean  
Dr. Rhonda Gaede

## **ABSTRACT**

The School of Graduate Studies

The University of Alabama in Huntsville

Degree: Doctor of Philosophy    College/Dept.: Engineering/Mechanical and  
Aerospace Engineering

Name of Candidate: Michael R. Brown

Title: Numerical Studies of Supersonic Jet Impingement on a Flat Plate

Numerical simulations of a supersonic air jet impinging on a flat plate are carried out using the Detached Eddy Simulation turbulence model. This study models an ideally expanded Mach 1.5 jet impinging normally on a large flat plate. The jet issues from a converging-diverging nozzle imbedded in a lift plate. The feedback mechanism between the impingement plate and the nozzle exit is identified and is observed to affect the shear layer as well as the jet core at the nozzle exit. The effects of nozzle geometry and separation distance between the nozzle exit and the impingement plate are investigated. Comparisons with test data show the CFD results to be in good agreement. The three impingement tones (L1, L2 and L3) observed in the tests are also predicted by the CFD results. Study of the nozzle to plate separation distance shows the impingement tone frequencies decrease as separation distance increases and some impingement tones become more or less dominant depending on the separation distance. The L3 tone is the

dominant tone for all three separation distances investigated. As the separation distance increases, the L2 tone becomes weaker while the L1 and L3 tones increase in magnitude. At the largest separation distance, the L2 tone also diminishes and the L3 tone becomes the dominant tone. The effect of nozzle geometry is seen to be very important in determining the prominence of certain impingement tones but does not significantly affect the overall sound pressure level. Normalized convection velocities of the shear layer disturbances are calculated to be  $U_c/U_{jet} = 0.54$  which is in good agreement with the test results of  $U_c/U_{jet} = 0.52$ . Acoustic environments on the impingement plate show little variation in spatial distribution with impingement distance and the peak overall sound pressure levels on the plate show negligible change with separation distance. Two-point space correlations of the pressure fluctuations on the impingement plate show strong correlation in the azimuth direction at distances away from the impingement point. Normalized convection velocities of the surface disturbances on the impingement plate,  $U_c/U_{jet}$ , are calculated using the two-point space-time correlations and the mean value is found to be  $U_c/U_{jet} = 0.47$ . The results of this study are in agreement with those in the open literature.

Abstract Approval: Committee Chair Kadel Fowl 6/29/12  
Department Chair [Signature] 7/6/2012  
Graduate Dean Rhonda Kay Saede 8/3/12

## **ACKNOWLEDGMENTS**

I would like to thank my advisor, Dr. Frendi for his patience and help through the years.

I would also like to thank Shawn Westmoreland for his guidance with grid generation and general OVERFLOW help. Post processing tools provided by him were invaluable to reducing the data in a timely manner. Finally, I would like to thank my family for their love, support and patience during my studies.

# TABLE OF CONTENTS

	Page
DISSERTATION APPROVAL FORM .....	iii
ACKNOWLEDGMENTS .....	vi
TABLE OF CONTENTS.....	vii
LIST OF FIGURES .....	ix
LIST OF TABLES .....	xii
LIST OF SYMBOLS .....	xiii
Chapter	
1. INTRODUCTION .....	1
1.1 Experimental Studies of Supersonic Jet Impingement.....	1
1.2 Numerical Studies of Supersonic Jet Impingement .....	9
2. MATHEMATICAL MODELS.....	14
2.1 DES Turbulence Model.....	14
3. METHOD OF SOLUTION .....	21
3.1 Computational Fluid Dynamics simulations .....	21
4. RESULTS AND DISCUSSION .....	26
4.1 Impinging Jet Geometry .....	26
4.2 Test Data Comparisons .....	30
4.3 Impingement Tone Analysis .....	39
4.4 OASPL and Sound Directivity .....	51
4.5 Feedback Mechanism .....	55



4.6 Resolved Turbulent Kinetic Energy .....	61
4.7 Jet Centerline Comparisons .....	63
4.8 Spatial SPL Distributions .....	65
4.9 Effects of Nozzle Geometry .....	71
4.10 Impingement Plate Environments .....	77
5. CONCLUSIONS.....	83
5.1 Effects of Nozzle and Plate Separation Distance .....	83
5.2 Effects of Nozzle Geometry .....	84
5.3 Feedback Mechanism Physics.....	85
5.4 Impingement Plate Environments .....	87
5.5 Recommendations for Further Study .....	87
6. REFERENCES .....	89
Appendix A.....	93

## LIST OF FIGURES

Figure	Page
4.1 Computational model.....	26
4.2 Comparison of test and modified nozzle geometries.....	28
4.3 Computational grid.....	29
4.4 Near-field pressure signal: $h/d=4$ .....	31
4.5 Comparison of near field sound pressure levels: $h/d=3.75$ .....	32
4.6 Comparison of near field sound pressure levels: $h/d=4$ .....	33
4.7 Comparison of near field sound pressure levels: $h/d=4.25$ .....	34
4.8 Effect of separation distance for measured sound pressure levels from test [10].....	36
4.9 Effect of separation distance for CFD calculated sound pressure levels.....	37
4.10 Contours of density gradient magnitude showing shear layer disturbances.....	38
4.11 Instantaneous convection velocities of shear layer vortical structures.....	39
4.12 Moving window in joint time-frequency analysis: $h/d=4$ near field pressure.....	40
4.13 Comparison of SPL tone magnitude for $h/d=4$ .....	41
4.14 Time variation of sound pressure levels: $h/d=4$ .....	43
4.15 SPL variation with time: $h/d=4$ .....	43
4.16 Comparison of impingement SPL tone magnitudes for $h/d=3.75$ .....	45
4.17 SPL variation with time: $h/d=3.75$ .....	46
4.18 Near field pressure for $h/d=3.75$ .....	46
4.19 Mach iso-surfaces colored by density showing the time variation of the initial shear layer instability in the jet: $h/d=3.75$ .....	47
4.20 Comparison of tone magnitude of SPL: $h/d=4.25$ .....	49
4.21 Near field pressure for $h/d=4.25$ .....	49

4.22	SPL variation with time: $h/d = 4.25$ .....	50
4.23	Mach=0.5 iso-surfaces colored by density showing asymmetry in the initial shear layer disturbance: $h/d=4.25$ .....	50
4.24	Separation distance comparison of OASPL distribution around nozzle exit: inner arc .....	51
4.25	Separation distance comparison of OASPL distribution around nozzle exit: outer arc .....	52
4.26	Separation distance comparison of OASPL distribution around impingement point: inner arc .....	52
4.27	Separation distance comparison of OASPL distribution around impingement point: outer arc .....	53
4.28	Comparison of OASPL contours for all separation distances .....	54
4.29	Top view of Mach=0.5 iso-surface colored by density showing disturbance propagation in the wall jet.....	55
4.30	Contours of density gradient showing acoustic wave interactions and shear layer disturbance growth: separation $h/d=4$ : (a) acoustic wave generated in impingement region; (b) propagation of acoustic wave toward nozzle exit; (c) acoustic wave reflection from lift plate; (d) acoustic wave generates a disturbance in the shear layer; (e) oncoming acoustic wave interacts with shear layer disturbance; (f) resulting amplified shear layer disturbance .....	58
4.31	Iso-surfaces of $Q=3000$ showing vortex structure in the shear layer.....	59
4.32	Contours of density gradient magnitude showing jet cone precession due to acoustic wave interaction.....	61
4.33	Comparison of resolved turbulent kinetic energy ( $m^2/sec^2$ ) for each separation distance .....	62
4.34	Effects of separation distance on jet centerline time-averaged velocities .....	64
4.35	Effects of separation distance on jet centerline time-averaged pressure .....	64
4.36	Effects of separation distance on time-averaged jet shock cell locations.....	65
4.37	Radial distribution of probe locations: $h/d=3.75$ .....	66
4.38	Jet radial SPL distribution at $x=47.6$ mm: $h/d=3.75$ .....	67
4.39	Radial distribution of probe locations: $h/d=4$ and $h/d=4.25$ .....	67

4.40	Jet radial SPL distribution at $x=50.8\text{mm}$ : $h/d=4$ .....	68
4.41	Jet radial SPL distribution at $x=54\text{mm}$ : $h/d=4.25$ .....	68
4.42	Monitor point distribution in axial direction for each separation distance.....	69
4.43	Axial SPL distribution at $r=24\text{mm}$ : $h/d=3.75$ .....	70
4.44	Axial SPL distribution at $r=26\text{mm}$ : $h/d=4$ .....	70
4.45	Axial SPL distribution at $r=28\text{mm}$ : $h/d=4.25$ .....	71
4.46	Comparison of test and modified nozzle with test data.....	73
4.47	SPL variation with time: modified nozzle.....	73
4.48	Comparison of OASPL distribution around the nozzle exit for test and modified nozzle geometries: inner arc.....	75
4.49	OASPL Comparison of OASPL distribution around the nozzle exit for test and modified nozzle geometries: outer arc.....	75
4.50	Comparison of OASPL distribution around the nozzle exit for test and modified nozzle geometries: inner arc.....	75
4.51	Comparison of OASPL distribution around the nozzle exit for test and modified nozzle geometries: outer arc.....	76
4.52	Comparison of OASPL contours $h/d=4$ (a) test geometry; (b) modified nozzle geometry.....	76
4.53	TKE comparison $h/d=4$ (a) modified nozzle; (b) test nozzle.....	77
4.54	OASPL on impingement plate: $h/d=3.75$ .....	78
4.55	OASPL on the impingement plate: $h/d=4$ .....	78
4.56	OASPL on the impingement plate: $h/d=4.25$ .....	79
4.57	Normalized two-point space correlation on impingement plate at reference point 9.6 cm from the impingement point: $h/d=4$ .....	80
4.58	Normalized space-time correlation on impingement plate at reference point 9.6 cm from the impingement point: $h/d=4$ .....	81
4.59	SPL on impingement plate at reference point 9.6 cm from the impingement point.....	81
4.60	Time averaged pressure distribution at impingement point.....	82

## LIST OF TABLES

4.1	Grid size for each case .....	29
4.2	Comparison of impigement tones $h/d=3.75$ .....	32
4.3	Comparison of impingement tones $h/d=4$ .....	33
4.4	Comparison of impigement tones $h/d=4.25$ .....	34

## LIST OF SYMBOLS

### Acronyms

CFD	Computational fluid dynamics
DES	Detached eddy simulation
DNS	Direct numerical simulation
LES	Large eddy simulation
NPR	Nozzle pressure ratio
OASPL	Overall sound pressure level
RANS	Reynolds averaged Navier Stokes
SPL	Sound pressure level
TKE	Turbulent kinetic energy
VTOL	Vertical take-off and landing

### Symbols

$a_1$	Turbulence model constant
$C_{DES}$	DES model coefficient
$C_{DESKE}$	k- $\epsilon$ DES coefficient
$C_{DESKW}$	k- $\omega$ DES coefficient
$C_\mu, C_{\epsilon 1}, C_{\epsilon 2}$	Turbulence model constants
$CD_{k\omega}$	Turbulence model parameter
$d$	Diameter
$E$	Internal energy
$F_1$	Blending factor for turbulence model

$h$	Nozzle height above impingement plate
$H$	Enthalpy
$k$	Turbulent kinetic energy
$L_t$	Turbulence length scale
$M$	Mach Number
$M_t$	Turbulent Mach number
$p$	Pressure
$Pr$	Prandtl number
$Pr_L$	Laminar Prandtl number
$Pr_t$	Turbulent Prandtl number
$P_k$	Production of turbulent kinetic energy
$Q$	Q criterion
$R$	Gas constant
$S_{ij}$	Rate of strain
$T$	Temperature
$t$	Time
$t^*$	Non-dimensional time
$u$	Velocity
$U_c$	Convection velocity
$U_j$	Jet exit velocity
$y$	Distance from wall
Greek Symbols	
$\beta, \beta^*, \beta_2$	Turbulence model constants

$\xi, \eta, \zeta$	Generalized coordinate directions
$\gamma$	Ratio of specific heats
$\delta_{ij}$	Kronecker delta
$\varepsilon$	Eddy dissipation rate
$\varepsilon_c$	Compressible eddy dissipation rate
$\theta$	Azimuth coordinate direction
$\kappa$	Thermal conductivity
$\lambda_2$	Turbulence model constant
$\mu$	Viscosity
$\mu_t$	Turbulent viscosity
$\nu_t$	Eddy viscosity
$\rho$	Density
$\sigma_\kappa$	Turbulent Schmidt number
$\tau$	Pseudo time
$\Omega$	Rate of rotation



# CHAPTER 1

## INTRODUCTION

Supersonic jet impingement on a plate is an important topic of research with the design of jet powered vertical take-off and landing (VTOL) aircraft. Research has focused on lift loss and acoustics of the impinging jet. Lift loss is the result of the jet entraining air which locally increases the velocity and lowers the local pressure under the aircraft. This has obvious implications for aircraft performance and safety. Acoustics of the supersonic impinging jet are also important since this may result in sonic fatigue for aircraft components and the landing platform in the case of aircraft carrier operations. The acoustic field may also adversely affect ground personnel and other critical systems.

### **1.1 Experimental Studies of Supersonic Jet Impingement**

Lamont and Hunt [1] investigated the flow structure of underexpanded turbulent jets impinging on a flat plate at various degrees of inclination. Schlieren images showed some oscillation in the shock wave at the surface of the plate. The oscillations were determined to be caused by the large, flat nozzle base which served as a reflective surface for the acoustic waves resulting in standing waves in the flow field. The oscillations were eliminated by acoustically insulating the nozzle base. Plate pressures for various plate separation distances showed a single peak pressure distribution on the plate for small separation distances ( $0.5 D$ ) and the development of a two peak distribution for separation distances between one and ten diameters. The pressure distribution on the plate once again became a single peak pressure distribution for a separation distance of

15 nozzle exit diameters. The conditions for the formation of separation bubble on the plate were also investigated. The shock cell location for an impinging jet does not change compared to a free jet. The formation of a separation bubble on the plate is dependent on the plate distance relative to the location of the free jet shock cell.

Ho and Nosseir [2] performed testing with turbulent impinging jets with high subsonic exit Mach numbers. Although these tests are for subsonic jets, the feedback mechanisms identified are relevant to supersonic impinging jets. Test data shows that for high subsonic speeds ( $M > 0.7$ ) and nozzle exit to plate separation distances of less than 7.5 exit diameters, the measured pressure signal on the plate has a sine shape indicating resonance. The source of the feedback mechanism was investigated. Cross correlations of data from pressure transducers in the near field show the feedback loops consist of coherent structures convected downstream at 0.62 times the exit velocity of the jet. The time delays identified in the cross correlation between two near field pressure transducers indicate the resonance is due to the low frequency coherent structures convected downstream rather than the high-frequency, small-scale turbulence. The upstream propagating pressure waves are generated by the jet impingement on the plate and travel at the ambient speed of sound with a near constant phase angle of  $32.5^\circ$  near the nozzle. The pressure waves travelling upstream excite the thin shear layer at the nozzle exit. The upstream and downstream travelling waves become phase locked at the nozzle exit so that self sustaining oscillations are maintained. Collective interaction in the jet shear layer causes the shear layer characteristic frequency to rapidly transition from high instability frequency to a low resonant frequency. Resonant frequency is seen to vary with nozzle to plate separation distance. Resonant frequency decreases with plate

separation distance until the next resonant frequency stage is reached resulting in an increase in resonant frequency.

Nosseir and Ho [3] examined the noise radiated by the jets studied in their previous work [2]. The near field pressure measurements showed the staging present in the previous plate measurements [2]. Cross correlations of the pressure data showed that the primary source of noise was the plate for a jet in resonance. A zero time delay is observed indicating that the impinging coherent structures are axisymmetric. A high frequency component is observed but it has a lower intensity compared to the plate source. When the jet is not in resonance, the high frequency component has a similar intensity as the plate source.

Krothapalli [4] investigated jet impingement for underexpanded choked jets from a rectangular nozzle. Observations showed the presence of two discrete tones that were identified as an impingement tone and a higher frequency screech tone that is typically associated with underexpanded jets. Staging behavior of the impingement tone was observed that depended on the ratio of jet height above the plate to the nozzle exit diameter. Oscillations in the impinging jet were seen and varied with nozzle pressure ratio and height of the nozzle exit above the plate. Data showed a feedback mechanism where acoustic waves at the impingement point travelled upstream toward the nozzle exit and induced instabilities in the shear layer.

Powell [5] investigated normal impingement of underexpanded, round sonic jets on various sizes of flat plates. Investigation of impingement tones on large plates looked at a normalized height to nozzle exit ratios between 0.75 and 7.0. Seven stages for impingement tones were identified in this height range and a feedback mechanism

postulated as the cause of the observed staging. Norum [6] investigated impingement of supersonic, rectangular jets on a flat plate and recorded staging behavior for the primary impingement tones for nozzle height to diameter ratios of 3 to 10. A rough model of the feedback mechanism was developed that was highly dependent on the estimated average convection velocity in the subsonic portion of the jet.

Tam and Ahuja [7] suggested that the feedback loop for the impingement tones is not external to the jet as put forth by Nosseir and Ho [2, 3]. Tam and Ahuja proposed that the waves travelling upstream from the plate to the nozzle exit are neutral waves with characteristics the same as Kelvin-Helmholtz instability waves. These waves propagate within the jet and close the feedback loop which produces the characteristic impingement tones. A vortex-sheet jet model was developed that predicts much of the jet behavior observed in impingement tests. The model shows that a subsonic, impinging jet has a limited range of Strouhal number waves that match the Kelvin-Helmholtz instability waves seen in jet flows. Axisymmetric feedback is within the narrow Strouhal number range while helical modes are outside this range. This matches test data showing only axisymmetric modes for impinging subsonic jets. The model also predicts the behavior seen in tests of no resonance generated impingement tones being produced by a cold jet with an exit Mach number less than 0.65. The model applied to supersonic jets shows the neutral waves existing in the jet but with the main part of the neutral wave outside the jet. The model predicts that the frequency matching between the Kelvin-Helmholtz instability waves and the neutral waves permits Strouhal numbers corresponding to both axisymmetric and helical jet modes.

Henderson and Powell [8] performed tests for normal impingement of an axisymmetric choked jet on a flat plate with nozzle height to exit diameter ratios of 0.5 to 10. Data analysis showed that these tones fell onto three parallel lines on a logarithmic plot and identified as L1, L2 and L3 tones. The L1 tones are symmetrical while the L2 and L3 tones are helical. Sudden jumps in the dominant tonal frequency were observed as the jet height above the plate was changed, however in some cases the other tones would still be present. It was shown that the feedback mechanism between the nozzle and the plate was responsible for this jump in dominant tone. As the nozzle to the plate distance was increased, additional wavelengths would appear which shifts the dominant impingement tone to different frequency. These jump locations are also the locations where the jet is most receptive to other modes of oscillation. Data also shows that at these jump points, the jet may oscillate between dominant tone modes. A reflector was also incorporated in the tests to alter the feedback mechanism and change the dominant tone for a given height. Based on the reflector location, the dominant tone could be suppressed.

Kuo and Dowling [9] investigated the shock oscillations for a moderately underexpanded jet impinging on a flat plate. They developed a linear stability theory to predict shock oscillation frequency and damping rate for a given nozzle to plate distance, nozzle pressure ratio and shock stand-off distance. The study finds that the shock oscillations result in pressure and entropy fluctuations in the stagnation region on the plate. The entropy fluctuations were determined to be a significant acoustic source. These acoustic waves propagate upstream and enhance the shock oscillation. Analysis

showed that stand-off shock locations corresponding to the free jet shock cell location resulted in shock oscillations.

Krothapalli, et. al. [10] performed studies of the acoustics of perfectly expanded and underexpanded supersonic axisymmetric jet impinging on a flat plate. Tests were performed using a lift plate with the nozzle imbedded in the plate such that the exit was flush with the bottom of the lift plate. Pressure data was taken on the lift plate to determine downward force on the plate as a function of nozzle exit height above the plate. Near field acoustic data was taken ten throat diameters from the nozzle exit. Data was taken for different nozzle exit distances above the impingement plate. Height to nozzle throat diameter ratios of 3.75, 4 and 4.25 were investigated. Nozzle pressure ratio (NPR) for the perfectly expanded cases was 3.7 while the NPR of the underexpanded cases was 5. Results of the study show that the lift loss increases as the separation distance between the nozzle exit and the ground plane decreases. This is driven by the increased entrainment velocities as the separation distance decreases. Data also show that the presence of the lift plate excites a screech tone that is not present without the lift plate. Comparisons with free jet acoustic data show that the presence of the ground plate increases the OASPL by 8 dB relative to a free jet. Jet impingement tones were seen in the acoustic data as well as the characteristic staging behavior. A feedback loop formula based on the measured convective velocities of the jet flow was applied and the results show good agreement with the appropriate phase lag however, the derivation of the appropriate phase lag could not be determined from data and was derived by using the value that provided the best fit with data. It was hypothesized that the phase lag was likely from a combination of the shock structure in the vicinity of the impingement point

and the excitation of the shear layer caused by acoustic waves reflected from the lift plate. Data also shows that the role of shock cells for the convective velocities and acoustic frequencies are negligible for perfectly expanded jets but become more important for highly underexpanded jets.

Alvi and Iyer [11] performed a follow-on study based on the same configuration in Krothapalli [10]. This study focused on flow field characteristics on the impingement plate. Measurements were made of the surface pressure distribution at the impingement region on the impingement plate. Schlieren images were also made to better understand the physics behind the formation of a stagnation bubble. PIV data was also used to quantify the properties of the resulting wall jet as a function of NPR and nozzle-plate separation distance.

Henderson [12] investigated the connection between flow structure and the production of tones for supersonic jet impingement on a square flat plate with the side dimension equal to 12 nozzle exit diameters. The supersonic jet was generated using a round, convergent nozzle and operating at underexpanded conditions with NPR ranging from 3.38 and 4.74. Comparisons are also made with the results of Krothapalli [10] and Henderson and Powell [8]. Underexpanded supersonic jets showed little sensitivity to the nozzle geometry and the test apparatus. The data exhibited the same L1 and L2 tones identified in Henderson and Powell [8]. Test data also show that some separation distances and nozzle pressure ratios do not produce impingement tones and are referred to as zones of silence. It was observed that the impingement tones for a large plate are associated with impulsive wave fronts produced when the plate stand-off shock collapses for a portion of the oscillation cycle. The Mach disk is also identified as a source of

noise for moderately and highly underexpanded jets. Impingement tones cease when a conical shock wave appears in the flow or when the first or second shock wave is in the same position as for the free jet. Some comparisons are made with Krothapalli [10] and although the data shows similar staging behavior, the results do not clearly show the presence of L1 or L2 tones like the underexpanded jets.

Henderson, Bridges and Wernet [13] performed experiments investigating underexpanded, supersonic jets impinging on a large flat plate. Nozzle exit to plate separation distances between one and five exit diameters at a nozzle pressure ratio of four were investigated. Data showed tests that produced impingement tones also produced oscillations in the recirculation zone in the subsonic region in front of the plate and oscillations in the peripheral supersonic flow near the plate. This caused periodic pulsing in the wall jet, creating an acoustic source at approximately 2.6 nozzle radii from jet centerline.

Guerra, Su and Freire [14] studied the evolution of the radial wall jet after jet impingement on the plate. The study focused on heat transfer on the plate, the applicability of the log-law approach to obtaining the skin friction on the plate and the development of new methods for obtaining skin friction.

Henderson, Bridges and Wernet [15] performed experiments investigating underexpanded, supersonic jets impinging on a large flat plate. Nozzle exit to plate separation distances between one and five exit diameters at a nozzle pressure ratio of four. Data confirmed the findings of previous tests with a similar configuration [13]. Analysis showed that the stability of the jet was dependent on the strength of the stand-off shock and the velocity gradient in front of it. Production of tones occurred when the



Mach number upstream of the stand-off shock is slightly greater than the fully expanded Mach number. The occurrences of zones of silence were consistent with previous analysis [13].

## **1.2 Numerical Studies of Supersonic Jet Impingement**

Lee and Hong [16] investigated supersonic jet impingement in relation to rocket plume interactions for vertical launch systems. Data from sub-scale small test motors were used to benchmark computational fluid dynamic (CFD) models for Euler calculations. Nozzle exit to ground distance from 0.5 exit diameters to 6 diameters were investigated. Results showed that oscillations of the plate stand-off shock produced large pressure fluctuations on the plate for a distance of three diameters but the fluctuations rapidly diminished as the height was increased to four diameters and beyond. Fourier analysis of the shock oscillations showed frequencies between 1 – 10 kHz. The peak mean pressure on the plate was achieved at a nozzle to plate distance of four diameters. At close distances ( $h=0.5D$ ) the pressure profile on the plate had a single peak at the center of the impingement zone but the pressure profile became a two peak distribution as the separation distance increased to three diameters. The study also showed the shock locations in the plume were dependent on the pressure ratio and independent of the nozzle exit height above the plate.

Dauplain, Cuenot and Gicquel [17] performed a numerical study of supersonic jet impingement on a flat plate. The model utilized large eddy simulation (LES) with a fixed Smagorinsky model to model a supersonic jet from a converging nozzle with an NPR of 4.03 impinging on a flat plate at a distance of 4.16 nozzle exit diameters. Grid

resolution studies were performed for three different refinement levels: 7.5 million, 16 million and 22 million cells. Comparisons were made between the CFD results to experimental data from Henderson, Bridges and Wernet [14]. Computed mean and fluctuating quantities showed good agreement with the data. Since the jet was from an underexpanded converging nozzle only a weak impingement tone was produced with most of the acoustics exhibiting a broadband noise.

Numerical studies of supersonic jet impingement were performed by Tsuboi, et al [18] for two-phase jets. The gas was modeled as inviscid with real gas effects included. Particles did not interact with each other and interacted with the gas through drag and heat transfer. The normal impingement calculations were performed with a two dimensional, cylindrically symmetric grid for a single phase jet. Normal impingement was investigated for separation distance to nozzle diameter ratios of 4.37, 6.1, and 7.85. The exit Mach number was 3.2 with a static pressure ratio of 1.3 at the nozzle exit resulting in an underexpanded jet. Qualitative comparisons with Schlieren images showed good agreement with the Euler calculation results. Oscillation of the plate stand-off shock was observed in the results as well as propagation of acoustic waves, however comparison between transient pressures on the ground plane were not possible since the test data was not high frequency.

Three dimensional Euler calculations were performed by Yaga et al [19] for circular and rectangular underexpanded jets impinging on a flat plate. Nozzle separation distances of  $h/d=2, 3,$  and  $4$  were investigated for the circular nozzle and separation distances of  $h/d= 2$  and  $3$  for the rectangular nozzle. Steady state temperature and pressure data were recorded on the impingement plate and compared to test data.

Comparisons of CFD calculated pressure on the plate to the test data showed good agreement with discrepancies attributed to uncertainties in the flow distribution at the nozzle exit in the tests and to viscous effects being neglected in the calculations. It was also observed that the temperature and pressure field in the impingement region on the plate were not symmetric for either the circular or rectangular jet. This was observed in both the tests and in the three-dimensional Euler calculations.

Kim and Park [20] performed unsteady, axisymmetric simulations of an underexpanded choked jet impinging on a flat plate. The study investigated the effects of nozzle pressure ratio and the separation distance between the nozzle exit and the impingement plate. Nozzle pressure ratio was varied between 2.3 and 4 and plate separation distance was varied between 2 and 4 exit diameters. The study reproduced the staging behavior with plate separation distance that has been observed in experimental investigations.

Hong and Jeon [21] investigated supersonic jet impingement on flat and complex surfaces. The main focus of the investigation was to test new computational algorithms for modeling supersonic jet impingement on a surface. The inviscid CFD simulations performed were three dimensional with a symmetry plane. Nozzle to plate separation distances of  $0.63d$  and  $2.6d$  were investigated for flat plates. All jets were moderately underexpanded with  $p_{exit}/p_{\infty} = 1.2$  and an exit Mach number of approximately 3.1. CFD results for steady state pressures on the plate compared well with experimental results for the same configuration. CFD predictions on the formation of a separation bubble at a separation distance of  $2.6d$  and the absence of a separation bubble at  $0.63d$  also agreed with experimental observations. Supersonic jet impingement on a complex surface was

also studied but the results did not match the test data. This was attributed to some geometric differences between the simulation and the test due to simplifications and aeroelastic effects that deformed the plate in the experiments.

Hu and Sittakavi [22] performed an unsteady LES analysis of supersonic jet impingement on a flat plate. High order schemes were employed in the analysis. Inviscid fluxes were discretized with a fifth-order WENO scheme, a sixth-order compact scheme was used for the viscous fluxes, third-order one sided schemes were used at the boundaries and an eighth order implicit filter was applied to remove numerical oscillations. Mostly qualitative results were presented with no comparison made with experimental results.

Lee, Hong and Park [23] investigated an underexpanded supersonic rocket plume impinging on a flat plate. The investigation was primarily concerned with predicting heating rates to be used to calculate the corresponding ablation on the plate in the impingement region. The motor chamber pressure was 1200 psi and the exit Mach number was 2.93. Three-dimensional, Navier-Stokes calculations were performed using two different CFD codes. Laminar and turbulent steady-state calculations were performed and compared to test data and an unsteady, laminar calculation. The results showed pressure oscillations in the impingement region on the plate that changed amplitude with the nozzle-to-plate separation distance. The unsteady characteristics of the impingement region were only of concern in the study for the effects on the accuracy of the heating rates predicted by the steady-state solution.

Based on the literature review there is a growing need to understand the flow physics and the acoustic environments generated by an impinging supersonic jet.

Therefore the current research effort is motivated by the lack of high fidelity, unsteady CFD solutions for an impinging supersonic jet. To this end using the experimental results of Krothapalli, et al [10], CFD simulations were performed using the same parameter space as the one given in [10] to investigate the various fluid dynamics and acoustic phenomena taking place. In particular the effect of the separation distance between the nozzle exit and the flat plate will be investigated. In addition, the near field acoustics will be obtained together with the surface pressure on the plate.

## **CHAPTER 2**

### **MATHEMATICAL MODELS**

#### **2.1 DES Turbulence Model**

The problem of interest in the current study is an unsteady flow involving a free shear layer with portions of wall-bounded flow. This unsteady flow field would ideally be modeled using Direct Numerical Simulation (DNS) or Large Eddy Simulation (LES). A DNS approach would capture all the turbulent scales while an LES approach would capture all the large turbulent scales with an isotropic model for all the scales not resolved on the grid. The Reynolds number of the flow make the necessary DNS grid resolution requirements too high to make DNS a practical approach in analyzing this problem. The Reynolds number and grid requirement of the free shear portion of the flow makes LES an attractive approach for analyzing the current problem, however the wall bounded portions of the flow pose a problem since the length scales in these regions would require a high mesh resolution to ensure that the isotropic turbulence assumption of the subgrid model is not violated.

The modeling approach used in this study was Detached Eddy Simulation (DES). DES is a hybrid Reynolds Averaged Navier Stokes (RANS)/LES model. As previously mentioned, the drawback of LES is the grid resolution required in wall bounded flows where the small scales must be resolved to get the proper physical behavior. In the DES model, RANS is used in the wall bounded regions while LES is used in the free shear regions. This approach is a compromise since RANS is not well suited to model an unsteady flow field since it cannot resolve multiple length scales and time averaging

tends to destroy time accuracy. The strength of RANS is in its ability to accurately model boundary layer flows. The DES model is ideally suited for flows where the free shear layer physics are the most dominant feature and the RANS approximations for wall boundary layers is sufficient. This allows the computational expense to be focused on the free shear region and not in the boundary layer.

Detached Eddy Simulation is usually implemented as a modification to an existing eddy viscosity turbulence model in a RANS framework. This approach solves the RANS turbulence model and then filters the results to determine the level of eddy viscosity in the solution of the Navier-Stokes equations [27]. In this study, the RANS turbulence model was Menter's Shear Stress Transport (SST) model. Menter's SST model blends the  $k-\omega$  turbulence model which is stable and gives good results for wall bounded flows with the  $k-\varepsilon$  model which generally gives good results for shear layer.

Instead of the traditional time averaged approach [24], the Favre averaged Navier-Stokes equations are used. Favre, or mass averaging, of a variable decomposes the variable into a Favre averaged mean and a turbulent fluctuation:

$$\Phi = \tilde{\Phi} + \Phi'' , \quad (2-1)$$

where:

$$\tilde{\Phi} = \frac{\overline{\rho\Phi}}{\bar{\rho}} \quad (2-2)$$

In Equation (2-2), the  $\overline{(\ast)}$  notation indicates ensemble averaging. Applying this decomposition to the Navier-Stokes conservation equation yields [25]:

$$\frac{\partial \bar{\rho}}{\partial t} + \frac{\partial}{\partial x_j} (\bar{\rho} \tilde{u}_j) = 0 \quad (2-3)$$

$$\frac{\partial}{\partial t} (\bar{\rho} \tilde{u}_i) + \frac{\partial}{\partial x_j} (\bar{\rho} \tilde{u}_j \tilde{u}_i) = -\frac{\partial \bar{p}}{\partial x_i} + \frac{\partial}{\partial x_j} \left[ (\mu + \mu_t) \left( \frac{\partial \tilde{u}_i}{\partial x_j} + \frac{\partial \tilde{u}_j}{\partial x_i} - \frac{2}{3} \mu \frac{\partial \tilde{u}_k}{\partial x_k} \delta_{ij} \right) \right] \quad (2-4)$$

$$\begin{aligned} \frac{\partial}{\partial t} (\bar{E}) + \frac{\partial}{\partial x_j} (\bar{\rho} \tilde{u}_j \bar{H}) &= \frac{\partial}{\partial x_j} \left[ \left( \frac{\mu}{\text{Pr}_L} + \frac{\mu_t}{\text{Pr}_t} \right) \frac{\partial \bar{h}}{\partial x_j} \right] + \\ \frac{\partial}{\partial x_j} \left[ \tilde{u}_i (\mu + \mu_t) \left( \frac{\partial \tilde{u}_i}{\partial x_j} + \frac{\partial \tilde{u}_j}{\partial x_i} - \frac{2}{3} \mu \frac{\partial \tilde{u}_k}{\partial x_k} \delta_{ij} \right) \right] &+ \frac{\partial}{\partial x_j} \left[ \left( \mu + \frac{\mu_t}{\sigma_k} \right) \frac{\partial k}{\partial x_j} \right] \end{aligned} \quad (2-5)$$

Additional terms appear in the equations involving the average of products of the velocity fluctuations. These are known as the Reynolds stresses and results in more unknowns than equations so additional equations are needed to model these terms. This is known as the closure problem. This problem is resolved using turbulence models to calculate the Reynolds stresses. The Boussinesq approximation (2-6) was suggested to approximate the Reynolds stresses by modeling them as proportional to the mean rate of strain.

$$-\overline{\rho u_i'' u_j''} + \frac{2}{3} \bar{\rho} k \delta_{ij} = \mu_t \left( \frac{\partial \tilde{u}_i}{\partial x_j} + \frac{\partial \tilde{u}_j}{\partial x_i} \right) - \frac{2}{3} \mu_t \frac{\partial \tilde{u}_k}{\partial x_k} \delta_{ij} \quad (2-6)$$

In Equation (2-6),  $\mu_t$  is a positive scalar proportionality coefficient defined as the eddy viscosity. This approach works well for flows where the shear stress dominates the flow but the isotropic turbulence assumption inherent in the model limits its applicability. Turbulence models are used to calculate a value for  $\mu_t$ , usually relating it to a function involving the transport of turbulent kinetic energy and dissipation rate. Three RANS turbulence models will be discussed in this section. The first model that will be discussed is the k- $\epsilon$  [29] and the second model is the k- $\omega$  model [29]. The third model is the Shear



Stress Transport (SST) model [28] that is a combination of the first two models. The DES model is then incorporated by making changes within the RANS SST model.

The k-ε model calculates the transport of two turbulence quantities: the turbulent kinetic energy (k) and the turbulent dissipation rate (ε). The compressible kinetic energy is given in Equation (2-7) [27].

$$\frac{\partial \bar{\rho} k}{\partial t} + \frac{\partial \bar{\rho} \tilde{u}_i k}{\partial x_i} = \frac{\partial}{\partial x_j} \left[ \left( \mu + \frac{\mu_t}{\sigma_k} \right) \frac{\partial k}{\partial x_j} \right] + P_k - \bar{\rho} (\varepsilon + \varepsilon_c) + \overline{p'' d''} \quad (2-7)$$

In (2-7),  $P_k$  is the production of turbulent kinetic energy calculated using Equation (2-8),  $\sigma_k$  is the turbulent Schmidt number typically with a value of unity, and ε is the dissipation rate,  $\varepsilon_c$  is the compressible dissipation rate given by Equation (2-9), and  $\overline{p'' d''}$  is the pressure dilation given by Equation (2-10). Turbulent viscosity is calculated using Equation (2-11) where  $C_\mu = 0.09$ . In Equations (2-9) and (2-10) the turbulent Mach number is given by Equation (2-12). In Equations (2-9) and (2-10),  $\alpha_1 = 1.0$ ,  $\alpha_2 = 0.4$ , and  $\alpha_3 = 0.2$ .

$$P_k = \nu_t \left( \frac{\partial \tilde{u}_i}{\partial x_j} + \frac{\partial \tilde{u}_j}{\partial x_i} \right) \frac{\partial \tilde{u}_i}{\partial x_j} - \frac{2}{3} k \frac{\partial \tilde{u}_i}{\partial x_i} \quad (2-8)$$

$$\varepsilon_c = \alpha_1 M_t^2 \varepsilon \quad (2-9)$$

$$\overline{p'' d''} = -\alpha_2 P_k M_t^2 + \alpha_3 \bar{\rho} \varepsilon M_t^2 \quad (2-10)$$

$$\mu_t = C_\mu \frac{\bar{\rho} k^2}{\varepsilon} \quad (2-11)$$

$$M_t = \sqrt{\frac{2k}{\gamma RT}} \quad (2-12)$$

The dissipation rate is calculated using [29]

$$\frac{\partial \bar{\rho} \varepsilon}{\partial t} + \frac{\partial \bar{\rho} \tilde{u}_i \varepsilon}{\partial x_i} = \frac{\partial}{\partial x_i} \left[ \left( \mu + \frac{\mu_t}{\sigma_\varepsilon} \right) \frac{\partial \varepsilon}{\partial x_i} \right] + C_{\varepsilon 1} \frac{\varepsilon}{k} P_k - C_{\varepsilon 2} \bar{\rho} \frac{\varepsilon^2}{k}, \quad (2-13)$$

where  $C_{\varepsilon 1}=1.44$  and  $C_{\varepsilon 2}=1.92$ .

The second two Equation model is the k- $\omega$  model developed by Wilcox [44].

This model uses the turbulence variable  $\omega$  (Equation (2-14)) that is a function of the turbulent dissipation [27].

$$\omega = \frac{\varepsilon}{C_\mu k} \quad (2-14)$$

Eddy viscosity is then calculated using:

$$\nu_t = \frac{k}{\omega}. \quad (2-15)$$

The equation for transport of  $\omega$  in the Wilcox model is given by Equation (2-16) [29]

$$\begin{aligned} \frac{\partial \bar{\rho} \omega}{\partial t} + \frac{\partial \bar{\rho} \tilde{u}_i \omega}{\partial x_i} = \frac{\lambda_2}{\nu_t} P_k - \beta_2 \bar{\rho} \omega^2 + \beta^* \alpha_1 M_t^2 \bar{\rho} \omega^2 - \frac{\overline{p'' d''}}{\nu_t} + \\ 2 \bar{\rho} \sigma_{\omega 2} \frac{1}{\omega} \frac{\partial k}{\partial x_i} \frac{\partial \omega}{\partial x_i} + \frac{\partial}{\partial x_j} \left[ \left( \mu + \sigma_{\omega 2} \mu_t \right) \frac{\partial \omega}{\partial x_j} \right] \end{aligned} \quad (2-16)$$

where  $\kappa = 0.41$ ,  $\beta = 0.075$ ,  $\lambda=5/9$ ,  $\sigma_\omega=0.5$ ,  $\beta_2=0.0828$ ,  $\beta^*=0.09$ ,  $\sigma_\omega=0.5$ ,  $\sigma_{\omega 2}=0.769$ , and  $P_k$  is calculated using Equation (2-8) [29]. The constant  $\lambda_2$  is equal to 1.44 for planar jets and 1.6 for axisymmetric jets.

The k- $\varepsilon$  and k- $\omega$  models have their strengths and weaknesses. The k- $\varepsilon$  model is more accurate in shear flows while the k- $\omega$  model is more accurate near the wall and is more numerically stable than the k- $\varepsilon$  model in this region. The SST model combines

these two models using a blending function. The new, blended equations are given by Equations (2-17) and (2-18) [29].

$$\begin{aligned} \frac{\partial \bar{\rho}k}{\partial t} + \frac{\partial \bar{\rho}\tilde{u}_i k}{\partial x_i} &= P_k - \bar{\rho}\omega\beta^* k [1 + \alpha_1 M_t^2 (1 - F_1)] + (1 - F_1)\overline{p''d''} + \\ &\frac{\partial}{\partial x_j} \left[ (\mu + \sigma_k \mu_t) \frac{\partial k}{\partial x_j} \right] \end{aligned} \quad (2-17)$$

$$\begin{aligned} \frac{\partial \bar{\rho}\omega}{\partial t} + \frac{\partial \bar{\rho}\tilde{u}_i \omega}{\partial x_i} &= \frac{\gamma}{v_t} P_k - (1 - F_1) \frac{\overline{p''d''}}{v_t} - \beta \bar{\rho}\omega^2 + (1 - F_1)\beta^* \alpha_1 M_t^2 \bar{\rho}\omega^2 + \\ &2\bar{\rho}\sigma_{\omega 2} \frac{1}{\omega} (1 - F_1) \frac{\partial k}{\partial x_i} \frac{\partial \omega}{\partial x_i} + \frac{\partial}{\partial x_j} \left[ (\mu + \sigma_{\omega} \mu_t) \frac{\partial \omega}{\partial x_j} \right] \end{aligned} \quad (2-18)$$

In Equations (2-17) and (2-18),  $\sigma_k=0.5$ ,  $P_k$  is the production of turbulent kinetic energy, and  $F_1$  is a blending function given by

$$F_1 = \tanh \left( \left[ \min \left[ \max \left( \frac{\sqrt{k}}{C_{\mu} \omega y}, \frac{500\nu}{y^2 \omega} \right), \frac{4\rho\sigma_{\omega 2} k}{CD_{kw} y^2} \right] \right]^4 \right) \quad (2-19)$$

where  $y$  is the normal distance to the wall and  $CD_{kw}$  is the positive portion of

$$CD_{kw} = \max \left( 2\sigma_{\omega 2} \frac{1}{\omega} \frac{\partial \bar{\rho}k}{\partial x_j} \frac{\partial \bar{\rho}\omega}{\partial x_j}, 10^{-20} \right). \quad (2-20)$$

The coefficients in Equation (2-18) are computed using Equation (2-21) to blend the coefficients corresponding to the  $k-\omega$ ,  $\theta_1$ , with the coefficients from the  $k-\varepsilon$  model,  $\theta_2$  [27].

$$\theta = F_1 \theta_1 + (1 - F_1) \theta_2. \quad (2-21)$$

Eddy viscosity is calculated using equation

$$v_t = \frac{a_1 k}{\max(a_1 \omega, \Omega F_2)}, \quad (2-22)$$

Where  $a_1=0.31$ ,  $\Omega$  is the magnitude of the vorticity vector and  $F_2$  is calculated from Equation (2-23).

$$F_2 = \tanh \left[ \max \left( \frac{2\sqrt{k}}{C_\mu \omega y}, \frac{500\nu}{y^2 \omega} \right) \right]. \quad (2-23)$$

Now that the SST model has been formulated, it must be modified to incorporate DES. The DES modifications to the SST model replaces the dissipation term in Equation (2-17) with [27]

$$\varepsilon = \frac{\omega}{\beta^* k} = \frac{\varepsilon}{\min \left( 1.0, C_{DES} \frac{L_g}{L_t} \right)} \quad (2-24)$$

where  $L_g$  is the maximum grid length,  $L_t$  is the turbulence length scale and  $C_{DES}$  is the DES coefficient. Turbulence length scale and the CDES are calculated using Equations (2-25) and (2-26) [27] respectively.

$$L_t = \frac{\sqrt{k}}{\beta^* \omega} = \frac{k^{3/2}}{\varepsilon} \quad (2-25)$$

$$C_{DES} = (1 - F_1) C_{DESKE} + F_1 C_{DESKW} \quad (2-26)$$

In Equation (2-26),  $\beta^*=0.09$ ,  $C_{DESKE}=0.61$ ,  $C_{DESKW}=0.78$  and  $F_1$  is the blending coefficient calculated using Equation (2-19) [27]. This model adjusts the eddy dissipation if the grid length scale is less than the turbulent length scale which reduces the eddy dissipation these regions. This results in a Smagorinsky type LES model in the free shear regions of the flow with the wall bounded portions modeled with the  $k-\omega$  model.

Turbulent length scales not resolved on the computational grid are modeled using the RANS turbulence model which behaves like a subgrid model in LES.

## **CHAPTER 3**

### **METHOD OF SOLUTION**

#### **3.1 Computational Fluid Dynamics simulations**

The OVERFLOW 2 CFD code [30] (version 2.2c) was used in this research. The OVERFLOW2 CFD code has been successfully used to analyze a variety of unsteady fluid dynamic phenomena [31-35]. Based on these results and prior experience using this code, it was felt that it was adequate for performing this study. The OVERFLOW 2 flow solver is a structured, overset CFD code developed at NASA Ames and NASA Langley. The overset solver allows complex geometries to be decomposed into smaller, more manageable pieces. Grids are built for the individual geometric components so that adjacent grids overlap each other with the degree of overlap determined by the accuracy requirements of the numerical scheme used to generate a solution. The individual grids are then assembled using the PEGASUS code that identifies grid overlap and determines the grid to grid communication stencils. Unnecessary portions of grids, such as those that overlap into walls, are flagged so that the solver ignores the contribution from these regions to the overall flow field.

OVERFLOW 2 is a node-centered, finite-difference code which solves the perfect gas form of the compressible Navier-Stokes equations. Solution can be steady state or time accurate using implicit time marching. Various numerical schemes are available in OVERFLOW 2, allowing the user flexibility to determine the appropriate method to

solve a given problem. The following mathematical description is based on the OVERFLOW2 User's Manual [30].

The Navier-Stokes equations in generalized coordinates are given by:

$$\frac{\partial \bar{q}}{\partial t} + \frac{\partial \bar{E}}{\partial \xi} + \frac{\partial \bar{F}}{\partial \eta} + \frac{\partial \bar{G}}{\partial \zeta} = 0 \quad (3-1)$$

Where  $\bar{q}$  is the vector of conserved variables:

$$\bar{q} = \begin{bmatrix} \rho \\ \rho u \\ \rho v \\ \rho w \\ \rho e_0 \end{bmatrix} \quad (3-2)$$

Equation (3-1) can be rewritten in traditional, linearized implicit form including subiterations:

$$\begin{aligned} & \left[ I + \frac{\Delta t}{(1+\theta)\Delta\tau} + \frac{\Delta t}{1+\theta} (\partial_\xi A + \partial_\eta B + \partial_\zeta C) \right] \Delta q^{n+1,m+1} = \\ & - \left[ (q^{n+1,m} - q^n) - \frac{\theta}{1+\theta} \Delta q^n + \frac{\Delta t}{1+\theta} \text{RHS}^{n+1,m} \right] \end{aligned} \quad (3-3)$$

where

$$\text{RHS} = \frac{\partial \bar{E}}{\partial \xi} + \frac{\partial \bar{F}}{\partial \eta} + \frac{\partial \bar{G}}{\partial \zeta}. \quad (3-4)$$

In Equation (3-3),  $\theta=0$  for first order time differencing and  $\theta=1/2$  for second order time differencing. The variable n is the time step number and m is the subiteration number.

Equation (3-3) introduces an artificial time term used for time marching using dual time stepping:

$$\left( \frac{\Delta t}{(1+\theta)\Delta\tau} \right) \quad (3-5)$$

where pseudo time,  $\tau$ , may vary through the flow field. Dual time stepping for time-accurate calculations requires that the artificial time term converge at each physical time step to maintain temporal accuracy. The solution is calculated implicitly for each grid but the overset interpolated boundaries are updated explicitly at each subiteration. This improves global convergence at each time step by allowing exchange of information between grids.

Equation (3-3) has the form of  $\mathbf{Ax}=\mathbf{b}$  the solution of which involves direct inversion of matrix A. This can be computationally expensive for three-dimensional flows so approximations have been made to expedite the procedure. Factoring Equation (3-3) in space yields:

$$\begin{aligned} & \left[ I + \frac{\Delta t}{1+\theta} \partial_{\xi} A \right] \left[ I + \frac{\Delta t}{1+\theta} \partial_{\eta} B \right] \left[ I + \frac{\Delta t}{1+\theta} \partial_{\zeta} C \right] \Delta q^{n+1,m+1} = \\ & - \left[ \left( q^{n+1,m} - q^n \right) - \frac{\theta}{1+\theta} \Delta q^n + \frac{\Delta t}{1+\theta} RHS^{n+1,m} \right] + \text{Error} \end{aligned} \quad (3-6)$$

where the factorization error is given by

$$\text{Error} = - \left( \frac{\Delta t}{1+\theta} \right)^2 \left( \delta_{\xi} A \delta_{\eta} B + \delta_{\xi} A \delta_{\zeta} C + \delta_{\eta} B \delta_{\zeta} C \right) - \left( \frac{\Delta t}{1+\theta} \right)^3 \left( \partial_{\xi} A \partial_{\eta} B \partial_{\zeta} C \right). \quad (3-7)$$

The factorization error term is usually ignored resulting in an approximate factorization of Equation (3-3). Since the factorization error is scaled by time step it can limit or



prevent convergence for large time steps. The approximate factorization of Equation (3-6) is a three factor alternating direction implicit (ADI) scheme where A, B and C are the block tridiagonal matrices for structured grids with central difference or first order spatial upwind flux jacobians. The factored system can be solved by inverting the block tridiagonal matrices in each direction.

The A, B, and C matrices in Equation (3-6) may be decomposed into eigenvalues ( $\Lambda$ ) and eigenvectors (X)

$$\begin{aligned} A &= X_A \Lambda_A X_A^{-1} \\ B &= X_B \Lambda_B X_B^{-1} \\ C &= X_C \Lambda_C X_C^{-1} \end{aligned} \quad (3-8)$$

Substituting Equation (3-8) into Equation (3-6) results in a scalar pentadiagonal matrix form in each factored direction when mixed second and fourth order smoothing is included on the implicit side of the equation.

$$\begin{aligned} &X_A \left[ I + \frac{\Delta t}{1+\theta} \partial_{\xi} \Lambda_A \right] X_A^{-1} X_B \left[ I + \frac{\Delta t}{1+\theta} \partial_{\eta} \Lambda_B \right] X_B^{-1} X_C \left[ I + \frac{\Delta t}{1+\theta} \partial_{\zeta} \Lambda_C \right] X_C^{-1} \Delta q^{n+1,m+1} \\ &- \left[ (q^{n+1,m} - q^n) - \frac{\theta}{1+\theta} \Delta q^n + \frac{\Delta t}{1+\theta} \text{RHS}^{n+1,m} \right] + \text{Error} \end{aligned} \quad (3-9)$$

The approximations used to derive Equation (3-9) affect time accuracy for CFL numbers greater than one. The inversion of a scalar pentadiagonal matrix at each point can be done efficiently resulting in an extremely fast algorithm. A variety of implicit algorithms have been implemented into OVERFLOW 2. A full description of the implemented algorithms can be found in [30,36].

## CHAPTER 4

### RESULTS AND DISCUSSION

#### 4.1 Impinging Jet Geometry

The geometry analyzed in this study is an ideally expanded, supersonic jet impinging on a flat plate. The geometric parameters in the CFD analysis match those presented in the test setup found in Reference [10]. The test investigated the impingement of a supersonic jet on a flat plate. The supersonic jet was produced from a converging-diverging nozzle with an area ratio that gives ideally expanded flow at the nozzle exit ( $P_{\text{exit}} = P_{\text{atm}}$ ). The exit of the converging-diverging nozzle was flush mounted to a 25.4 cm diameter lift plate that was used to measure the downward force induced by air entrainment into the jet. A square impingement plate measuring 2.44 m x 2.44 m was placed at different distances below the nozzle exit depending on the test configuration being investigated. The computational model did not extend to the edges of the impingement plate so the plate covers the entire bottom of the computational domain.

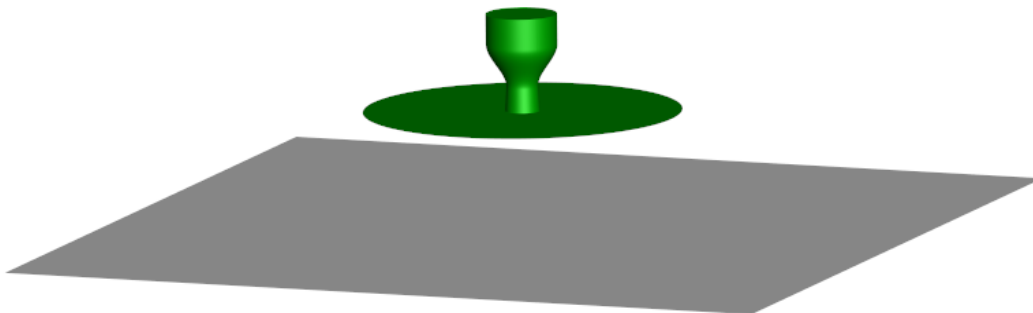


Figure 4-1 Computational model

The converging-diverging nozzle is described as having a converging section based on a third order polynomial and a conic diverging section with a constant angle of three degrees. The nozzle throat and exit diameters are 2.54 cm and 2.75 cm respectively, which gives an area ratio resulting in a perfectly expanded exit Mach number of 1.5 for a nozzle pressure ratio (NPR) of 3.7. The test nozzle geometry was provided by Florida State University and was incorporated into the model. The test utilized a long nozzle which allowed slow variation of the area ratio in the flow direction. One of the parameters of interest in this study was the effects of nozzle geometry on the jet flow field and acoustic properties. Previous studies [1,4,5,8,9,12-14] of supersonic jet impingement used overexpanded, converging nozzles to generate a supersonic jet and the results did not show sensitivity to nozzle geometry. A second nozzle was designed to provide a comparative analysis to determine if the nozzle geometry had measurable effects for an ideally expanded supersonic jet. Like the test nozzle, the new nozzle had the same expansion ratio, a converging section described by a third order polynomial and a conic diverging section with a constant angle of three degrees. However, the new nozzle was significantly shorter than the test nozzle. The new nozzle has a maximum converging section angle of  $33^\circ$  and throat radius of curvature of 1.0 throat radius ( $r_t$ ), resulting in a more aggressive area change along the nozzle axis than the test nozzle. Figure 4-2 compares the nozzle geometries used in the study.

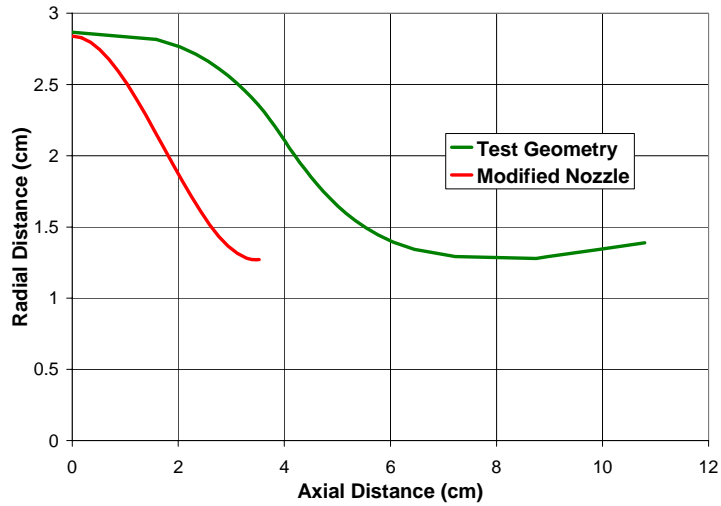


Figure 4-2 Comparison of test and modified nozzle geometries

The nozzle grids are wall fitted grids that wrap around the nozzle exit and onto the lift plate (Figure 4-3). The spacing of the nozzle grids was fine enough at the wall to resolve the laminar boundary layer on the nozzle wall. Wall grid spacing varied from  $2 \times 10^{-6}$  m at the combustion chamber section,  $3.4 \times 10^{-7}$  at the nozzle throat, and  $1 \times 10^{-5}$  m at the nozzle exit so that a  $y^+ \leq 1$  was maintained. The flow in the nozzle was modeled as laminar based on the test observations [10]. A boundary layer grid was placed on the lift plate. Fine grids were placed on the impingement plate but no attempt was made to fully resolve the boundary layer and wall functions were used in this region. The spacing at the impingement plate is  $2 \times 10^{-4}$  m which is sufficient for a  $y^+ \sim 20$ . The grid between the nozzle exit and the impingement plate is a uniform mesh with a spacing of  $6 \times 10^{-4}$  meters. Uniform meshing was used to eliminate phase error associated with grid stretching. The grid spacing was calculated to minimize phase error in the solution by ensuring at least 80 points per wavelength [37] for the maximum, primary tone frequencies of 7000 Hz measured in the tests. The speed of sound for this calculation

was assumed to be the ambient value 346 m/sec. The total grid system size for each case analyzed is shown in Table 4-1. Each case required approximately 65,000 to 97,000 CPU hours of computation time depending on the stability of the jet and the number of grid points in the domain.

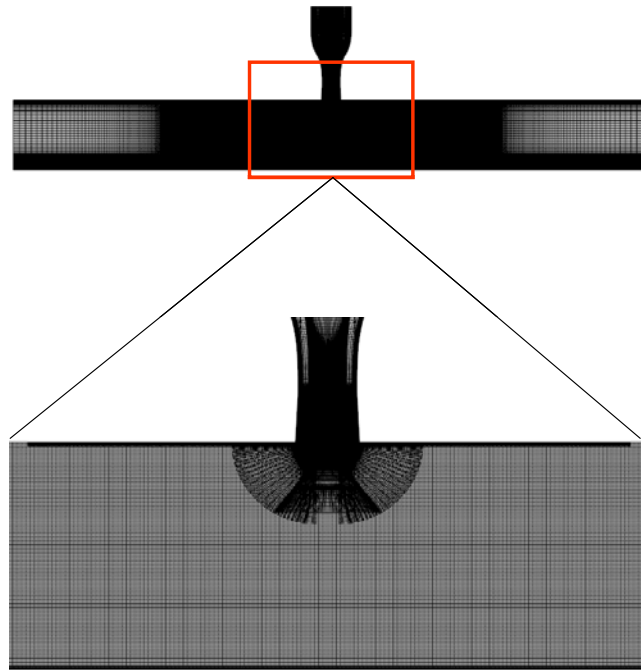


Figure 4-3 Computational grid

Table 4-1 Grid size for each case

<b>Separation Distance (throat diameters)</b>	<b>Grid Size (millions of points)</b>
3.75	75.2
4	78.7
4 (modified nozzle)	77.2
4.25	84.4

The three nozzle exit to impingement plate distances investigated in the test were also investigated in this numerical study. The separation distances, given in ratios of separation distance,  $h$ , to nozzle throat diameter,  $d$ , are  $h=3.75d$ ,  $4d$  and  $4.25d$ . Steady-

state solutions were obtained first for each case and then used as initial conditions for the unsteady calculations. The unsteady calculations continued until the pressure data became statistically steady and a sample of sufficient size for statistical analysis was obtained. Probe points were placed on two concentric arcs around both the nozzle exit and impingement point to record time histories of the flow properties. The data from these locations were then used to determine the directivity of sound. The study with the modified nozzle was performed at a separation distance of  $4d$ , since most test data [10] was available for this separation distance compared to the other separation distances.

#### **4.2 Test Data Comparisons**

CFD results were compared to test data [10] to ensure that the relevant physics are being captured. Measured sound pressure levels at a near field point were available in the test data for all three separation distances investigated in this study. Additional time averaged centerline velocity data and shear layer convection velocities were available for the  $h/d=4$  separation distance.

Sound pressure levels (SPL) were calculated at a near field point in the CFD simulation and compared to microphone data measured at a near field point 25 cm from the plume centerline axis. The high resolution requirements of the CFD simulation limited how far from the jet centerline the monitor point could be placed. The grid size requirements needed to extend the high resolution mesh to a point 25 cm from the jet centerline was prohibitive therefore the near field point was placed 18.5 cm from the jet centerline. As a consequence, the calculated SPL are expected to be higher than the measured SPL in the test but with no change in the frequencies. The observed test

frequencies of interest were between 3000 Hz and 6000 Hz so the distance from the jet axis to the near field point is approximately 1.7 wavelengths for the low frequency tones and 3.3 wavelengths for the high frequency tones. Pressure data at points in the flow field were recorded and used to determine if the flow was statistically steady before interrogating the flow field for statistic properties. The time history of the pressure at a near field monitor point for the  $h/d=4$  case is shown in Figure 4-4. The signal is seen to be statistically steady and shows the time period over which the flow field was interrogated for statistical information.

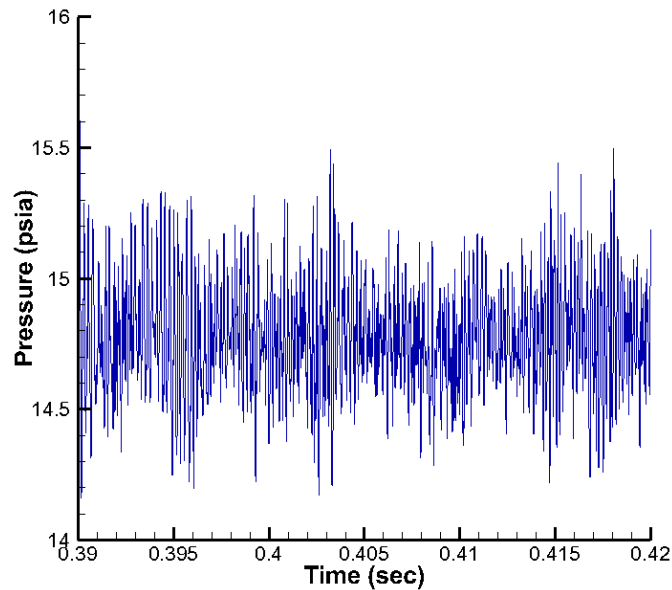


Figure 4-4 Near-field pressure signal:  $h/d=4$

Figure 4-5 shows a comparison between measured sound pressure level at the near field location to that obtained from CFD for the  $h/d=3.75$  case. CFD results show the presence of three distinct peaks similar to the test data. Previous investigations [8] show that three types of impingement tones are common for supersonic jet impingement. The tones are identified as L1, L2 and L3 tones. Perfectly expanded supersonic jets can

exhibit all three tones and do not exhibit the “zones of silence” observed for underexpanded, supersonic jet impingement [12].

Table 4-2 shows the tones measured in the impingement tests [10] and calculated with CFD. All three impingement tones obtained from the CFD are within 8% of that of the test data. The magnitude of the L3 tone is dominant in the CFD results whereas in the test results, the three tones are of similar magnitude. The frequency roll-off in the CFD solution at 15000 Hz is a function of the temporal resolution of the simulation.

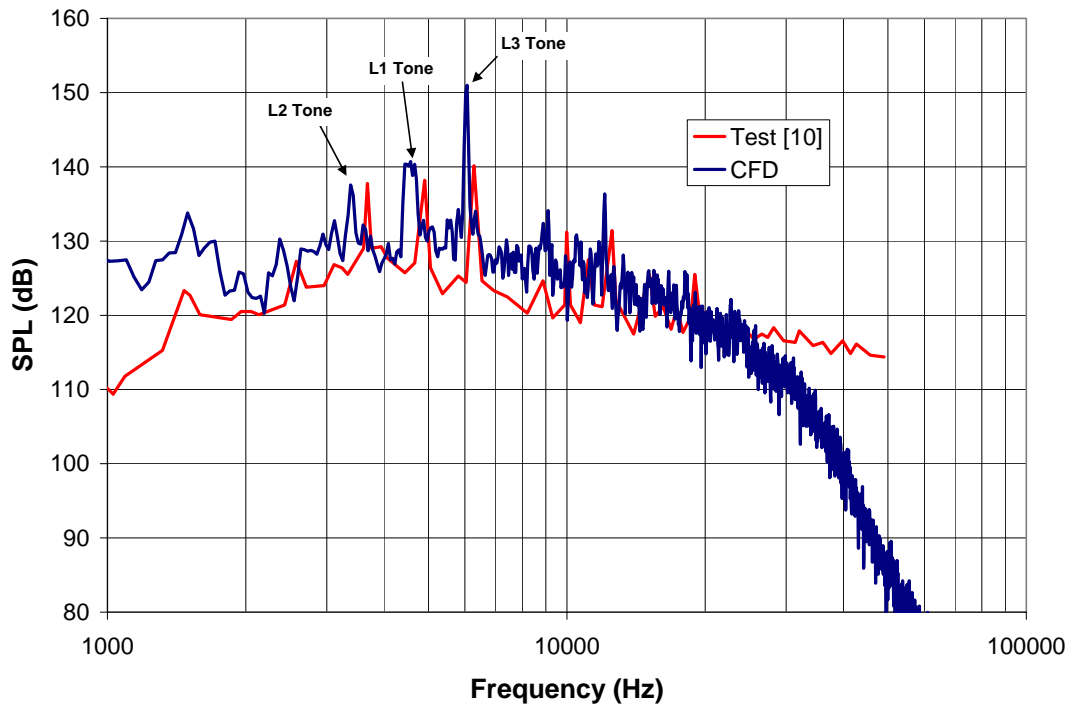


Figure 4-5 Comparison of near field sound pressure levels:  $h/d=3.75$

Table 4-2 Comparison of impingement tones  $h/d=3.75$

Tone	Frequency (Hz)		
	Test Data [10]	CFD	% Difference
L2	3680	3380	8.2
L1	4902	4660	4.9
L3	6275	6070	3.3



Figure 4-6 compares the SPL predicted by CFD and obtained from test data for the  $h/d=4$  separation distance. The CFD results and test data [10] compare well with the peaks predicted by CFD slightly lagging the measured test frequencies as shown in Table 4-3. The CFD frequency's lag is within 4% of the measured test values.

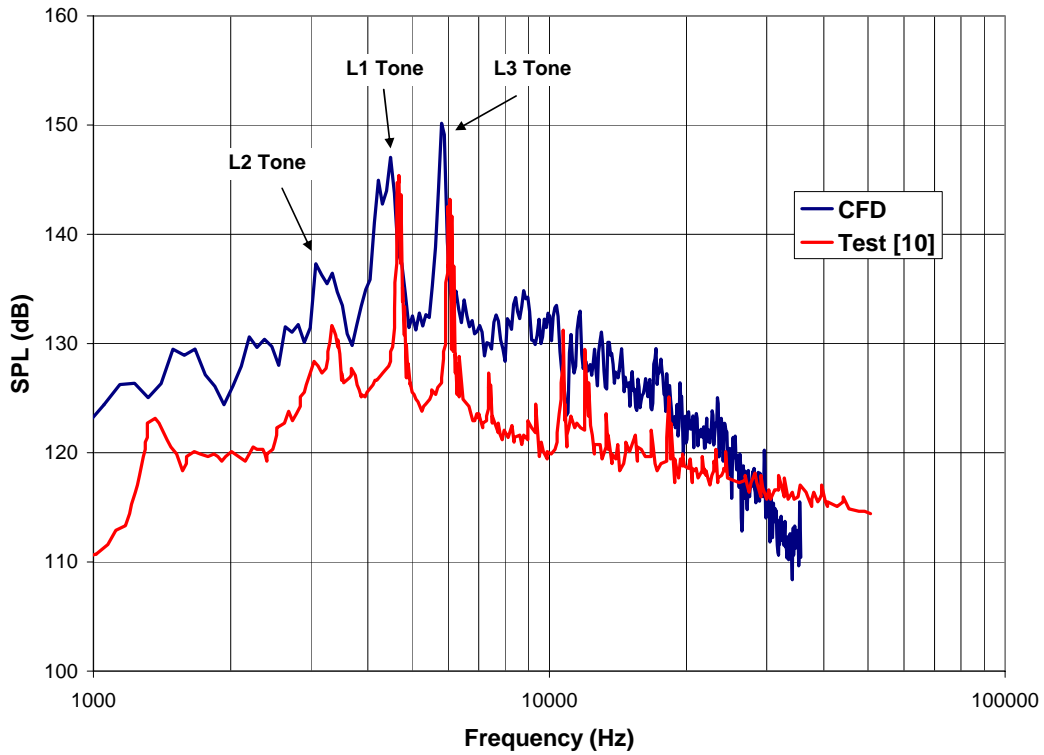


Figure 4-6 Comparison of near field sound pressure levels:  $h/d=4$

Table 4-3 Comparison of impingement tones  $h/d=4$

Tone	Frequency (Hz)		
	Test Data [10]	CFD	% Difference
L2	3340	3250	2.7
L1	4680	4480	4.3
L3	6050	5800	4.1

The SPL comparisons for the  $h/d=4.25$  separation case are shown in Figure 4-7. The CFD shows strong L1 and L2 tones compared to the weaker tones in the test data.

The broad nature of the L2 tone seen in the test is also captured in the CFD. In both the CFD and the test data, the L3 tone is the strongest but its relative magnitude is larger in the test than in the CFD. The CFD results for all three separation distances show good agreement with the test data.

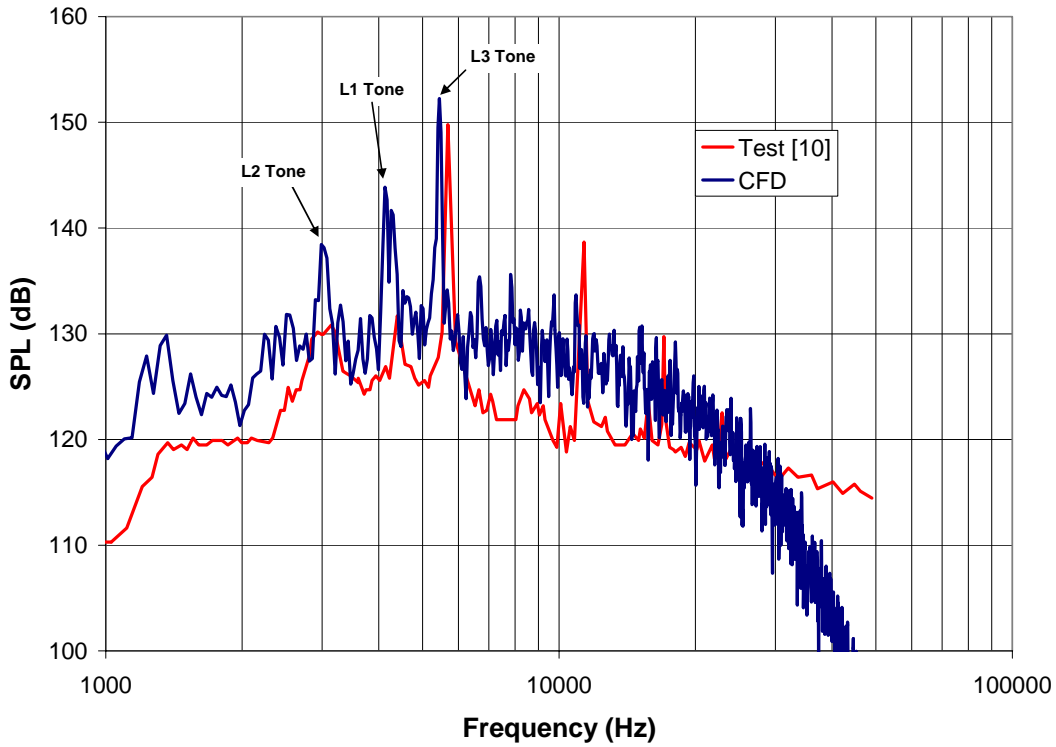


Figure 4-7 Comparison of near field sound pressure levels:  $h/d=4.25$

Table 4-4 Comparison of impingement tones  $h/d=4.25$

Tone	Frequency (Hz)		
	Test Data [10]	CFD	% Difference
L2	3100	3100	0.0
L1	4400	4130	6.1
L3	5685	5550	2.4

#### 4.2.1 Effects of Separation Distance

The nozzle exit to plate spacing is an important parameter in the behavior and resulting acoustic environment of the jet. The measured sound pressure levels from the

tests [10] are shown in Figure 4-8. The results in Figure 4-8 are offset for clarity with the results for the  $h/d=4$  offset by 20 dB and the ones for the  $h/d=4.25$  by 40 dB, only the results of the  $h/d=3.75$  are unchanged. Figure 4-8 shows that increasing the separation distance has two effects on the impingement tones: a decrease in frequency and change in magnitude of each tone. The decrease in frequency has been observed in a number of tests [4,5,8,10,12,16]. The decrease in frequency has to do with the feedback loop's role in the tone generation. The instabilities that create the tones have their origins in the acoustic interactions between the impingement zone and the nozzle exit. As the distance between the plate and the nozzle exit increases, the acoustic waves take longer to propagate from the impingement point to the nozzle exit. It also takes longer for the disturbances to travel from the nozzle exit to impingement point. The increased distance reduces the frequency of the feedback and therefore reduces the frequency of the tone.

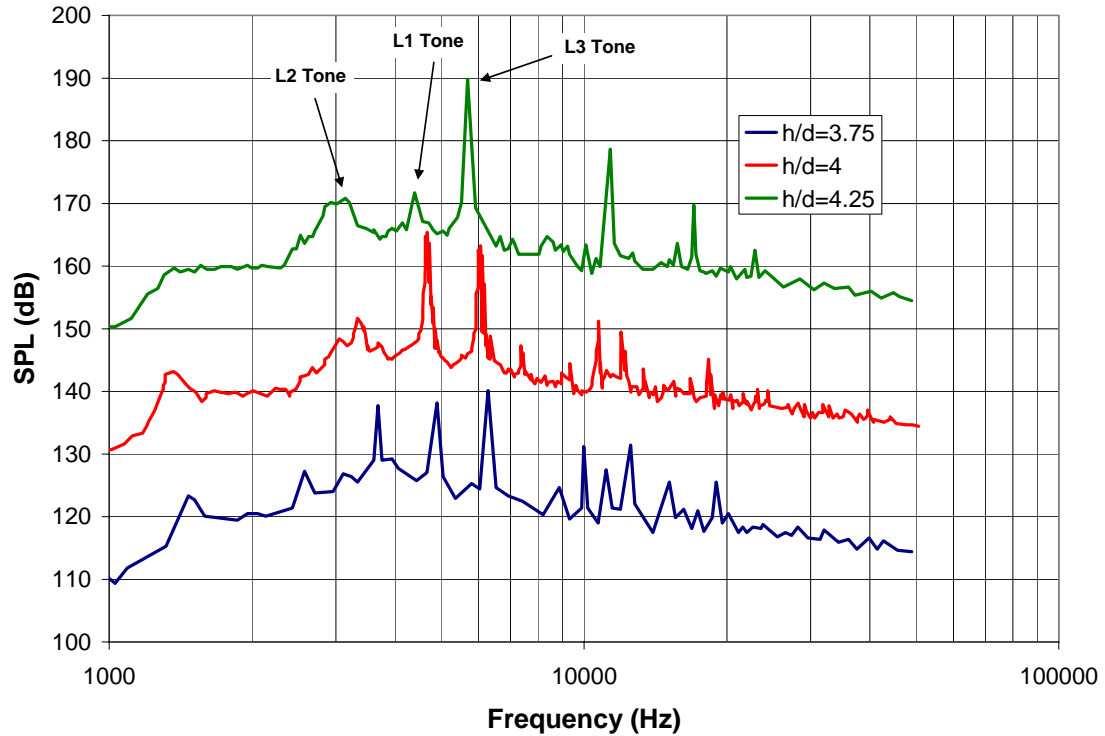


Figure 4-8 Effect of separation distance for measured sound pressure levels from test [10]

The other effect of separation distance is the change in magnitudes of the impingement tones with separation distance. The L2 tone decreases in magnitude and becomes broader as the separation distance increases. The L1 tone initially increases in magnitude but dramatically decreases at the largest separation distance. The L3 tone grows in magnitude with separation distance with a magnitude of approximately 15 dB above the average noise level to a magnitude of approximately 25 dB above the average noise level at the largest separation distance. The CFD results for all the separation distances are shown in Figure 4-9 with the same offsets applied to the CFD results as the test results above.

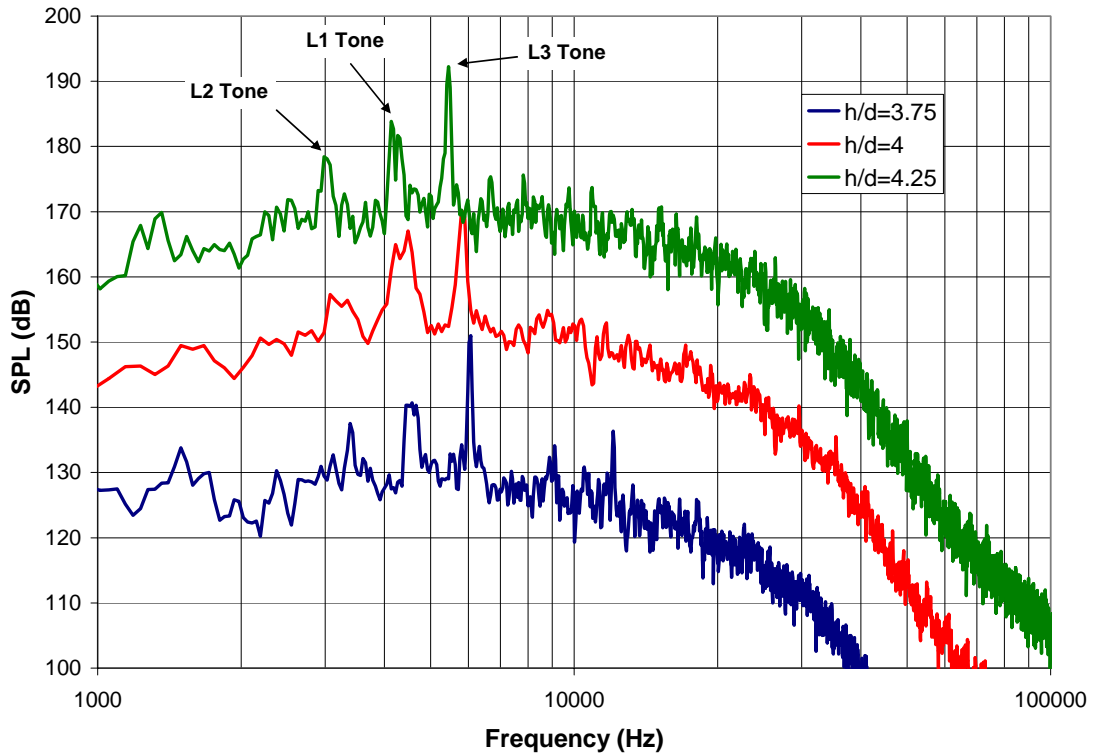


Figure 4-9 Effect of separation distance for CFD calculated sound pressure levels

The decrease in tonal frequencies observed in the test data is also seen in the CFD results. The CFD also shows the broadening of the L2 tone as well as the behavior of the L1 tone with separation distance. However, the CFD results show a stronger L1 tone at the largest separation distance than the test data. The CFD results show a strong L3 tone for all separation distances.

#### 4.2.2 Shear Layer Convective Velocities

Disturbances are born in the jet shear layer as a result of the feedback mechanism between the impingement zone and the nozzle lip. These vortical shear layer disturbances are shown in Figure 4-10. The disturbances propagate downstream in the jet shear layer. The velocity of the propagation of these vortical structures was measured in

the test [10] and in the CFD simulation for the  $h/d=4$  separation distance. The velocity of a vortex was calculated by measuring the distance it traveled over a given time. This was performed for several vortices. The velocities normalized to the jet exit velocity of 427 m/sec are shown in Figure 4-11. The test data shows an average normalized convective velocity of 0.52 while the CFD results predict a normalized convective velocity of 0.54. This is approximately 4% difference between the two results and is within the measurement error for the velocity calculation. It is also interesting to note that the CFD results are encompassed in the data scatter range. This indicates good agreement between the CFD and the test data and confidence that the CFD is properly modeling the physics of the flow.

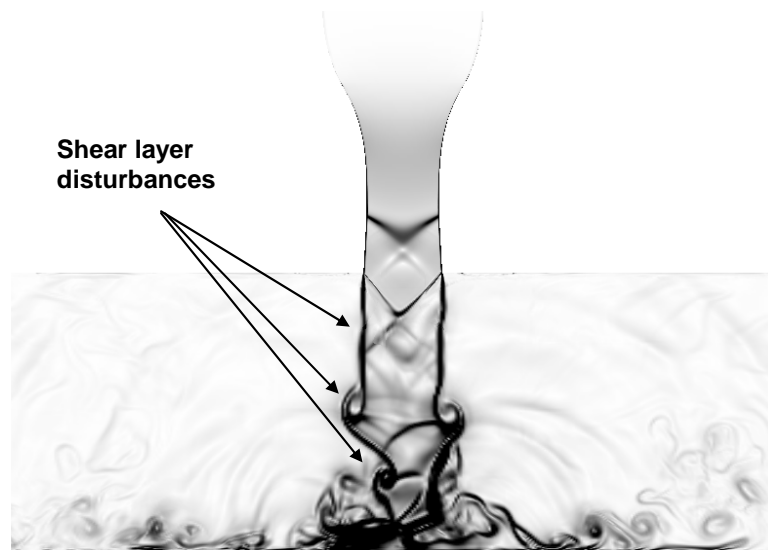


Figure 4-10 Contours of density gradient magnitude showing shear layer disturbances

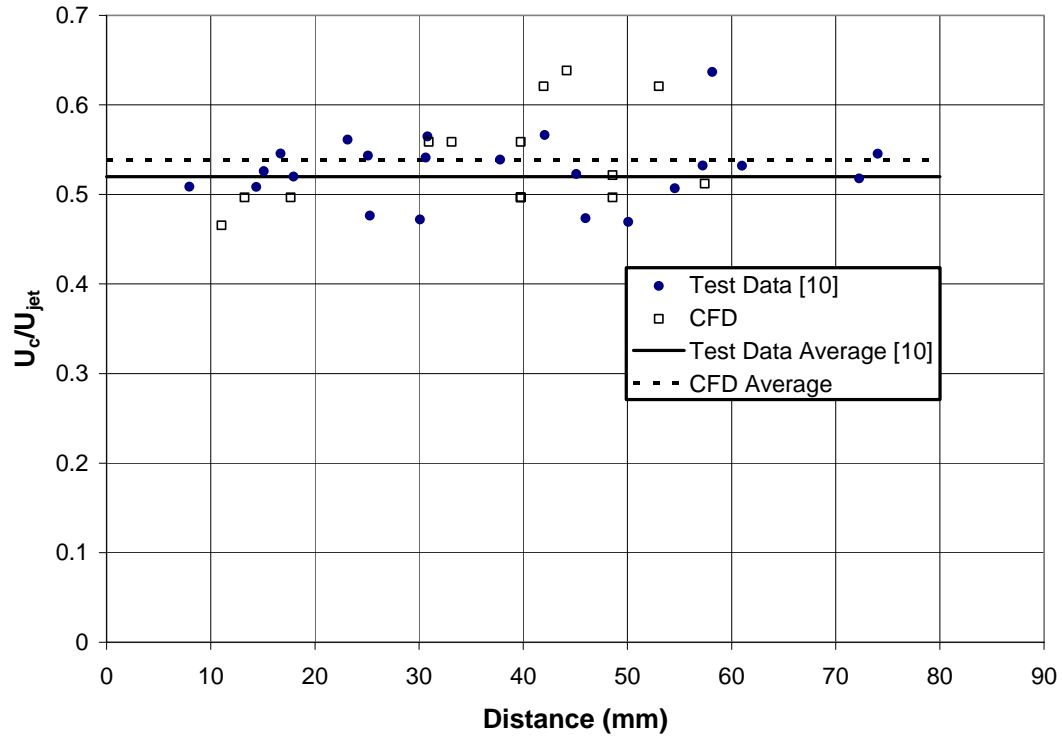


Figure 4-11 Instantaneous convection velocities of shear layer vortical structures

### 4.3 Impingement Tone Analysis

CFD results showed good agreement with the SPL data; however there were some differences in magnitudes of the impingement tones. Time variation of the impingement tones was observed in some cases. A joint time-frequency analysis was performed to determine the variation of the impingement tones with time.

#### 4.3.1 Separation Distance $h/d=4$

Figure 4-13 shows the impingement tones for the  $h/d=4$  case. The results compare favorably with the test data. The test results show that the highest sound pressure level is at 4680 Hz while the CFD shows the highest peak at 5800 Hz. The

shape of the predicted peak at 4480 Hz suggested that there is some competition between frequencies. A joint time-frequency analysis was performed by applying a finite width moving window on the pressure signal to determine if the sound pressure levels changed over time. The window was 8192 samples wide and moved 1000 samples per step in the calculation.

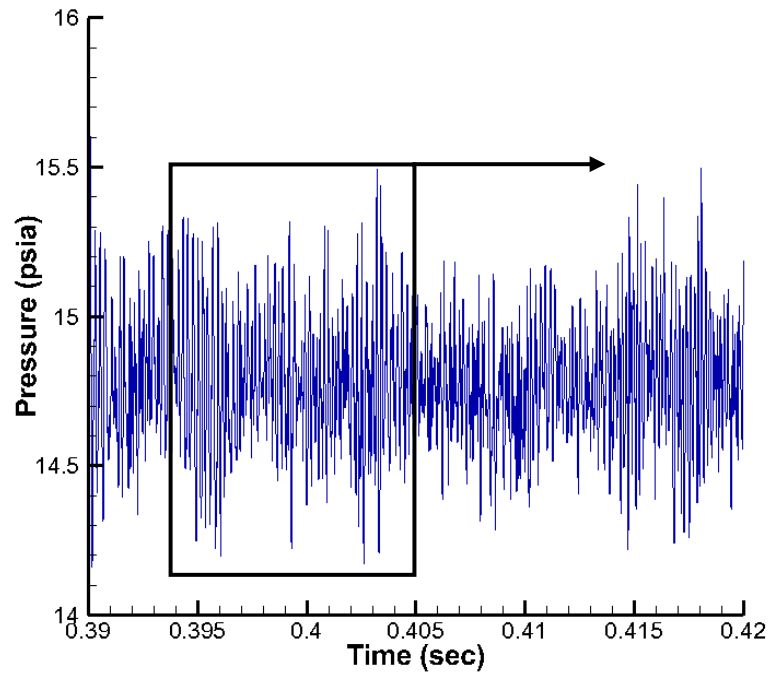


Figure 4-12 Moving window in joint time-frequency analysis:  $h/d=4$  near field pressure



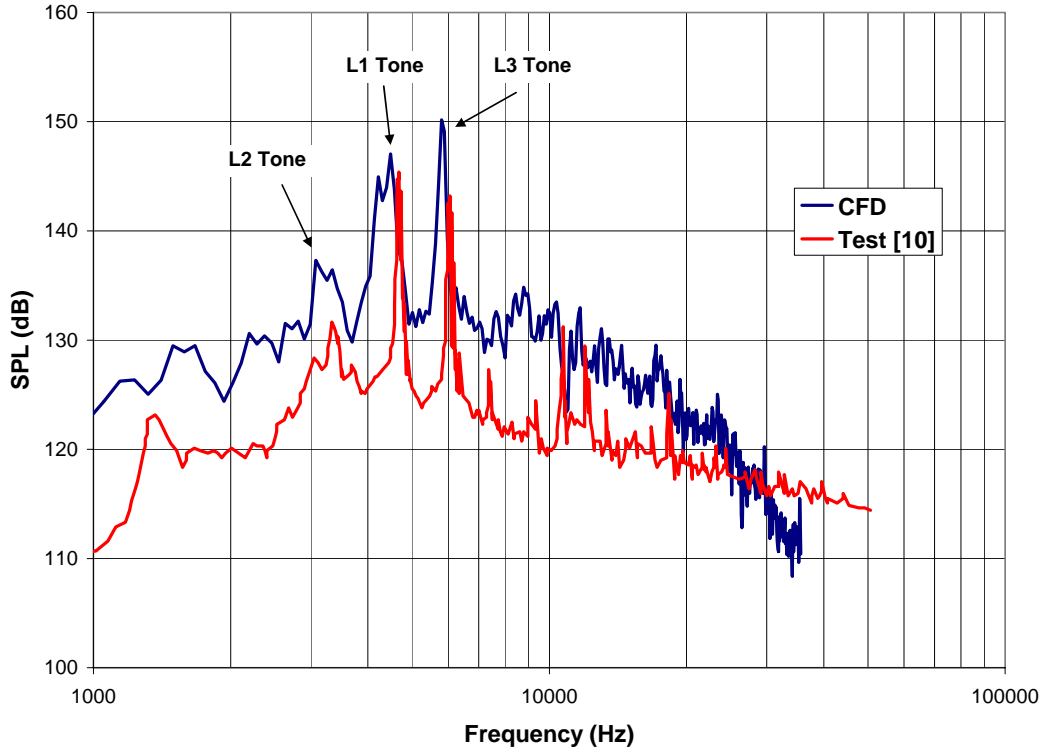


Figure 4-13 Comparison of SPL tone magnitude for  $h/d=4$

Figure 4-14 shows the variation of sound pressure levels at different times. The dominant impingement tones can be seen to change with time. The L3 tone is the dominant tone at the beginning of the cycle (a) but over time, the L1 tone starts the increase in magnitude while the L3 tone begins to decrease in magnitude (b). Later, the L1 is dominant while the L2 tone also increases in magnitude. As time progresses further, the L1 tone diminishes as the L3 tone once again increases in magnitude. Figure 4-15 shows a plot of the variation of sound pressure level with frequency and normalized time (Equation (4-1)).

$$t^* = \frac{t - t_0}{t_{\text{window}}} \quad (4-1)$$

In Equation (4-1),  $t$  is the current time,  $t_0$  is the start time of the time sample and  $t_{\text{window}}$  is the window width used for SPL calculation. The jet exhibits a combination of modes responsible for these frequencies and these oscillations did not appear to be diminishing over the simulation. Test observations showed that the jet showed a distinct change in mode at  $h/d \sim 4$  [10]. The  $h/d=4$  case is in the range of this transition which would result in the jet being unstable and oscillating between different modes. This unstable behavior was also observed for certain separation distances with supersonic impinging jets from underexpanded, choked converging nozzles [8]. These oscillations are not mentioned as being observed during testing [10] and the results shown in Figure 4-13 are based on the entire pressure signal.

The test apparatus allowed tens of minutes of data to be gathered for analysis while the amount of CFD data is limited by the available computational resources. Trying to simulate the test run time would require many years of CPU time which is not feasible. Instead the CFD simulation was run as long as possible to gather as much time data as possible with the total simulated time being less than 0.5 seconds (Figure 4-4). It is believed that over a large time history, the CFD results would reproduce the trend seen in the test data, however the CFD results do show the dominant frequencies observed in the tests.

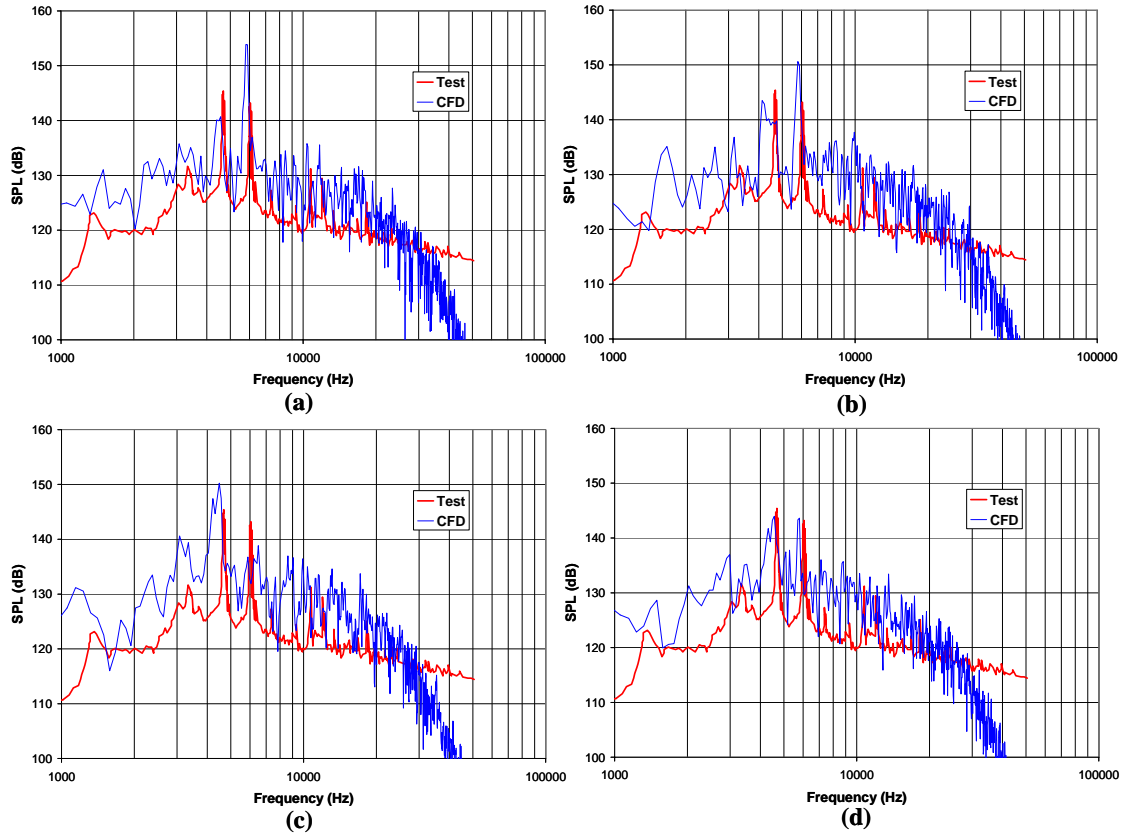


Figure 4-14 Time variation of sound pressure levels:  $h/d=4$

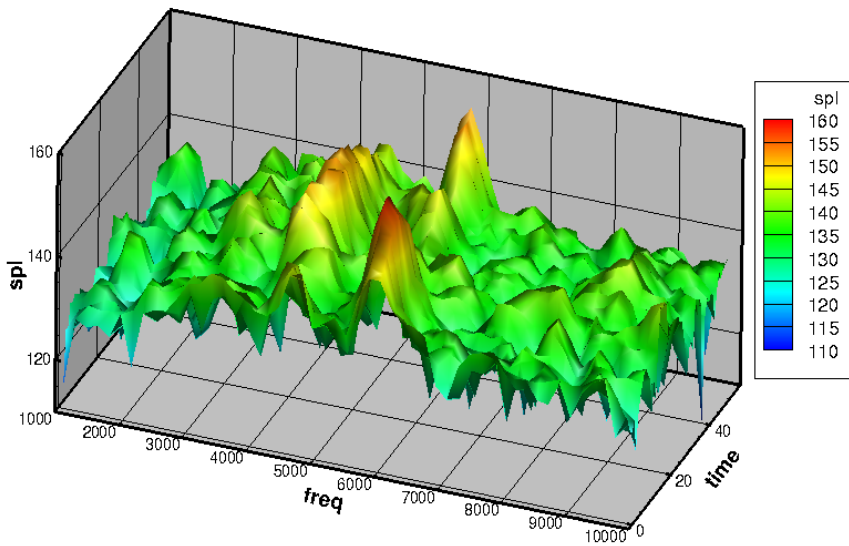


Figure 4-15 SPL variation with time:  $h/d=4$

The jet behavior for this separation distance showed a combination of sinuous and varicose modes [40]. These jet modes appear to correspond to the different impingement tones. The sinuous mode corresponds to a helical mode while the varicose mode corresponds to a symmetric mode. When the sinuous mode is dominant the L3 helical tone is at a maximum while the L1 symmetric tone is at a minimum. At a later time the varicose or symmetric mode dominates resulting in the symmetric L1 tone being the dominant tone and the L3 tone is at a minimum. Interestingly the helical L2 tone increases in strength when the symmetric L1 tone is dominant and is not present when the L3 tone is dominant. This suggests that the two helical tones may be mutually exclusive and do not manifest at the same time. Test data shows that the L2 tone becomes broader and less defined as the separation distance decreases. The frequency also decreases so that it approaches half the frequency of the L3 tone. The competition with L3 subharmonic may be the cause of the broadening and weakening of the L2 tone when the L3 tone is dominant.

#### **4.3.2 Separation Distance $h/d=3.75$**

Figure 4-16 shows all three tones appearing in the test data and CFD results with the L3 tone being the most dominant. The CFD results show the L3 tone being relatively stronger than seen in the test data. The results also show a broader L1 tone than in the test data, indicating more than one tone near this frequency.

The impingement tones magnitudes showed a similar time dependency (Figure 4-17) as was observed in the  $h/d=4$  case, however the magnitudes changed more rapidly with time. Since the magnitudes changed rapidly, the moving time window was small

resulting in a coarse frequency resolution, but the time dependency can be seen. The cycle of the L3 tone and the L1 tone alternately growing and diminishing as well as coexisting can be seen. The L2 tone tends to diminish when a strong L1 tone is present and increases when the L3 tone is dominant. The dominance of the L3 tone in time is the reason that it is also the overall dominant tone for the entire time history which is not what was observed for the  $h/d=4$  case where it does not dominate all the time. All three tones are present for some times as they oscillate in magnitudes indicating a complex jet behavior. The time history of near field pressure is shown in Figure 4-18. Wave packets can be seen in the pressure signal indicating the time variation of frequency observed in Figure 4-17.

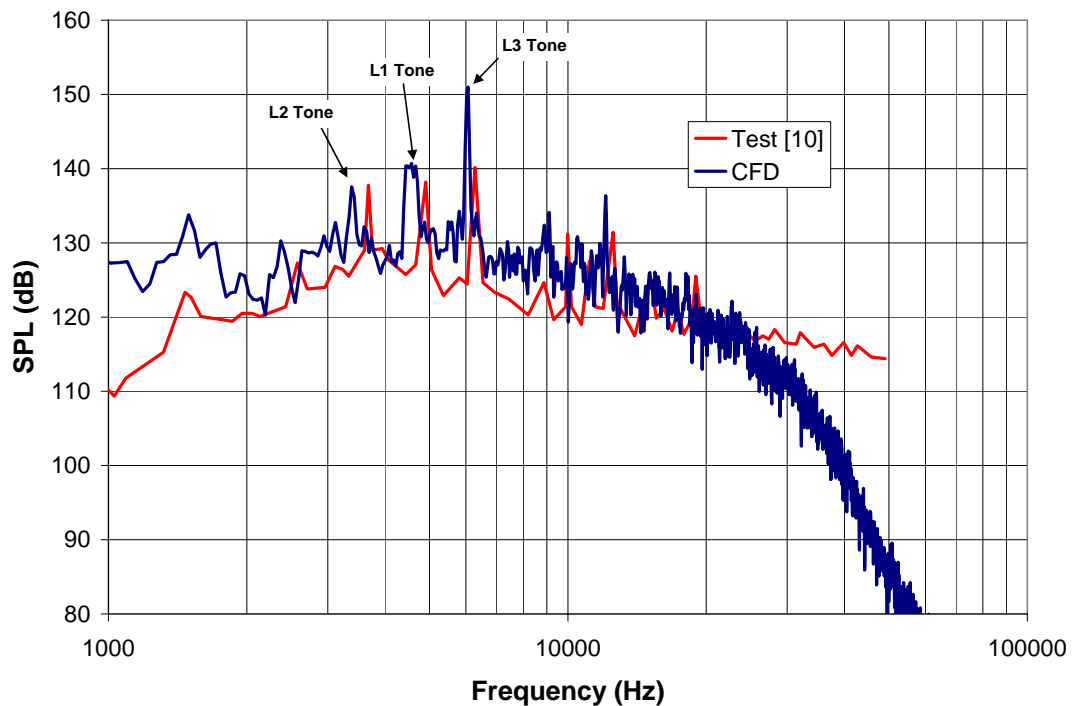


Figure 4-16 Comparison of impingement SPL tone magnitudes for  $h/d=3.75$

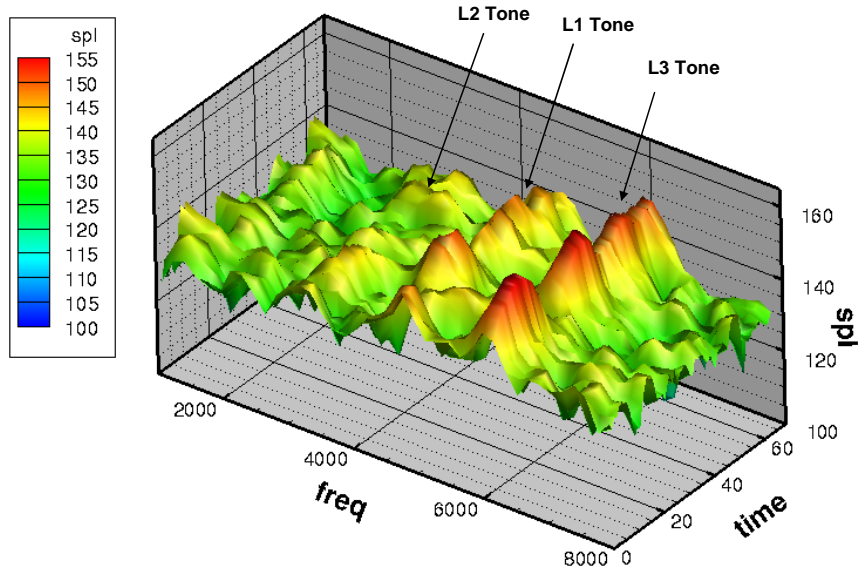


Figure 4-17 SPL variation with time:  $h/d = 3.75$

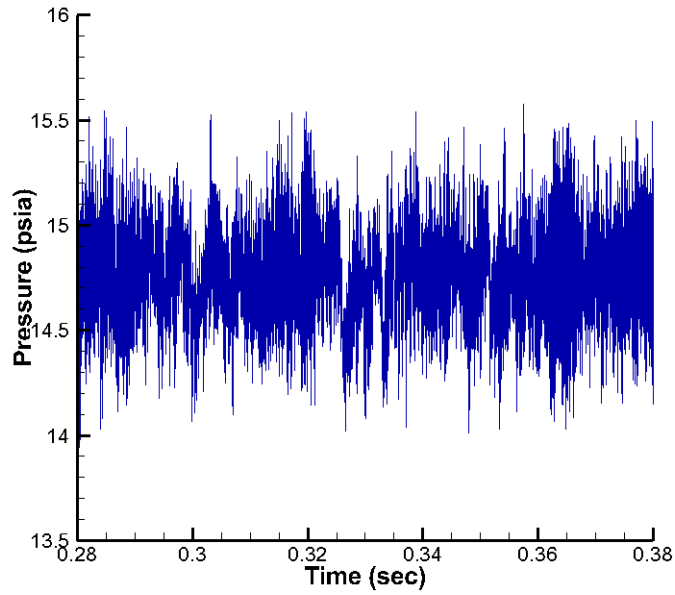


Figure 4-18 Near field pressure for  $h/d = 3.75$

Figure 4-19 shows Mach=0.5 isosurfaces colored by density at different times. The jet shows characteristics of the varicose (axisymmetric) mode with the shear layer vortices being shed at approximately 6000 Hz. The jet behavior shows some complex features that are indicative of the presence of both symmetric and helical modes. The

images show the shedding pattern for four successive vortices. Each vortex is not symmetric and shows skewness in the axial direction. The skewness of each vortex changes azimuthally for each successive vortex, showing a helical mode in the shedding. As this skewed vortex propagates it causes the jet to transition into a sinuous (flapping) mode near the impingement zone.

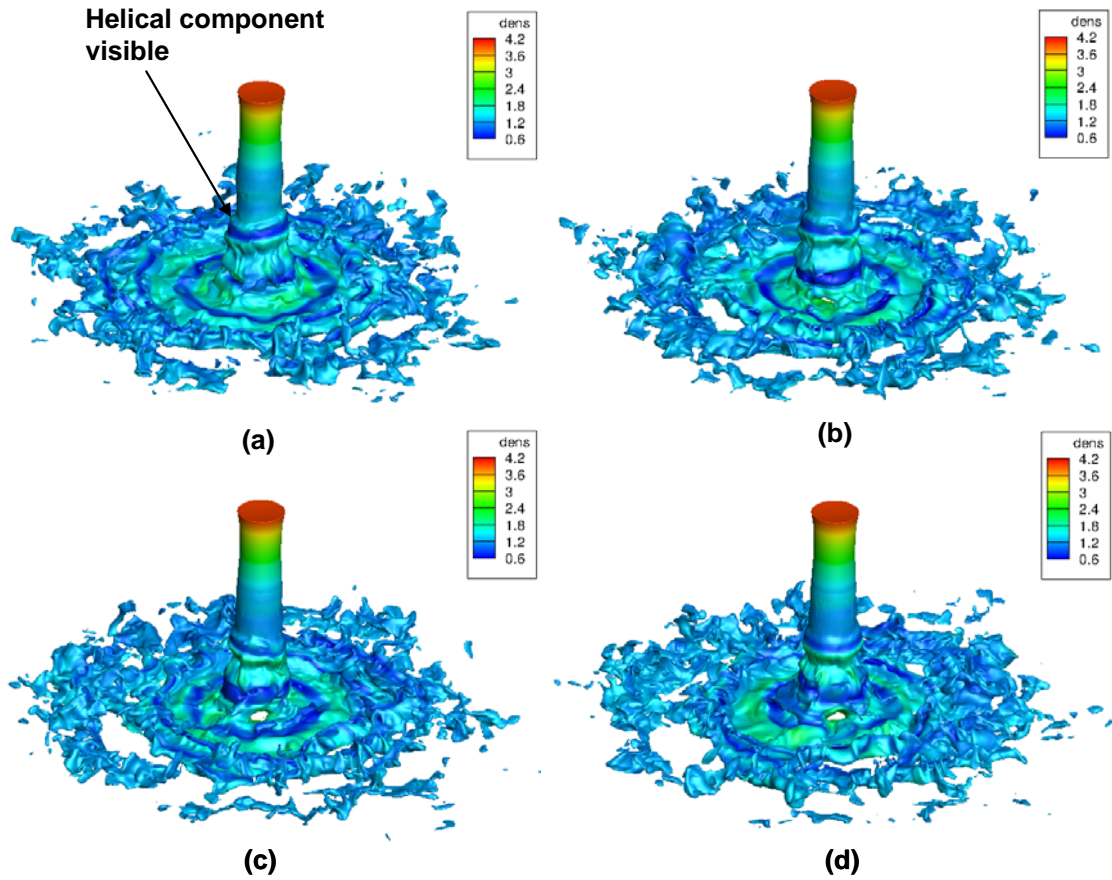


Figure 4-19 Mach iso-surfaces colored by density showing the time variation of the initial shear layer instability in the jet:  $h/d=3.75$

### 4.3.3 Separation Distance $h/d=4.25$

Figure 4-20 shows the sound pressure level calculated for the complete, statistically-steady pressure time history for the  $h/d=4.25$  case (Figure 4-21). Figure 4-22

shows the time variation of sound pressure level. The L3 tone shows little variation with time indicating that it is more stable at this separation distance than the other separation distances investigated. The dominance of the L3 tone is also seen in the test data with first multiple harmonics also appearing. The L1 and L2 tones show oscillations over time with the magnitudes lower than the L3 tone. This agrees with the test data showing that these tones are not dominant but the magnitudes of these tones are larger in the CFD calculation. The sources of these tones are from the jet modes with the helical tones generated by the sinuous or helical mode and the symmetric tones generated by the varicose modes of the jet. The influence of the helical mode can be seen in Figure 4-23 which shows disturbances in the shear layer at different times. The images are sequenced so that each successive vortex is shown as it reaches approximately the same axial location as the previous one. The results show the vortex is not symmetric and has significant skewness. Although shedding at the nozzle exit appears to be varicose in nature, the skewness indicates an asymmetric mode. In addition, the different times shown in Figure 4-23 illustrate how the asymmetry is not at the same location for successive shedding events. The skewness in the disturbance changes azimuthal location for each successive vortex shed. This indicates the presence of another helical mode in the jet.



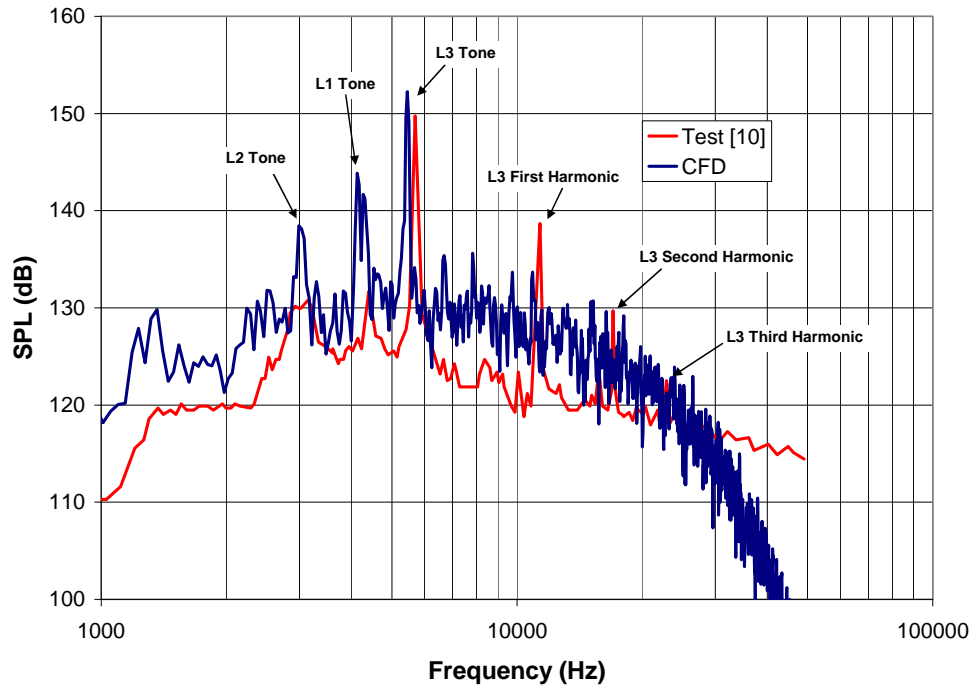


Figure 4-20 Comparison of tone magnitude of SPL:  $h/d=4.25$

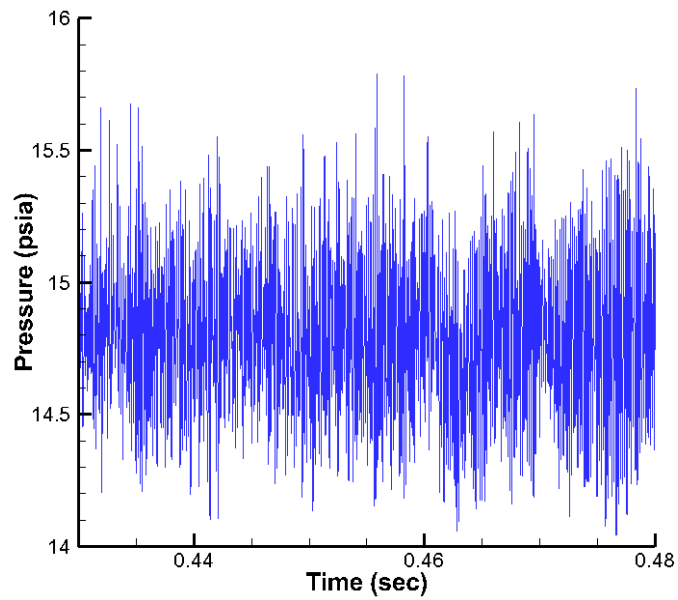


Figure 4-21 Near field pressure for  $h/d=4.25$

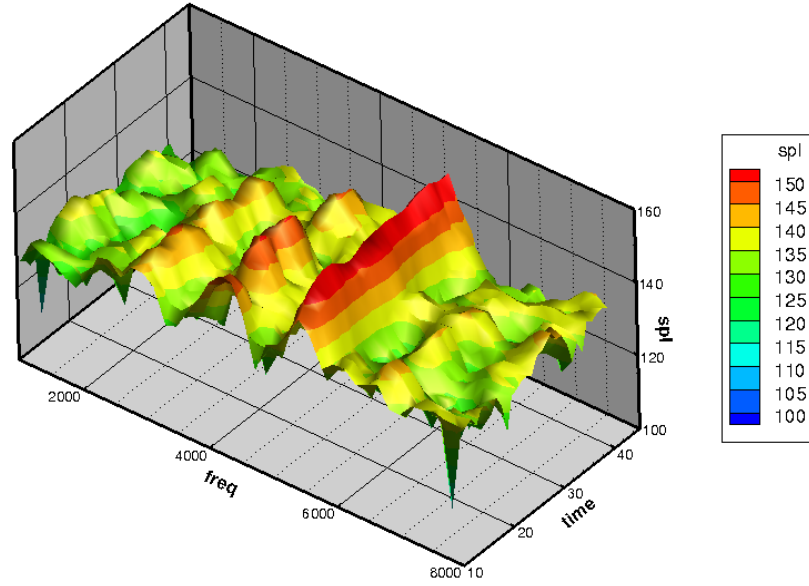


Figure 4-22 SPL variation with time:  $h/d = 4.25$

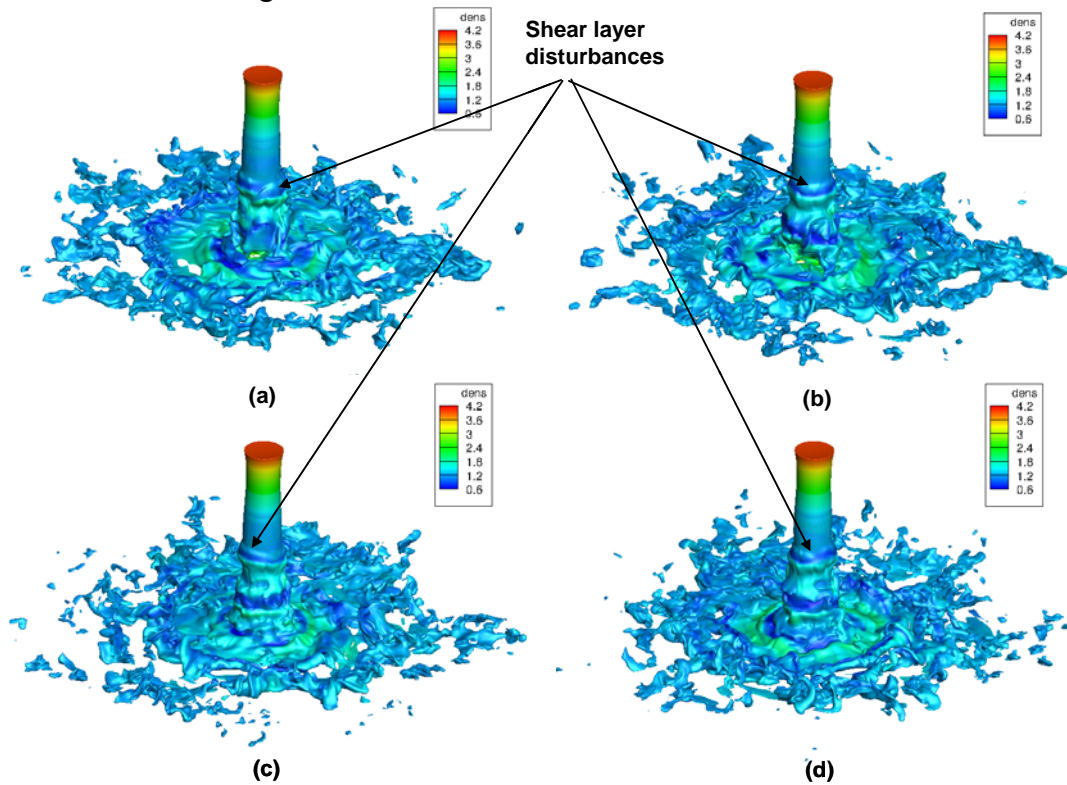


Figure 4-23 Mach=0.5 iso-surfaces colored by density showing asymmetry in the initial shear layer disturbance:  $h/d=4.25$

#### 4.4 OASPL and Sound Directivity

Monitor points were placed in the CFD domain on concentric arcs surrounding the nozzle exit and impingement point on the plate. Flow properties were recorded at these points every time step of the calculation. Overall sound pressure level (OASPL) was calculated at each probe locations and used to determine the directivity of the sound.

Distributions of OASPL for points around the nozzle exit are shown in Figure 4-24 and Figure 4-25 for the inner arc and the outer arc respectively. The OASPL distributions for all the cases are very similar in shape and magnitudes and both show a peak OASPL approximately  $15^\circ$  from the jet centerline. The  $h/d=4.25$  case, however, shows slightly less OASPL levels beyond  $15^\circ$ . The distributions for all three are very similar in Figure 4-25 with no appreciable differences in OASPL levels or directivity between the cases.

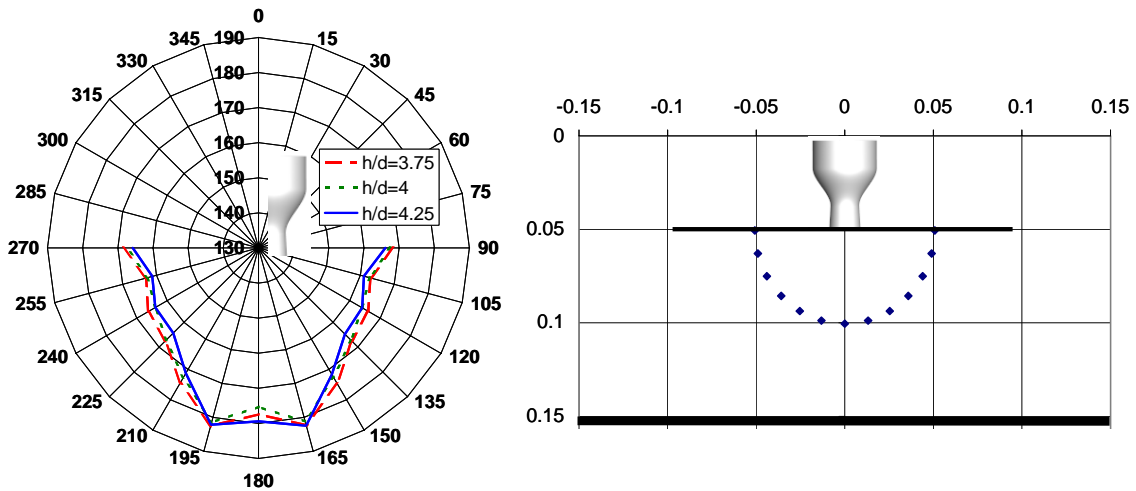


Figure 4-24 Separation distance comparison of OASPL distribution around nozzle exit: inner arc

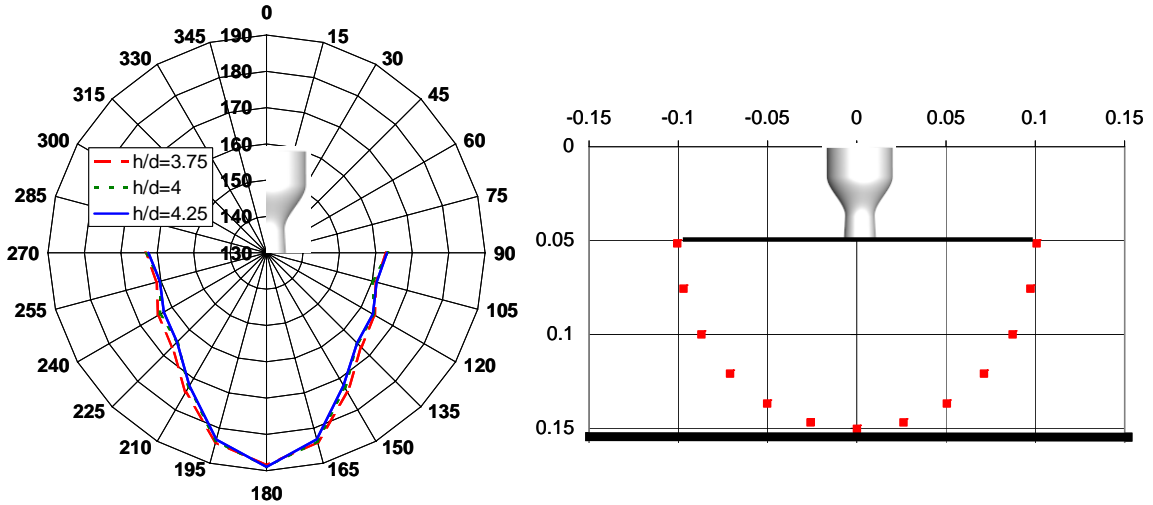


Figure 4-25 Separation distance comparison of OASPL distribution around nozzle exit: outer arc

The distributions of OASPL around the impingement point are shown in Figure 4-26 and Figure 4-27 for the inner and outer arc respectively. Once again the  $h/d=4.25$  case shows a peak on the jet centerline. The  $h/d=4.25$  case also shows lower OASPL levels than the other cases beyond  $15^\circ$ . The outer arc results for all the cases are similar with maximum OASPL occurring at  $15^\circ$  and the peak falling with separation distance.

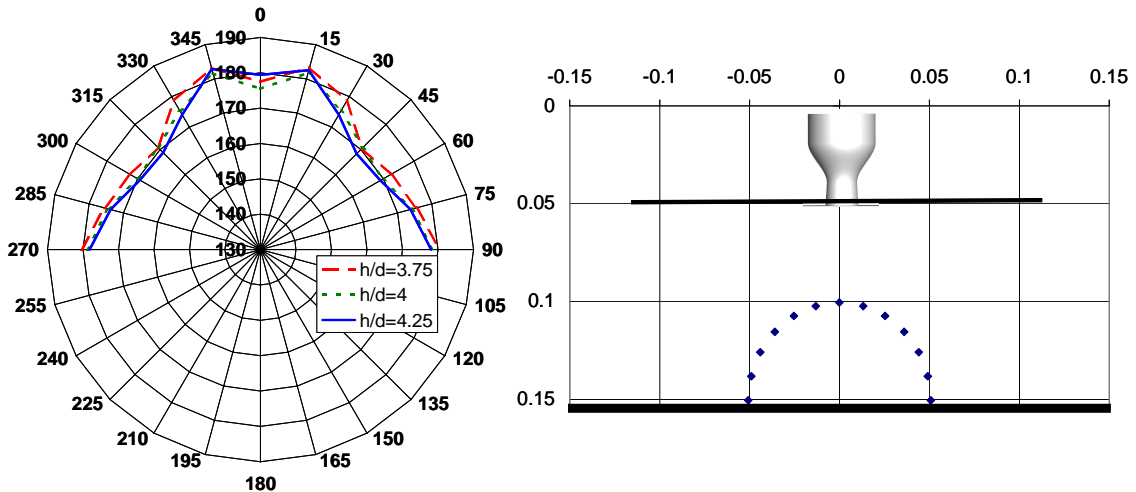


Figure 4-26 Separation distance comparison of OASPL distribution around impingement point: inner arc

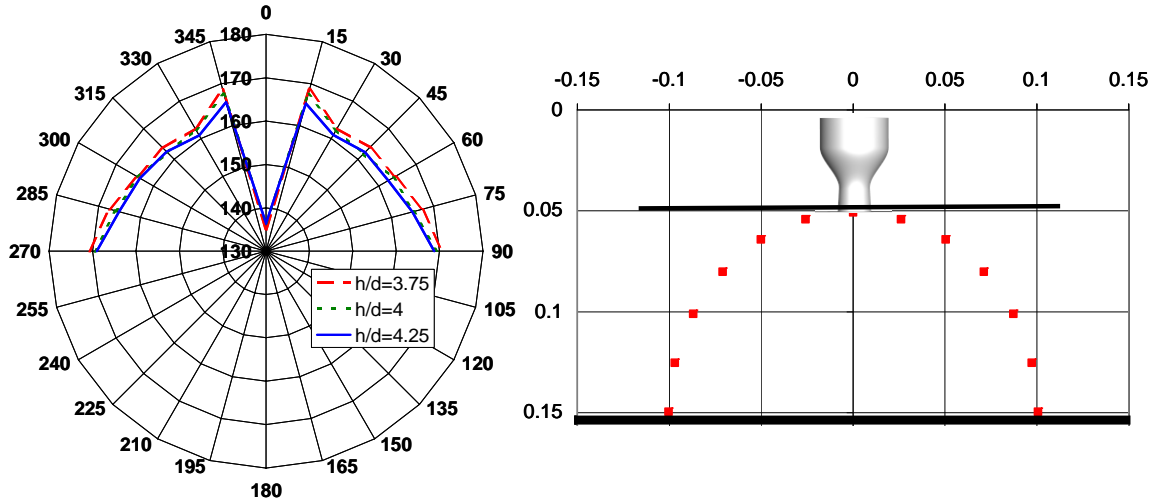


Figure 4-27 Separation distance comparison of OASPL distribution around impingement point: outer arc

Figure 4-28 shows contours of OASPL through a center plane of the nozzle.

Distinctive nodes in the OASPL distribution can be seen for all separation cases. As the separation distance increases new features can be seen appearing. Low OASPL regions on the jet centerline above the plate and below the nozzle exit also changes as separation distance increases. All the contours show a high OASPL region on the nozzle axis near the point halfway between the nozzle exit and the plate. The locations of these regions shift downstream as the separation distance increases.

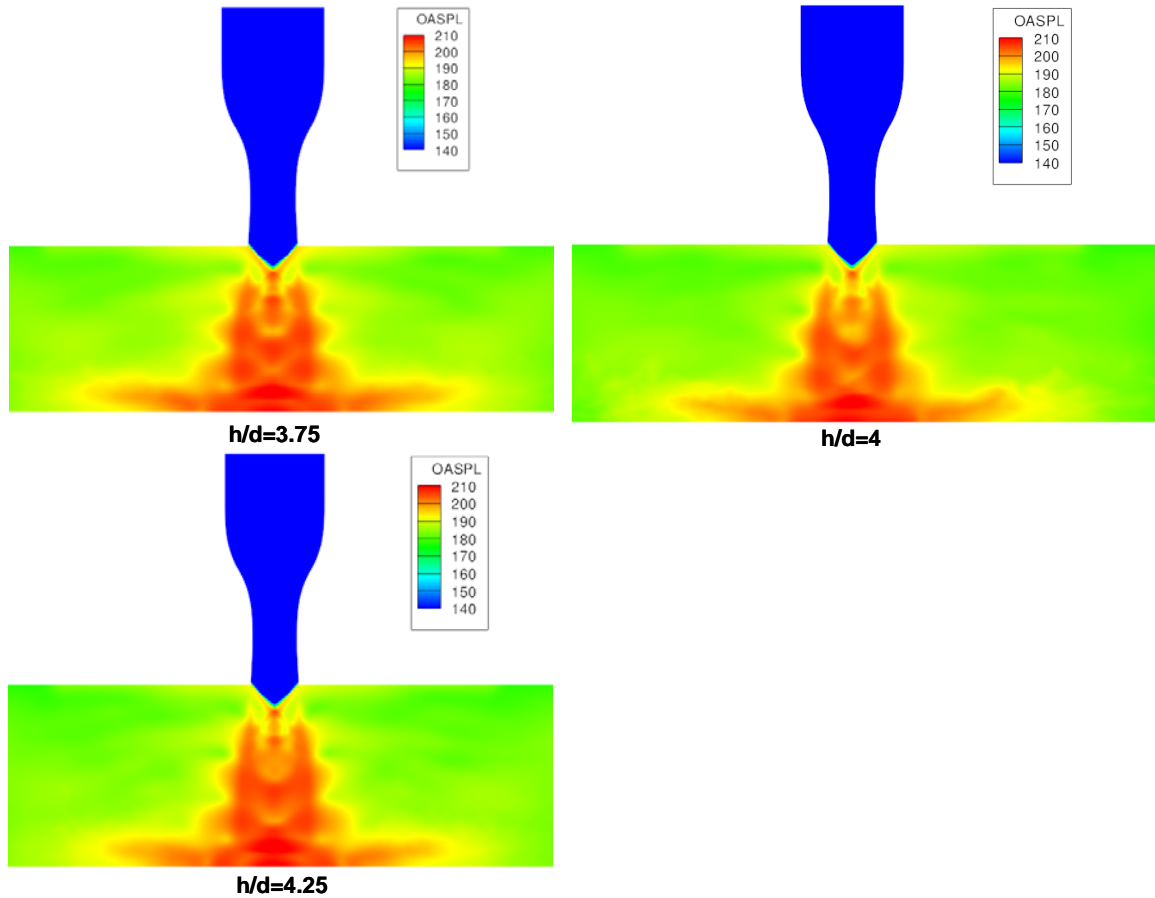


Figure 4-28 Comparison of OASPL contours for all separation distances

Figure 4-28 shows the highest noise levels in the jet shear layer and the impingement region on the plate. The jet oscillation creates strong acoustic waves that radiate away from the impingement point. These waves interact with vortices in the shear flow along the plate and generate regions of high noise just off the plate surface. Experimental investigations [12,13,15] show that after the plume impinges on the plate, a wall jet forms on the plate and extends radially from the impingement zone. The unsteadiness in the impingement zone is transmitted into the wall jet causing pulsations which becomes a noise source. The shear layer fluctuations and the interaction of the

feedback loop also make the jet shear layer a region of elevated noise. The results shown in Figure 4-28 agree with these observations. Figure 4-29 shows an instantaneous isosurface of Mach 0.5 colored by density of the impinging jet for all three separation distances. The pulsing in the shear layer created by the unsteadiness in the impingement zone propagates outward from the impingement zone.

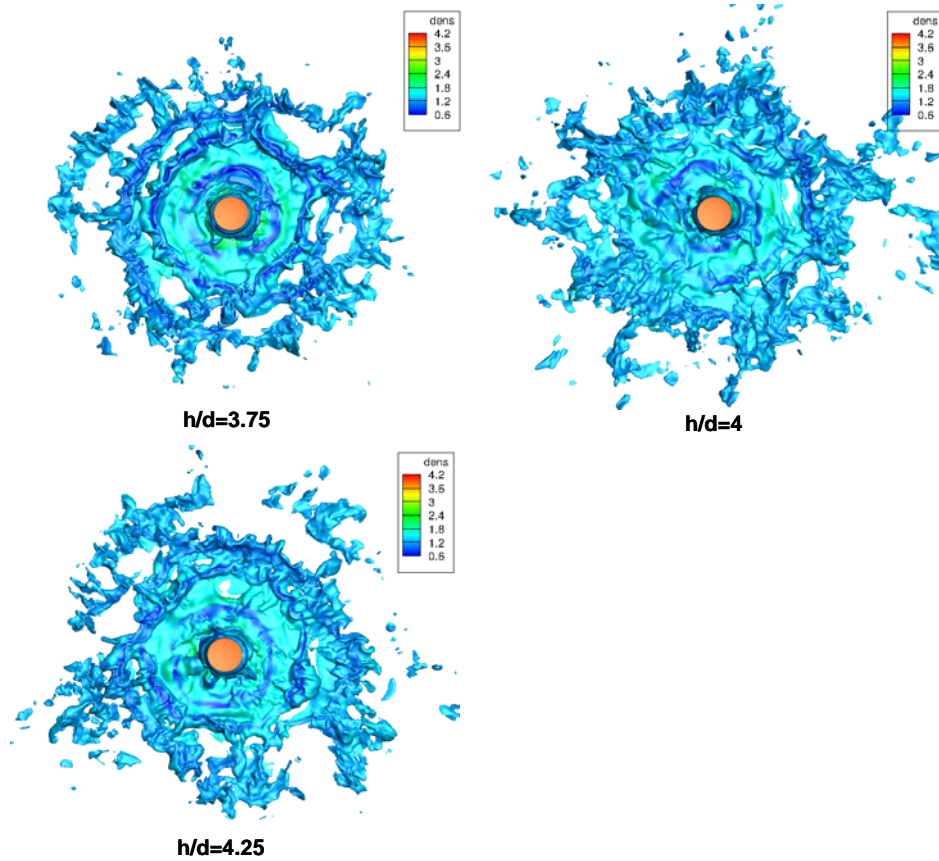


Figure 4-29 Top view of Mach=0.5 iso-surface colored by density showing disturbance propagation in the wall jet

#### 4.5 Feedback Mechanism

The feedback loop is an important mechanism in jet impingement. Acoustic waves from the impingement point propagate upstream and interact with the jet at the

nozzle exit. This creates a disturbance that propagates downstream and alters the frequency of the acoustic waves generated at the impingement point. The new frequency acoustic waves then excite different frequency disturbances in the jet that in turn change the frequency of the acoustic waves generated in the impingement region. This continues until the frequencies lock in at a unique frequency associated with the nozzle geometry, nozzle pressure ratio, nozzle exit conditions and the separation distance [2-14, 38].

The properties of the initial jet shear layer at the nozzle exit are important parameters in the feedback loop. The initial jet shear layer properties determine the shear layer's receptivity to some frequencies [39, 40, 42] which in turn can determine the jets behavior. Certain frequencies excite the jet into a sinuous mode while other frequencies excite the jet into a varicose mode [41]. Small changes in the initial shear layer affect its receptivity which can alter the feedback loop and the resulting impingement tones. Previous research [2,3] has suggested that the feedback mechanism takes place through acoustic wave interaction with jet shear layer. Other research [7] has argued that the feedback is internal to the jet. The present research shows that the feedback mechanism is the interaction of the acoustic waves with both the shear layer and internal flow of the jet.

Figure 4-30 shows the evolution of a disturbance in the jet shear layer. An acoustic wave from the impingement point propagates upstream (a). As the acoustic wave travels upstream it interacts with the jet and jet shear layer. The acoustic wave propagates into the jet with a change in the angle relative to the external portion of the acoustic wave but maintaining contact through the shear layer (b). When the part of the acoustic wave outside the jet reaches the lift plate, it is reflected (c) and begins to



propagate downstream, perturbing the shear layer as it travels (d). The acoustic wave inside the jet reaches the weak shock cone formed by waves from the nozzle lip. The internal wave only weakly reflects from the jet cone and no longer has the same strength or coherence. The imbalance between the external and internal acoustic wave results in external acoustic wave perturbing the shear layer as it propagates downstream (e). An oncoming acoustic wave inside the jet interacts with the disturbance and amplifies it (d). The disturbance continues to grow and alters the structure of the jet downstream. As the separation distance increases, the more these disturbances grow and disrupt the jet structure. An asymmetric distribution of these disturbances in the shear layer corresponds to the jet entering a helical mode while a symmetric distribution results in the jet entering into a symmetric (varicose) mode.

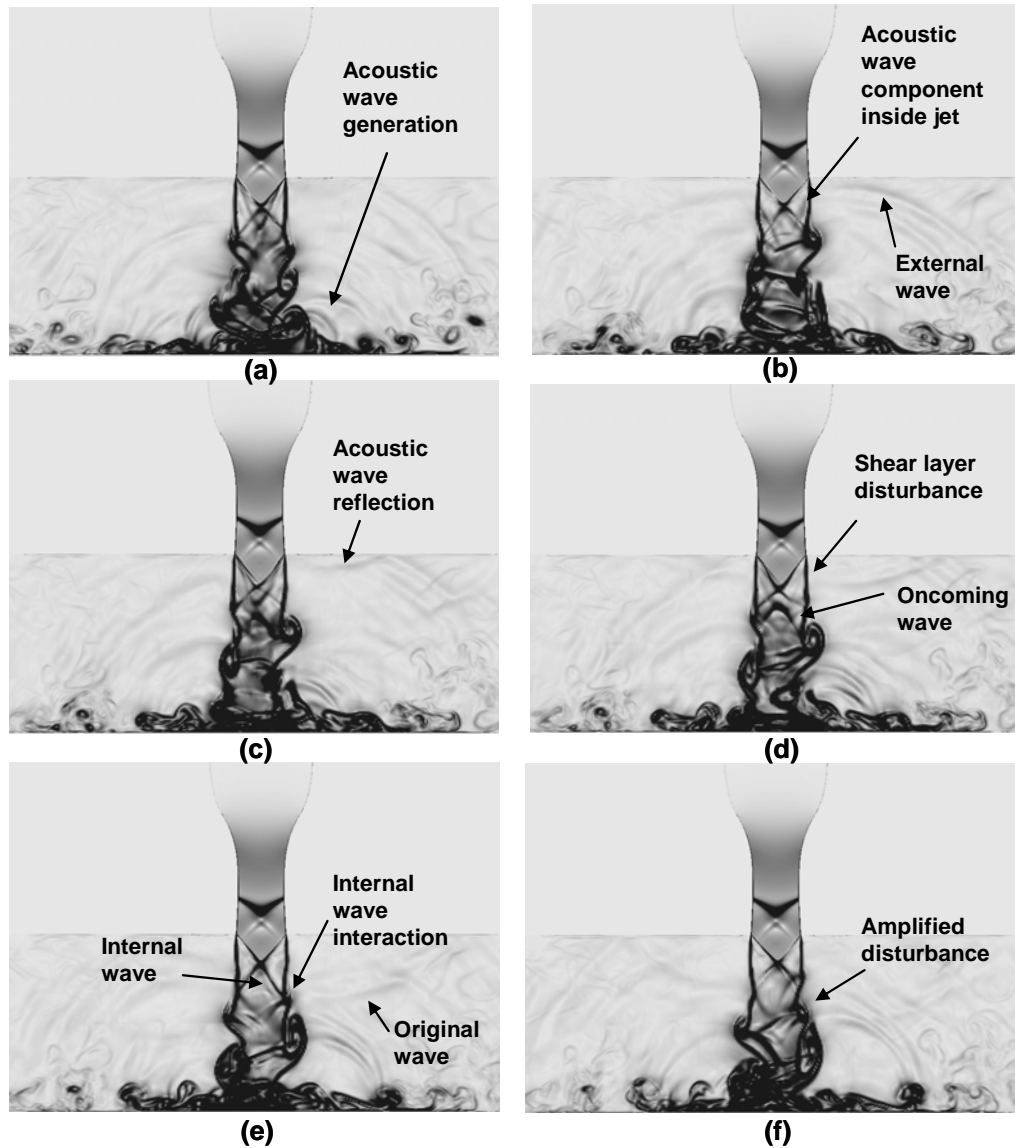


Figure 4-30 Contours of density gradient showing acoustic wave interactions and shear layer disturbance growth: separation  $h/d=4$ : (a) acoustic wave generated in impingement region; (b) propagation of acoustic wave toward nozzle exit; (c) acoustic wave reflection from lift plate; (d) acoustic wave generates a disturbance in the shear layer; (e) oncoming acoustic wave interacts with shear layer disturbance; (f) resulting amplified shear layer disturbance

Test observations [10] and CFD results show that these disturbances in the shear layer are vortices. The structure of these shear layer vortices is investigated by using the Q criterion [41]. The Q criterion (Equation (4-2)) is calculated by subtracting the rate of

strain from the rate of rotation which for  $Q > 0$  shows region of high rotation. In Equation (4-2), the rate of strain,  $S_{ij}$ , and the rate of rotation,  $\Omega_{ij}$ , are given by Equation (4-3) and (4-4) respectively.

$$Q = \frac{1}{2}(\Omega_{ij}\Omega_{ij} - S_{ij}S_{ij}) \quad (4-2)$$

$$S_{ij} = \frac{1}{2}\left(\frac{\partial u_i}{\partial x_j} + \frac{\partial u_j}{\partial x_i}\right) \quad (4-3)$$

$$\Omega_{ij} = \frac{1}{2}\left(\frac{\partial u_i}{\partial x_j} - \frac{\partial u_j}{\partial x_i}\right) \quad (4-4)$$

Although this formulation is incompressible, it is sufficient to reveal the structure of the shear layer vortices. Figure 4-31 shows the vortices in the flow field based on a  $Q$  value of 3000 where the vortices in the shear layer can clearly be seen.

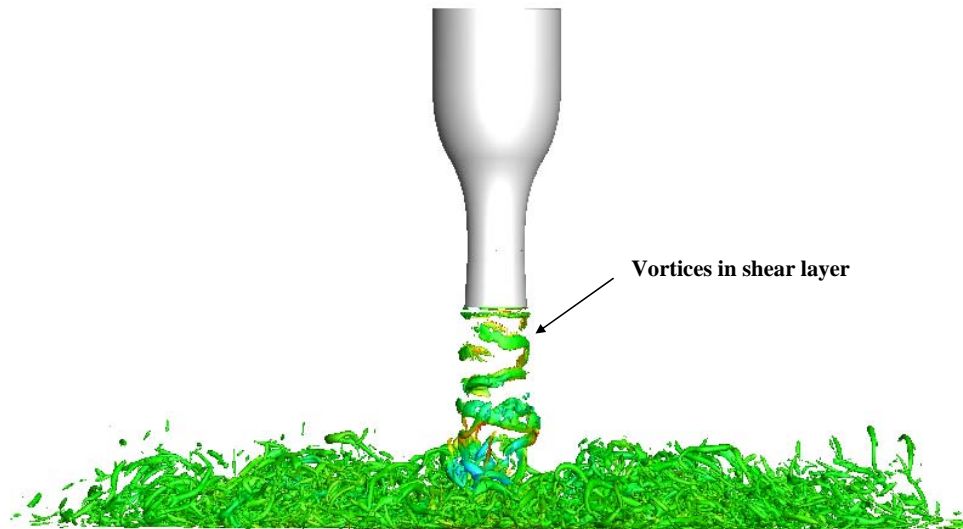


Figure 4-31 Iso-surfaces of  $Q=3000$  showing vortex structure in the shear layer.

The CFD results shows that the acoustic wave effects are not limited to the shear layer and do affect the internal jet flow up to the nozzle exit lip. The interaction of the internal acoustic wave with the conical feature formed by compression waves in the nozzle causes the conical feature (referred to as the cone hereafter) to move. The weak and disorganized reflection from the cone indicates that the acoustic wave energy goes into moving the surface and the motion of the cone corresponds with the jet mode. Asymmetric acoustic waves will cause the cone to have a precessing motion, corresponding to the jet entering a helical mode. Symmetric acoustic waves will cause the cone to oscillate vertically corresponding to the jet entering a symmetric mode. The motion of this cone structure for a jet with a helical mode is shown in Figure 4-32.

The motion of an impinging jet is governed by the initial jet flow and the evolution of disturbances in the jet shear layer. Near the nozzle exit the motion of the jet is governed by the motion of the jet core. Further from the nozzle exit, vortical disturbances in the jet grow and become the dominant influence on jet behavior. Figure 4-30 shows how as jet nears the impingement plate, the vortices are large and greatly influence the jet behavior. The CFD results show that the feedback mechanism affects the flow at the nozzle exit and the shear layer. While some studies have shown the interaction between acoustic waves and the shear layer [2,3,38,39,41,40,42] and linked the shear layer receptivity to jet modes [40,42] there was no mention of the direct interaction between acoustic waves and the core flow of the jet. One study indicates the presence of instability waves internal to the jet [7], but the waves identified are not external acoustic waves propagating into the jet.

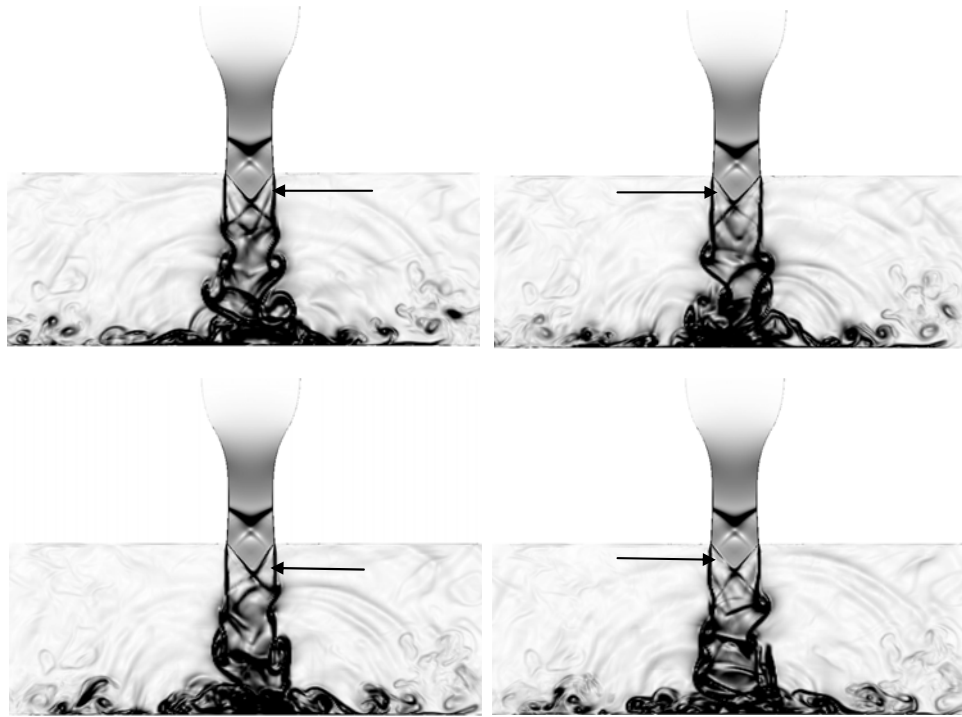


Figure 4-32 Contours of density gradient magnitude showing jet cone precession due to acoustic wave interaction

#### 4.6 Resolved Turbulent Kinetic Energy

Regions of high turbulent kinetic energy (TKE) are generated by turbulent fluctuations which are also noise sources in the flow field. The distribution of TKE in the flow helps inform where the regions of possible sound generation are located. The resolved turbulent kinetic energy is from the turbulent fluctuations resolved on the grid as opposed to the unresolved kinetic energy that is calculated in the subgrid model.

The resolved turbulent kinetic energy is shown in Figure 4-33. The results for all three separation distances are very similar as are the magnitudes. This is similar to the results for OASPL observed previously (Figure 4-28). Noise sources are indicated by regions of high turbulent kinetic energy. The prominent TKE locations are in the shear

layer, near the impingement point and in the wall jet shear layer. The strong vortical disturbances in the shear layer create large fluctuations that increase the turbulent kinetic energy in that region. The flow oscillation in the region of the impingement point has the highest turbulent kinetic energy showing that it is the region of the largest noise production. The shear layer of the wall jet also contains regions of high turbulent kinetic energy as a result of the pulsing of the jet transmitted through the wall jet.

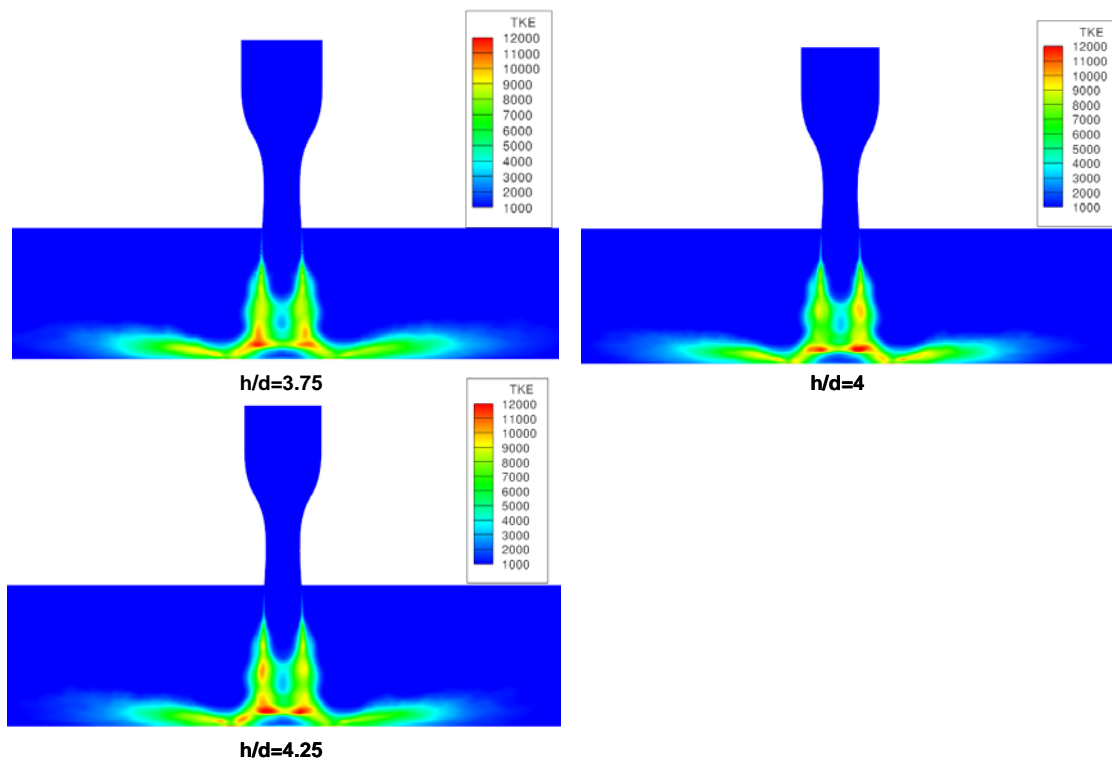


Figure 4-33 Comparison of resolved turbulent kinetic energy ( $\text{m}^2/\text{sec}^2$ ) for each separation distance

## 4.7 Jet Centerline Comparisons

The time averaged jet centerline properties for each separation distance are compared. The effects of the separation distance on the jet centerline properties are investigated. The time averaged centerline velocity is shown in Figure 4-34 for all three separation distances. The velocity along the jet axis only shows some slight variation close to the nozzle exit but becomes more pronounced downstream. At the separation distances analyzed, the velocities seem to have a somewhat similar profile with axial distance. The profiles appear to lengthen as separation distance increases. Figure 4-35 shows the time averaged mean pressures along the jet axis. Again, the most significant variations occur far downstream near the plate. The locations of peak pressures (Figure 4-35: A and B) along the jet axis moves downstream as separation distance increases. The pressure at location A is smallest for the largest separation case and the peaks shifted downstream as separation distance increases. Location B shows the highest pressure is for the  $h/d=4.25$  case. The shift downstream is also larger with separation distance at this location. This shift in the jet structure is shown in Figure 4-36 with the shift in the jet cell structure most pronounced near the plate. In Figure 4-36 the intermediate and largest separation distances are compared with the shortest separation distance. Location (a) shows no significant change while location (b) only shows a significant change in position for the largest separation case. Location (c) shows a significant shift downstream for both the  $h/d=4$  and  $h/d=4.25$  cases. The plate separation distance appears to affect the entire jet structure with the effects being slight near the nozzle exit but increasing in magnitude with distance from the nozzle exit.

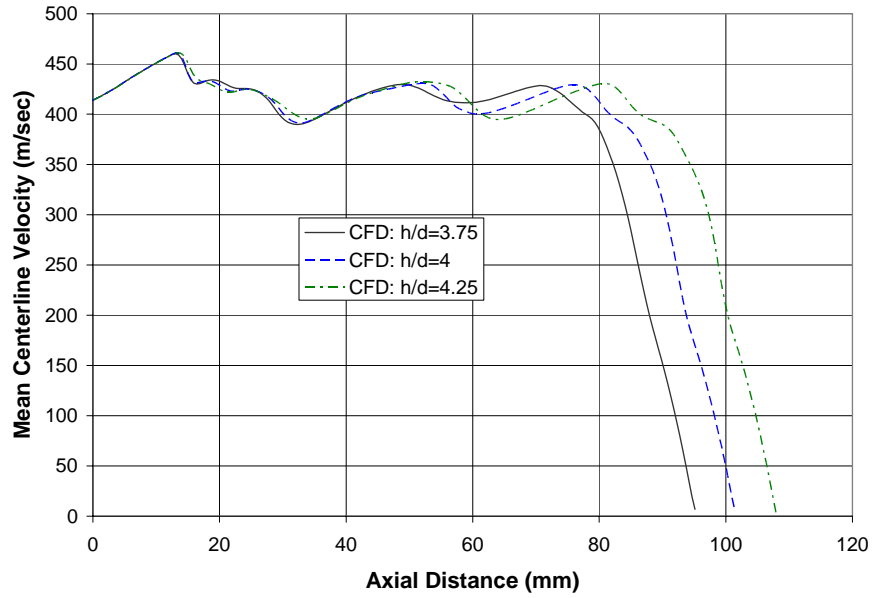


Figure 4-34 Effects of separation distance on jet centerline time-averaged velocities

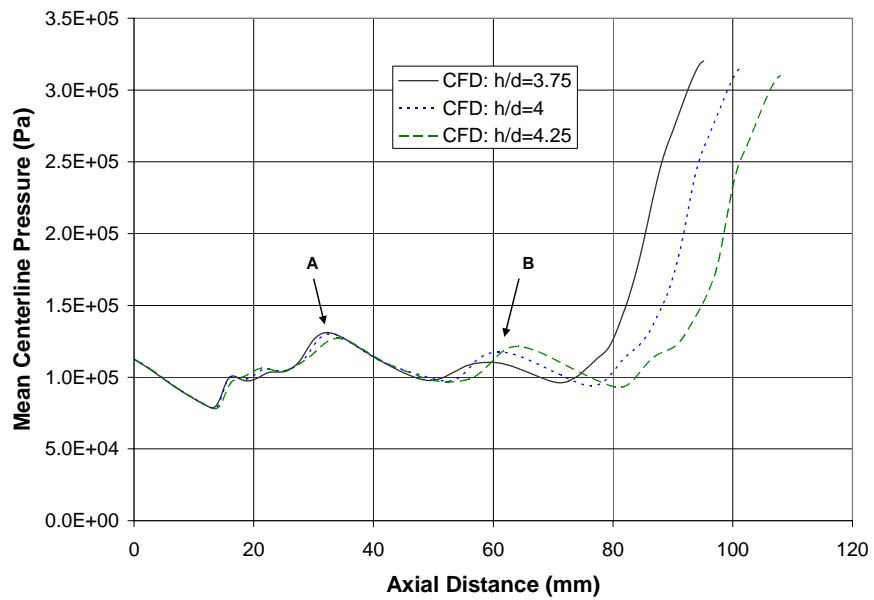


Figure 4-35 Effects of separation distance on jet centerline time-averaged pressure



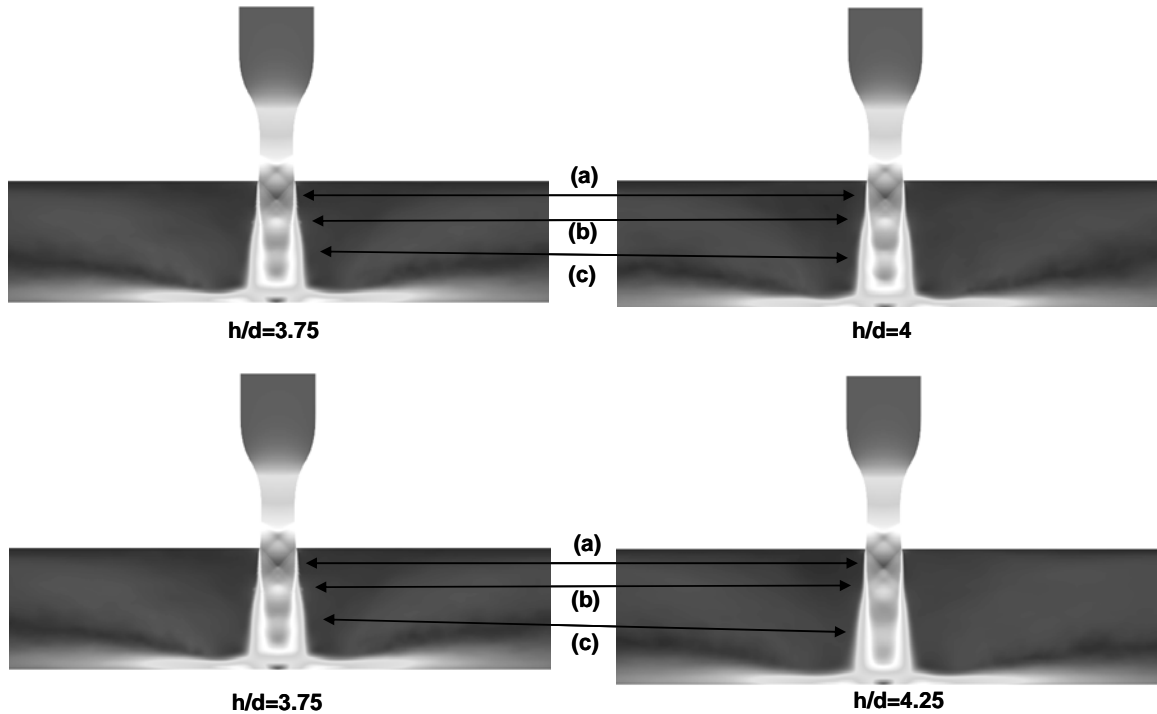


Figure 4-36 Effects of separation distance on time-averaged jet shock cell locations

#### 4.8 Spatial SPL Distributions

Monitor points were located at approximately midway between the jet exit and the impingement plate. Figure 4-37 shows the monitor point locations on a contour plot of the time averaged velocity. The middle radial location is in the shear layer near the jet core while the outer point is at the outer edge of the shear layer. Figure 4-38 shows the radial distribution of sound pressure level at the midpoint between the nozzle exit and the impingement plate. The L3 tone shows higher magnitudes in the shear layer than on the jet centerline; however the harmonics of the L3 tone are stronger at the jet centerline than in the other radial locations. These results show that the impingement tones are present in the jet core but are amplified in the shear layer. The impingement tone frequencies are introduced into the shear layer at the nozzle exit as part of the feedback mechanism. The

resulting disturbances travel downstream in the shear layer and can be amplified or reduced based on the shear layer receptivity. Figure 4-38 shows the tones that are amplified in the shear layer. Amplification is determined to take place when the tone amplitude is larger in the shear layer than at the centerline of the jet. Multiple harmonics are seen at the higher frequencies. A similar low frequency tone is also seen in the near field in the test data (Figure 4-5) but unfortunately no near-field test data was available in Reference [10] for direct comparison. Monitor point locations for the  $h/d=4$  and  $h/d=4.25$  cases are shown in Figure 4-39. Unlike the  $h/d=3.75$  case, the farthest radial points are not in the jet shear layer for these cases. However similar behavior is also observed for the  $h/d=4$  and  $h/d=4.25$  separation cases shown in Figure 4-40 and Figure 4-41 respectively. Amplification is seen for the point in the shear layer and no amplification is seen at the last radial point except in regards to the L3 tone for the  $h/d=4$  case. The prominence of this tone suggests that it is at frequency that is greatly amplified in the shear layer. This would result in an increased magnitude for a point near the jet but outside the shear layer.

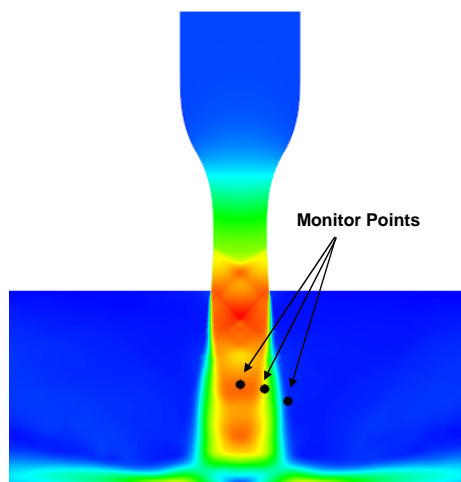


Figure 4-37 Radial distribution of probe locations:  $h/d=3.75$

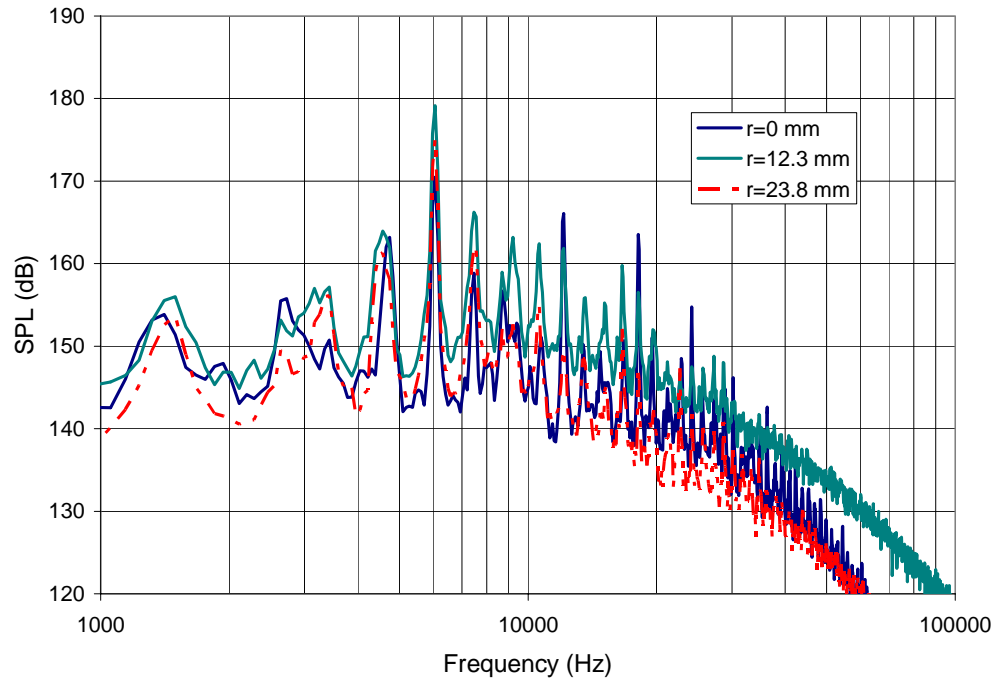


Figure 4-38 Jet radial SPL distribution at  $x=47.6$  mm:  $h/d=3.75$

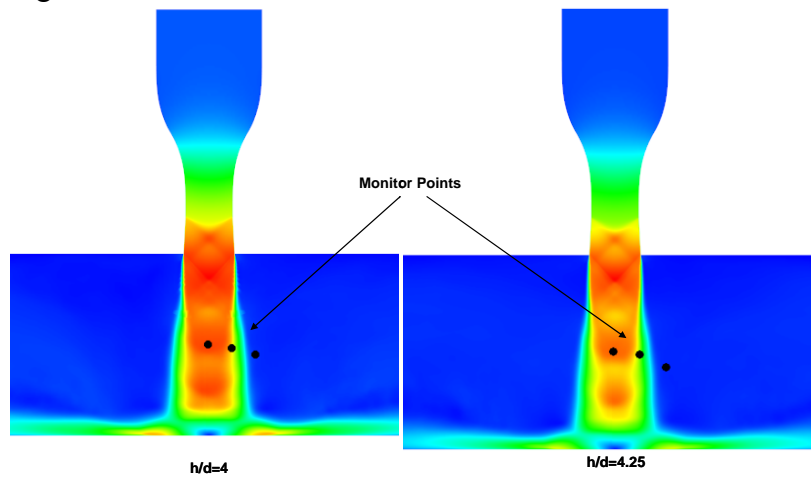


Figure 4-39 Radial distribution of probe locations:  $h/d=4$  and  $h/d=4.25$

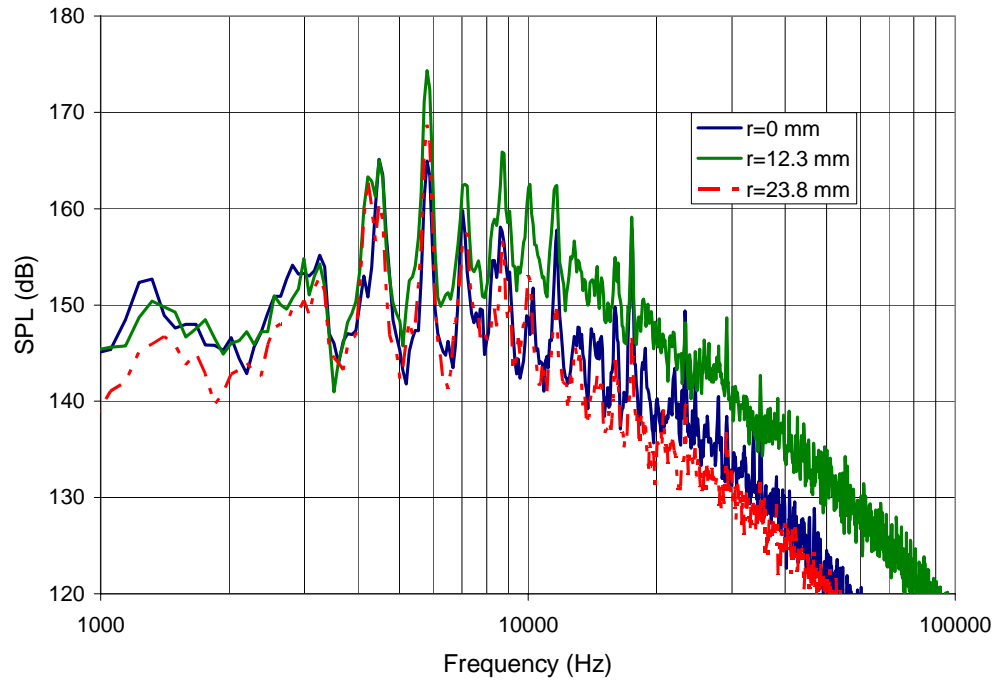


Figure 4-40 Jet radial SPL distribution at  $x=50.8\text{ mm}$ :  $h/d=4$

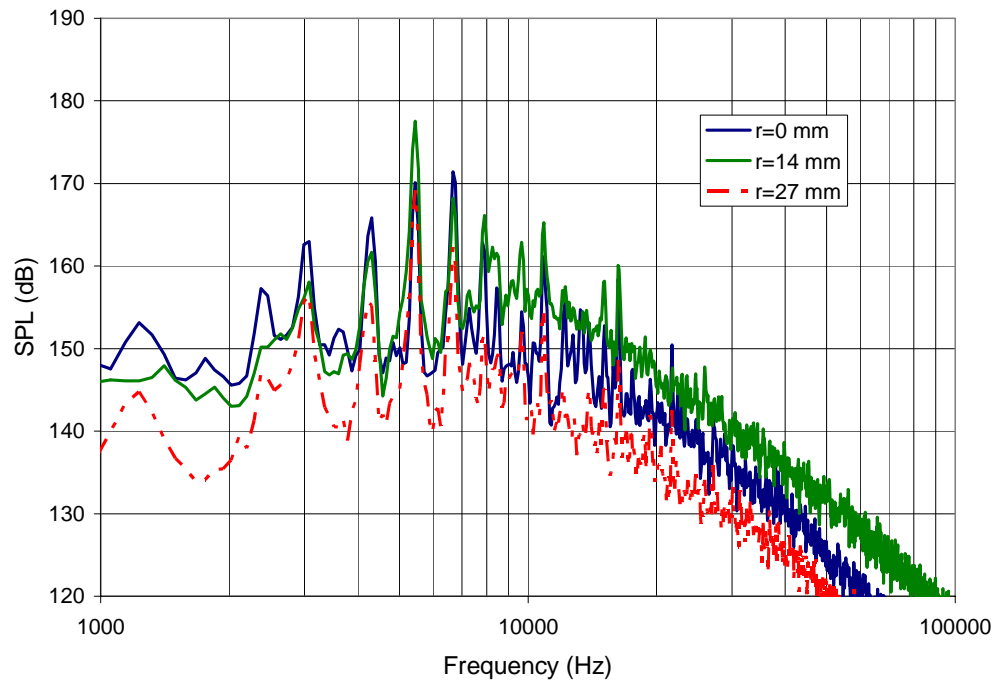


Figure 4-41 Jet radial SPL distribution at  $x=54\text{ mm}$ :  $h/d=4.25$

Analysis was performed for monitor points at a constant radial location but different axial locations in the flow field. Monitor point locations for each separation distance are shown in Figure 4-42. The results for the  $h/d=3.75$  case are shown in Figure 4-43. The magnitudes of the impingement tones increase as does the overall level of the broadband noise as the impingement plate is approached. Similar results are seen for the  $h/d=4$  and  $h/d=4.25$  cases shown in Figure 4-44 and Figure 4-45 respectively. The results confirm that the impingement zone is the highest source of noise in the flow field. Care should be taken in comparing the magnitudes between the different separation cases since the radial distance from the jet axis increases with separation distance and the monitor point locations proximity to the jet and shear layer result in higher sound pressure levels.

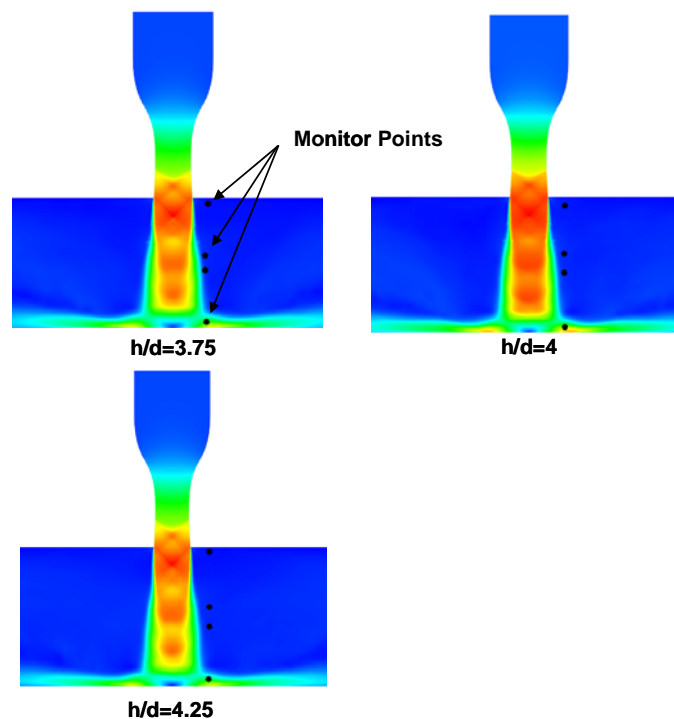


Figure 4-42 Monitor point distribution in axial direction for each separation distance

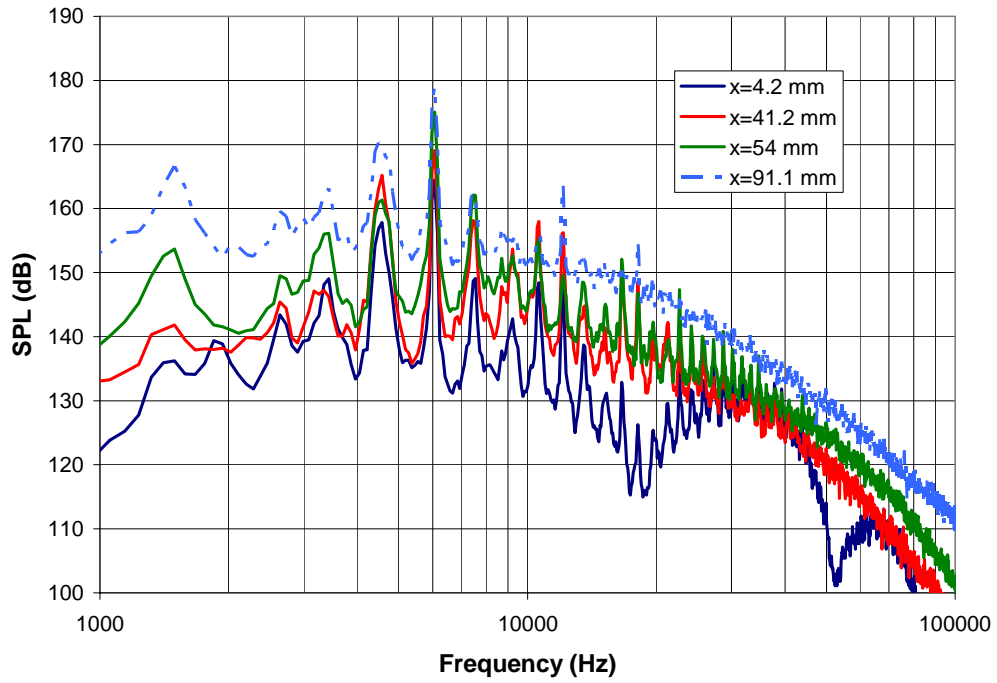


Figure 4-43 Axial SPL distribution at  $r=24\text{mm}$ :  $h/d=3.75$

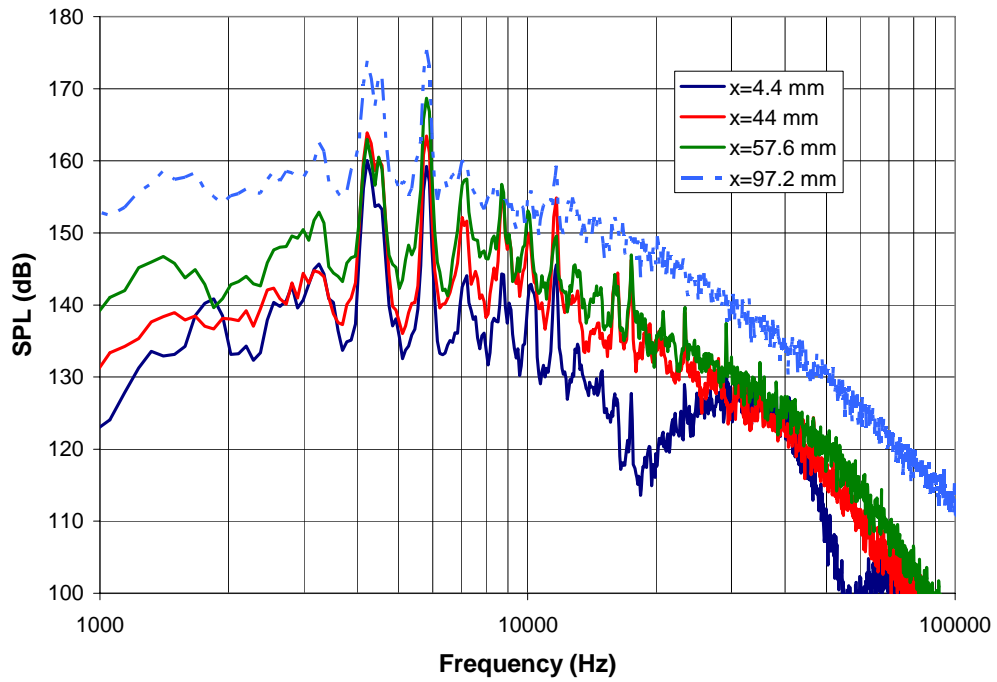


Figure 4-44 Axial SPL distribution at  $r=26\text{mm}$ :  $h/d=4$

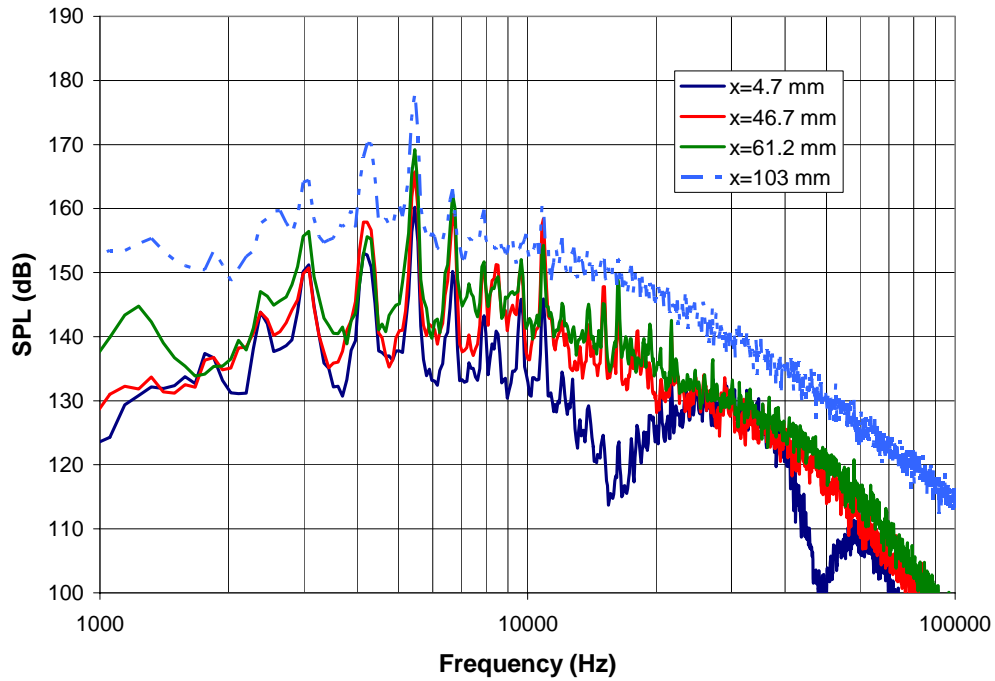


Figure 4-45 Axial SPL distribution at  $r=28\text{mm}$ :  $h/d=4.25$

## 4.9 Effects of Nozzle Geometry

The effects of nozzle geometry on the flow field were investigated using the modified nozzle shown in Figure 4-2. The effect of nozzle geometry on the acoustic environments are presented and discussed.

### 4.9.1 Sound Pressure Level

The effects of nozzle geometry was investigated using a modified nozzle (Figure 4-2) at the  $h/d=4$  separation distance. The CFD predicted sound pressure levels for the modified nozzle are shown in Figure 4-46. Like all previous analyses, the near field point at which the measurements are collected are closer to the nozzle exit for the CFD than the probe location in the tests, resulting in sound pressure levels higher than those

measured in the tests. The results show the L2 tone is more prominent for the modified nozzle than for the test geometry. The L1 tone magnitude is also lower than seen for the test geometry but the L3 tone is more prominent. Figure 4-47 shows the time variation SPL with frequency and time. The L3 tone is very stable over time similar to what was seen in the  $h/d=4.25$  case with some oscillations seen in the L1 and L2 tones. The stability of the L3 tone for the modified nozzle is different from the behavior seen for the test nozzle geometry. It is also interesting that L2 is also stronger for the modified nozzle compared to that for the test geometry. The modified nozzle has a shorter overall length than the test nozzle which should result in a thinner boundary layer in the nozzle. This thinner shear layer will have a different receptivity than the test nozzle geometry shear layer. This would allow different tones to be enhanced while others are damped. The dependence of the tones on the feedback mechanism makes the shear layer receptivity an important parameter. The frequency of impingement tones does not appear to be a function of the nozzle geometry but a function of the separation distance between the nozzle and the plate and the nozzle pressure ratio.



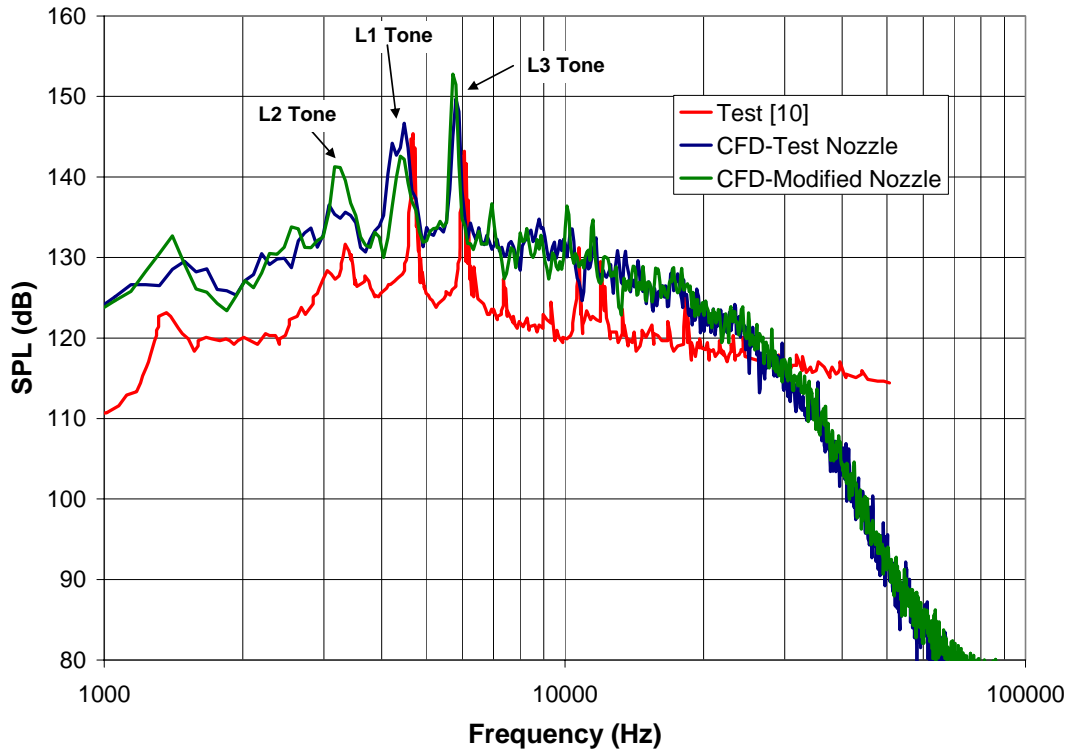


Figure 4-46 Comparison of test and modified nozzle with test data

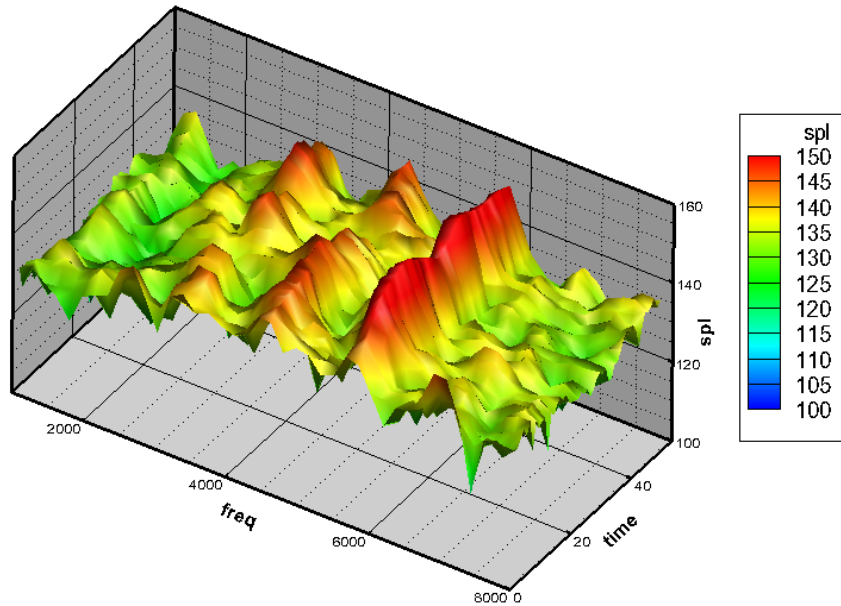


Figure 4-47 SPL variation with time: modified nozzle

#### 4.9.2 OASPL and Sound Directivity

Overall sound pressure level was calculated at each of the monitor points surrounding the nozzle exit and the impingement point. Comparisons of OASPL around the nozzle exit for the test nozzle geometry and the modified nozzle geometry are shown in Figure 4-48 and Figure 4-49 on the inner and outer arcs respectively. The modified nozzle has a 3dB higher OASPL at 180° compared to that for the test nozzle (Figure 4-48) but the rest of the OASPL directivity and levels show negligible difference. Figure 4-49 shows almost identical directivity and magnitudes between the flow fields for the two nozzles. Figure 4-50 compares the OASPL on the inner arc around the impingement point. The modified nozzle shows a 3dB higher peak on the axis compared to that for the test nozzle. Figure 4-51 compares the OASPL on the outer arc around the impingement point and shows negligible differences between OASPL and directivity between the nozzle geometries. The Figure 4-52 compares the OASPL contours for the test nozzle geometry and the modified nozzle geometry for the  $h/d=4$  separation distance. There are no significant differences between the two nozzle geometries confirming that OASPL is independent of nozzle geometry.

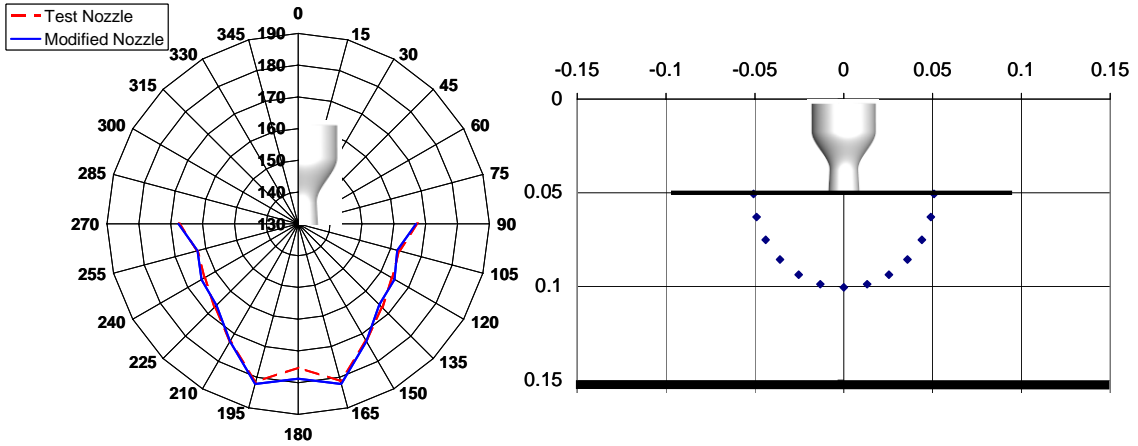


Figure 4-48 Comparison of OASPL distribution around the nozzle exit for test and modified nozzle geometries: inner arc

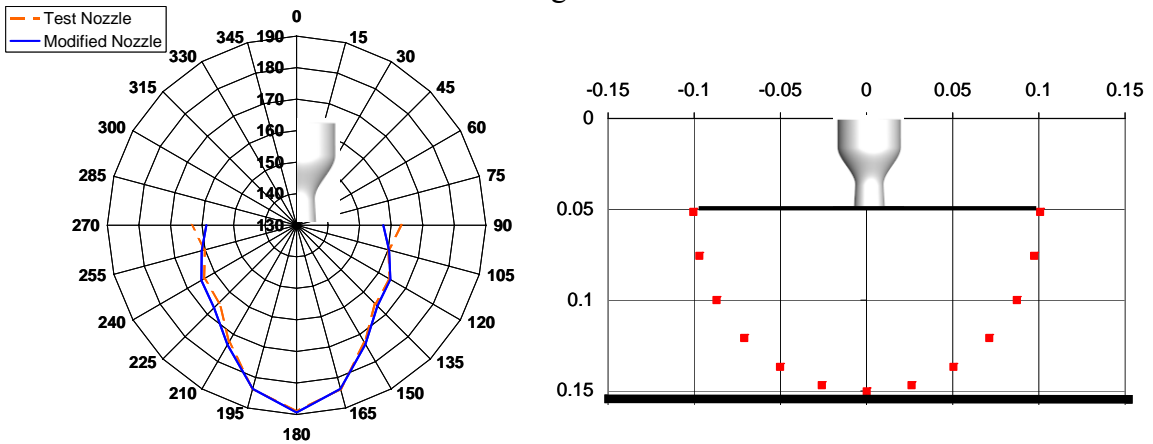


Figure 4-49 OASPL Comparison of OASPL distribution around the nozzle exit for test and modified nozzle geometries: outer arc

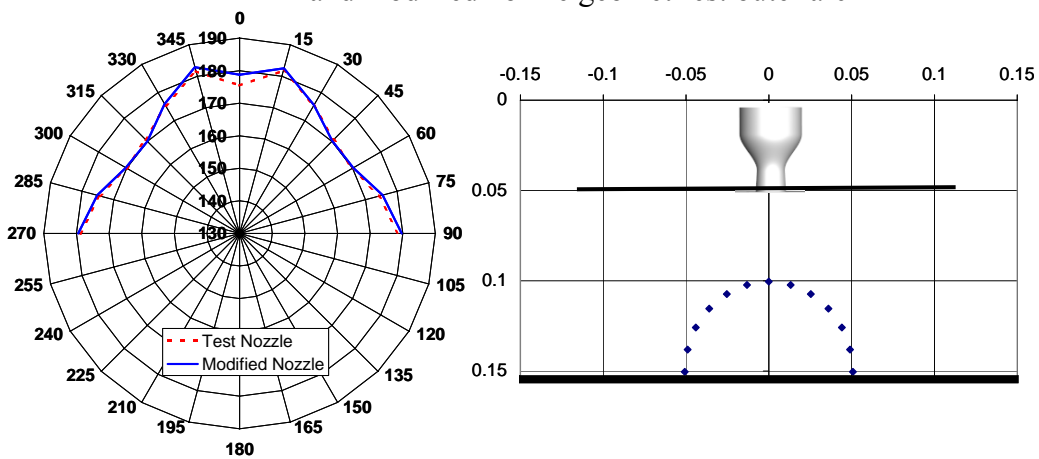


Figure 4-50 Comparison of OASPL distribution around the nozzle exit for test and modified nozzle geometries: inner arc

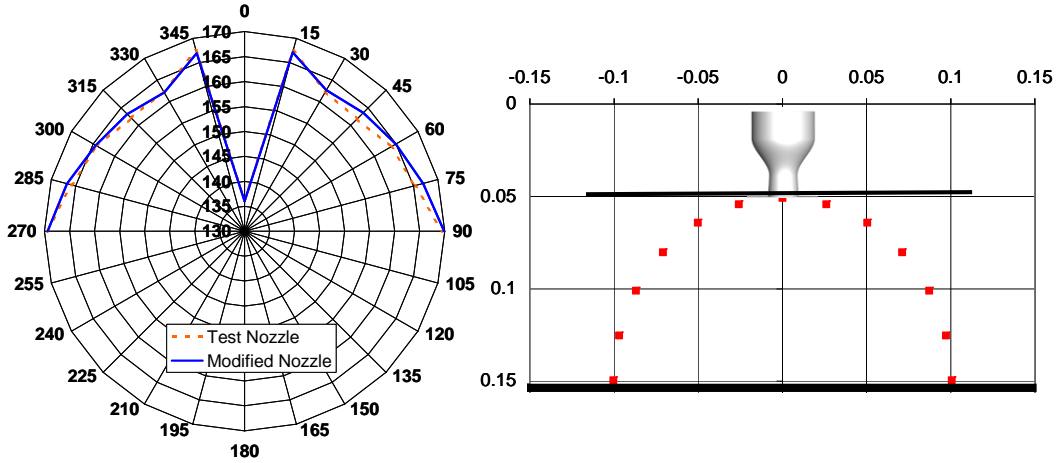


Figure 4-51 Comparison of OASPL distribution around the nozzle exit for test and modified nozzle geometries: outer arc

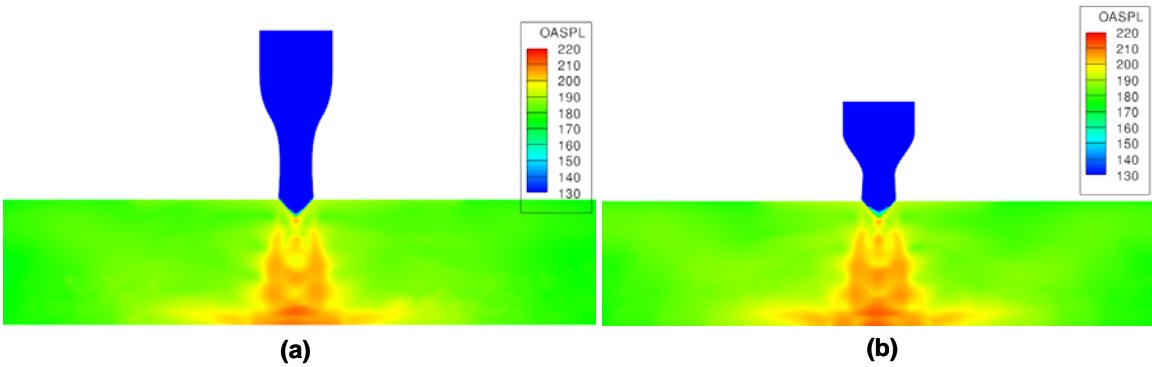


Figure 4-52 Comparison of OASPL contours  $h/d=4$  (a) test geometry; (b) modified nozzle geometry

### 4.9.3 Resolved Turbulent Kinetic Energy

Figure 4-53 compares the resolved turbulent kinetic energy for the test nozzle geometry and the modified nozzle. The resolved turbulent kinetic energy is very similar for the test nozzle and the modified nozzle for this separation distance (Figure 4-53) with only minor differences. The differences are attributed to the different times over which

the data is averaged. The similarity in TKE is expected based on the results seen in the previous discussion of OASPL.

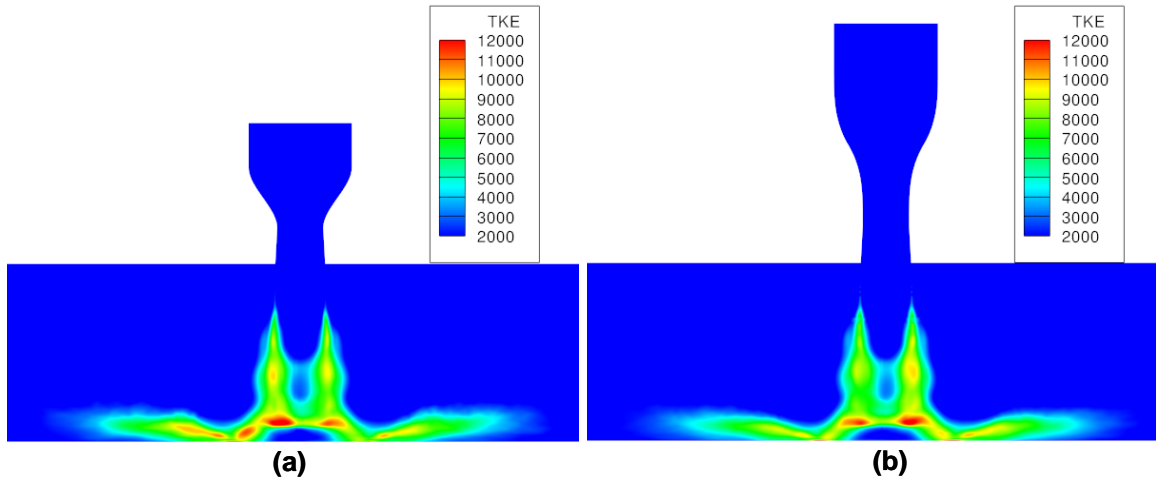


Figure 4-53 TKE comparison  $h/d=4$  (a) modified nozzle; (b) test nozzle

#### 4.10 Impingement Plate Environments

Overall sound pressure levels were calculated on the impingement plate for all the separation distances analyzed. Figure 4-54, Figure 4-55, and Figure 4-56 show results for the  $h/d=3.75$ ,  $h/d=4$ , and  $h/d=4.25$  separation distances respectively. The results show similar magnitudes with a peak of approximately 210 dB seen at the impingement point with OASPL falling to 170 dB at the edge of the plate. The OASPL contours for the  $h/d=3.75$  and  $h/d=4.25$  cases are smoother than observed for the  $h/d=4$  case. The  $h/d=4$  case being close to the transition point of modes behaves chaotically as it oscillates between jet modes. This results in jagged pattern of OASPL on the plate. Given a longer time history, the contours would be smoother but the results demonstrate the time variation of the jet.

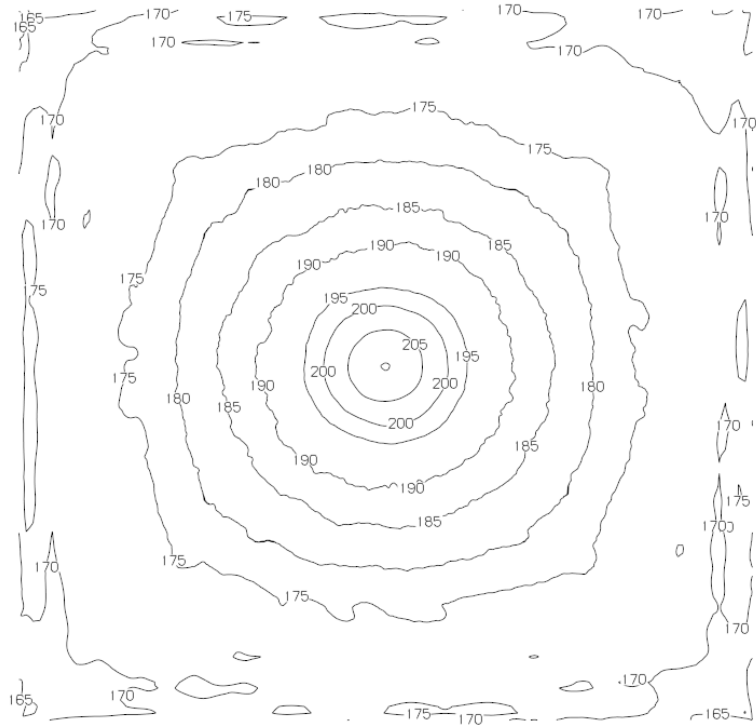


Figure 4-54 OASPL on impingement plate:  $h/d=3.75$

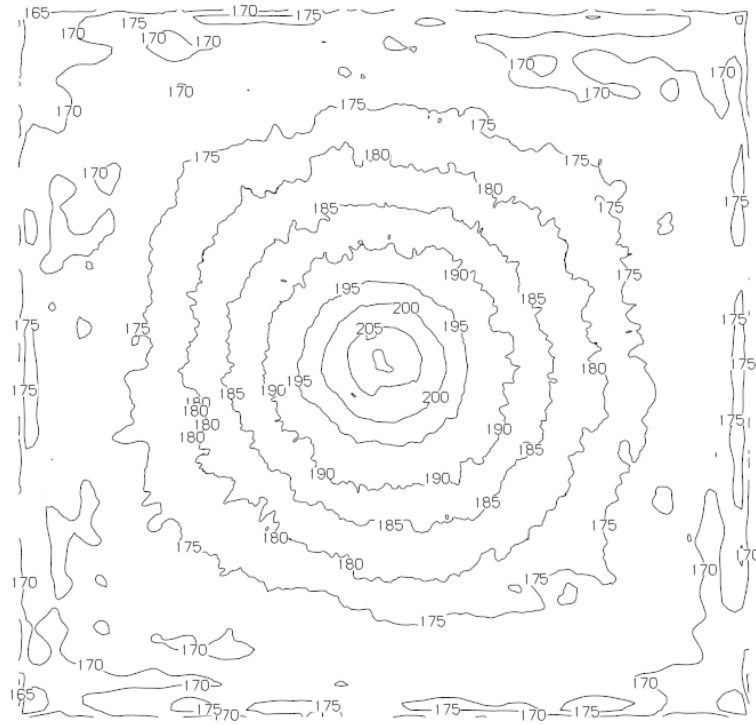


Figure 4-55 OASPL on the impingement plate:  $h/d=4$

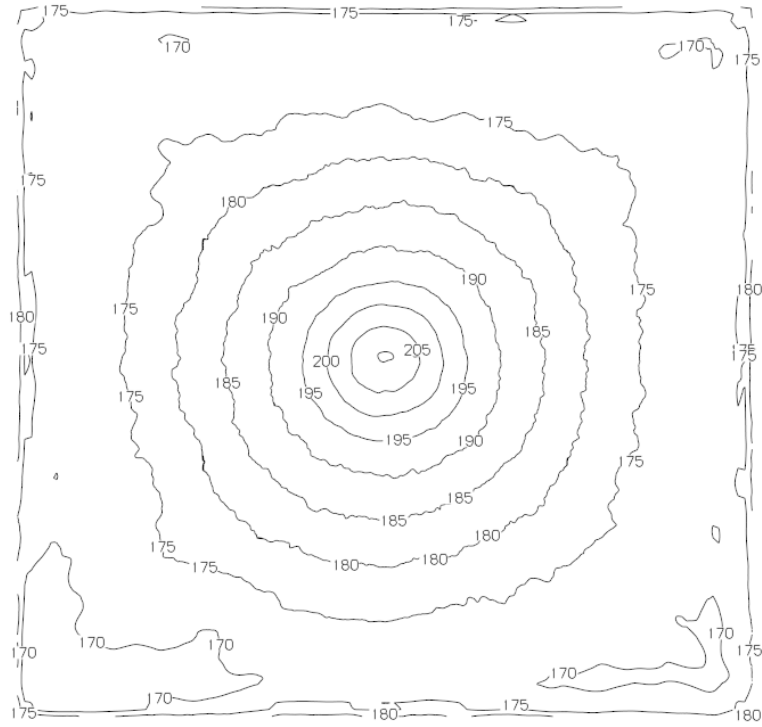


Figure 4-56 OASPL on the impingement plate:  $h/d=4.25$

#### 4.10.1 Two-Point Correlations

The environments experienced on the impingement plate were investigated in more depth for the  $h/d=4$  separation distance. The normalized, two-point spatial correlation of pressure was calculated on the surface using Equation (4-5) [24].

$$f(r,t) = \frac{\langle p(\vec{x} + \vec{e}r, t)p(\vec{x}, t) \rangle}{\langle p^2 \rangle} \quad (4-5)$$

In Equation (4-5),  $p$  is the pressure fluctuation and  $p^2$  is calculated at  $r$ . This results in the normalized two point correlation. Figure 4-57 shows the normalized two-point correlation on the plate several diameters from the jet. The correlation of the pressure on the plate shows a tight spatial correlation about the correlation point located at zero. The correlation rapidly falls off in all directions but slower in the azimuth direction than

the radial direction indicating the presence of elongated structures in the  $\theta$ -direction. The two-point space-time correlation on the plate is shown in Figure 4-58. This shows the convection velocities associated with the disturbances on the plate. Taking the slope of a line passing through zero and the contours of the correlation function gives a convection velocity ( $U_c$ ) of 200 m/sec which corresponds to a normalized convective velocity ( $U_c/U_{jet}$ ) of 0.47. This is a lower convective velocity than was observed in the jet shear layer (Figure 4-11). The SPL for the correlation point is shown in Figure 4-59. The L1 and L3 tones can be seen in Figure 4-59 but the L2 tone is not distinguishable from the overall noise level.

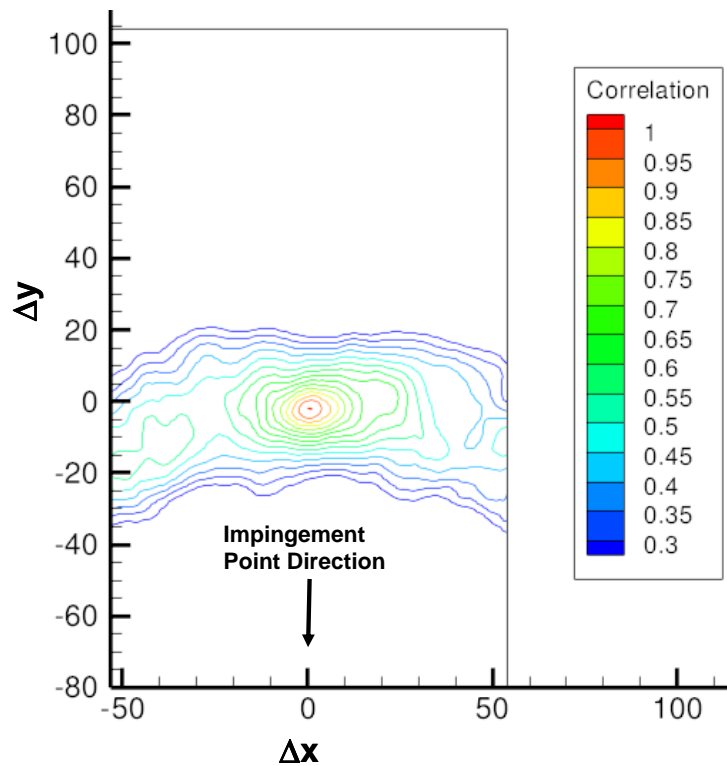


Figure 4-57 Normalized two-point space correlation on impingement plate at reference point 9.6 cm from the impingement point:  $h/d=4$



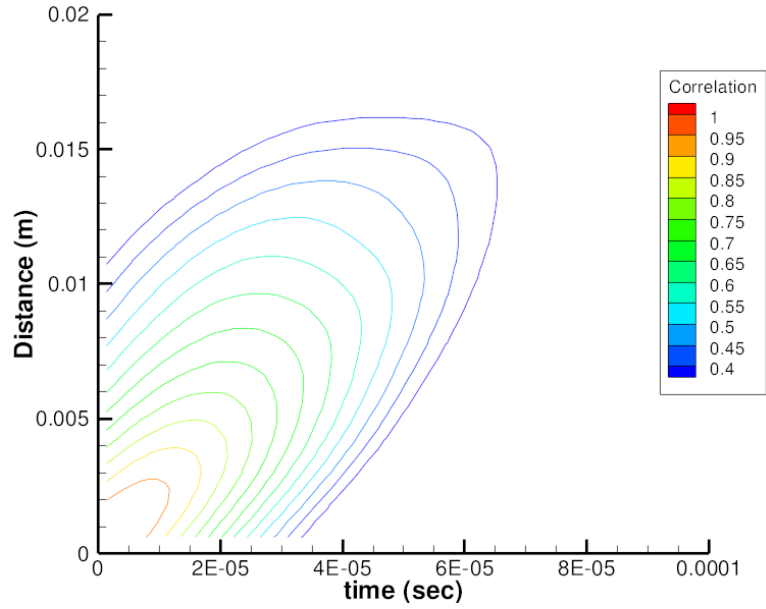


Figure 4-58 Normalized space-time correlation on impingement plate at reference point 9.6 cm from the impingement point:  $h/d=4$

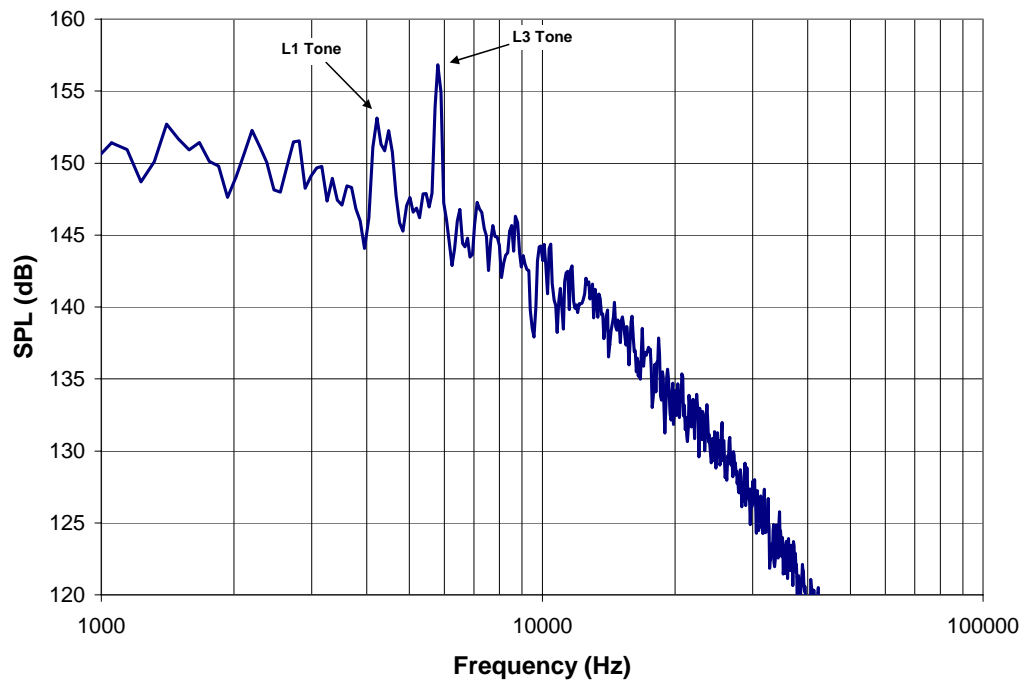


Figure 4-59 SPL on impingement plate at reference point 9.6 cm from the impingement point

### 4.10.2 Time-Averaged Pressure

Jet impingement produces a time varying pressure field on the plate. This field can be decomposed into mean and fluctuating components. The mean pressure distribution on the plate around the impingement point for each of the three separation distances is shown Figure 4-60. The distribution is relatively unchanged for the separation distances analyzed. The modified nozzle does not affect the mean pressure distribution about the impingement point. The fluctuating pressure distribution is responsible for the OASPL on the plate surface. Although the OASPL on the impingement plate shows some variation with separation distance, they are not significant.

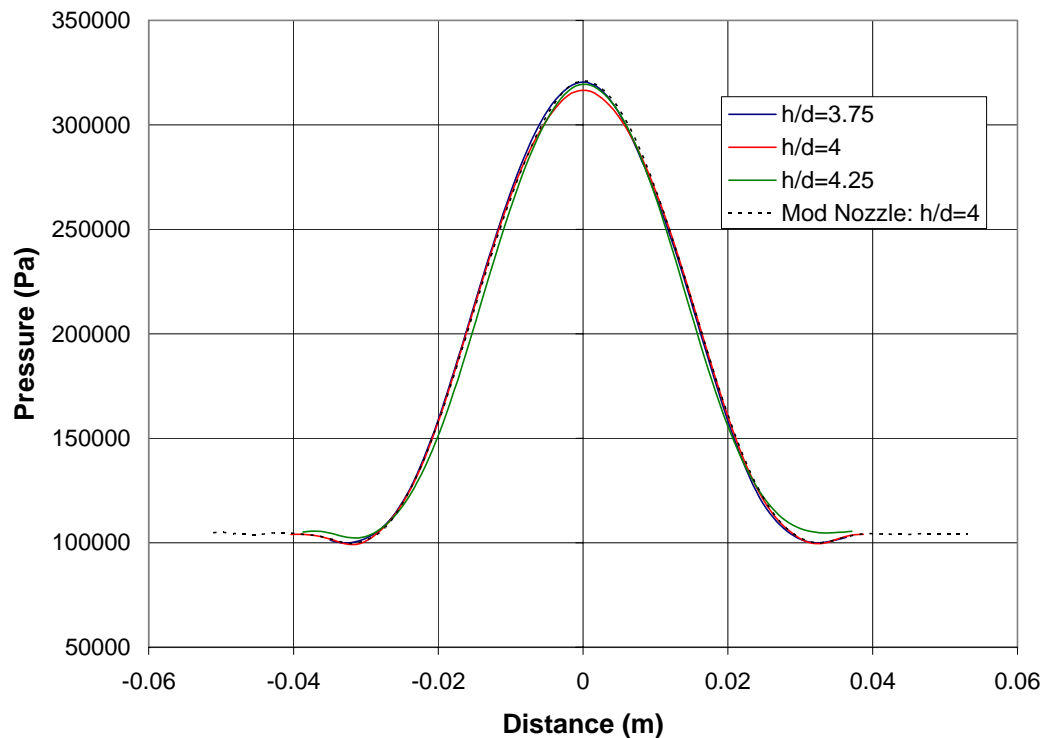


Figure 4-60 Time averaged pressure distribution at impingement point

## **CHAPTER 5**

### **CONCLUSIONS**

CFD analysis of a supersonic jet impingement on a flat plate was performed for three separation distances and the results compared to test data [10]. The CFD results showed good agreement with the test data. The CFD results also allowed an investigation to better understand the physics of supersonic jet impingement. The parameters that affect the impingement tones and the jet behavior were identified.

#### **5.1 Effects of Nozzle and Plate Separation Distance**

The nozzle exit to plate spacing is an important parameter in the behavior and resulting acoustic environment of the jet. The first effect is the decrease in the frequency of each tone. This observation has been made in a number of tests [4,5,8,10,12,16]. The instabilities that create the tones have their origins in the acoustic interactions between the impingement zone and the nozzle exit. As the distance between the plate and the nozzle exit increases, the acoustic waves take a longer time to propagate from the impingement point to the nozzle exit. It also takes longer for the disturbances to travel from the nozzle exit to impingement point. The increased distance reduces the frequency of the feedback and therefore reduces the tone frequency. This decrease in the frequency was observed both in the test data and in the CFD results.

The second effect of separation distance is the change in magnitudes of the impingement tones with separation distance. The dominant impingement tone changes as the separation distance increases. At the lowest separation distance,  $h/d=3.75$ , all the

tones show similar magnitudes and are well defined. At the intermediate separation distance,  $h/d=4$ , the L2 tone magnitude is greatly reduced and the tone has a broader character. The L1 and L2 tones magnitudes are higher with the L1 tone being dominant. At the last separation distance investigated,  $h/d=4.25$ , the L1 and L2 tones are diminished in the test data but the CFD predicts a significant L1 tone. However, the relative magnitude is diminished with regard to the  $h/d=4$  separation case. Both the test and CFD predict the L3 tone having the largest magnitude. The CFD results successfully captured this observed trend.

Another effect of increasing separation distance is the change in the structure of the jet. Separation distance changes the shock cell locations of the jet with the locations shifting downstream as the separation distance increases. The shift in the cell locations is slight near the nozzle exit and grows in magnitude farther downstream with the greatest shift occurring for the cell just upstream of the impingement plate. This shift will continue until the free jet cell locations are reached at a sufficiently large separation distance. This affects the velocity and pressure along the jet axis.

## **5.2 Effects of Nozzle Geometry**

CFD simulations for the  $h/d=4$  separation distance were performed with two different nozzles. The first nozzle geometry was based on the test nozzle geometry which has a gradual area change upstream of the throat. The second nozzle incorporated a much more rapid change in area upstream of the throat but still maintained the same diverging section and area ratio. The results showed that OASPL and directivity was not changed with the modified nozzle. The only changes were the magnitudes of the

impingement tones. This is most likely due to the change in the initial shear layer between the two nozzle geometries. Any change in the shear layer characteristics affects the receptivity of the shear layer. The shear layer receptivity affects which jet mode is dominant which in turn affects the impingement tones since there is a feedback mechanism between the frequency of the shear layer disturbances and the impingement zone. A change in shear layer receptivity may increase the magnitude of one impingement tone relative to others. This was observed in the CFD results with the L2 and L3 tones increasing in magnitudes while the L1 tone decreased in magnitude relative to the test nozzle geometry. The joint time-frequency analysis also showed that the L3 tone is much more stable in time for the modified nozzle than for the test nozzle geometry but the modified nozzle also shows competition between the L1 and L2 tones over time.

### **5.3 Feedback Mechanism Physics**

The feedback mechanism between the nozzle exit and the impingement zone was observed in the CFD results. The acoustic waves from the impingement zone affected both the shear layer and the jet core flow. The motion of the jet near the nozzle exit is affected by the motion of the jet core while downstream of the nozzle exit and closer to the plate, the jet motion is a function of the distribution of vortical disturbances in the shear layer. A helical distribution of vortices in the shear layer gives the jet a helical motion at the impingement plate while a symmetric distribution gives the jet a symmetric motion at the impingement plate.

Acoustic waves were observed to propagate into the jet core and perturb the conical compression wave structure at the nozzle exit. When an acoustic wave hits the compression cone, it reflects tangential to the surface with any normal reflections being extremely weak and incoherent. The tangential reflection results in a deformation in the compression cone surface. This perturbation is transmitted downstream through the interior of the jet and inducing a motion in the jet core. Symmetric acoustic waves results in the compression cone and the jet core oscillating in the axial direction. Helical acoustic waves results in the compression cone and the jet having a helical motion.

The acoustic waves from the impingement zone create disturbances in the shear layer at the nozzle lip. Subsequent acoustic waves create disturbances but also interact with the disturbances in the shear layer appearing to strengthen them. The disturbances are vortices that travel downstream in the shear layer to the impingement zone. The vortical nature of these disturbances was also observed in the test data [10]. The CFD calculated convective velocities of these vortices matched within 4% of what was measured in the tests. The role of these disturbances in the jet mode was also observed. The vortices were not symmetric and would perturb the jet as they travel downstream. The helical shape of these disturbances induced a flapping mode in the jet near the impingement point. This was most prominent for the  $h/d=4.25$  separation case since the jet was longer and the disturbances could travel farther.

Disturbances introduced into the shear layer at the nozzle lip through the feedback mechanism have different frequencies. The receptivity and properties of the shear layer are such that some frequency tones are enhanced while others are diminished. The CFD calculations show that some tones have higher magnitude in the jet shear layer compared

to those at the jet centerline and outside the shear layer. The L3 tone consistently showed higher magnitudes in the shear layer than in the jet and the surrounding fluid. This tone is apparently at a frequency at which the disturbance rapidly grows in the shear layer for all three impingement cases. The CFD calculation shows that the high frequency harmonics present in the shear layer and the jet quickly diminish between the jet and near field monitor point.

#### **5.4 Impingement Plate Environments**

The CFD also shows how the shear layer vortices propagate into the wall jet and are responsible for noise generation in that region. Two-point space correlations on the surface of the plate show a strong correlation in the azimuth direction which is consistent with the observed vortex propagation in the wall jet. Two-point space-time correlations show the convective velocity of the vortices is slower in the wall jet than they are in the shear layer with the CFD calculated a normalized convective velocity of 0.54 in the jet shear layer and 0.47 in wall jet at the measurement location 9.6 cm from the jet axis. Overall sound pressure levels on the impingement plate show similar magnitudes for all three impingement distances. This uniformity is also seen in the negligible variation of the time averaged pressure at the impingement point among the cases analyzed.

#### **5.5 Recommendations for Further Study**

The results of this study showed that hybrid RANS/LES CFD could be used to accurately capture and understand the physics of an impinging supersonic jet. The results also revealed some areas for further study in this subject.

Given the important role in shear layer receptivity on the feedback mechanism and the jet modes, a detailed analysis of shear layer receptivity should be performed. Given that the shear layer receptivity is dependent on its initial shape and characteristics, a more extensive study of nozzle geometry and upstream flow conditions would be valuable since this would provide a passive way to control or eliminate undesirable frequencies. This study would probably require a higher fidelity analysis than was performed here to capture the data required to perform a detailed study of the interaction of frequencies. Higher order methods would be beneficial for study of this problem given the size of the study and the temporal and spatial resolution requirements of the CFD simulations.



## REFERENCES

1. Lamont, P. J. and Hunt, B. L., "The impingement of underexpanded, axisymmetric jets on perpendicular and inclined flat plates", *Journal of Fluid Mechanics*, Vol. 100, Pt. 3, pp. 471-511, 1980.
2. Ho, C. and Nosseir, N. S., "Dynamics of an impinging jet. Part 1. The feedback Phenomenon", *Journal of Fluid Mechanics*, Vol. 105, pp. 119-142, 1981.
3. Nosseir, N.S. and Ho, C., "Dynamics of an impinging jet. Part 2. The noise generation", *Journal of Fluid Mechanics*, Vol. 116, pp. 379-391, 1982.
4. Krothapalli, A., "Discrete Tones Generated by an Impinging Underexpanded Rectangular Jet", *AIAA Journal*, Vol. 23, No. 12, pp. 1910-1915, 1985.
5. Powel, A., "The sound-producing oscillations of round underexpanded jets impinging on normal plates", *Journal of the Acoustical Society of America*, Vol. 83, No. 2, pp. 515-533, 1988.
6. Norum, T.D., "Supersonic Rectangular Jet Impingement Noise Experiments", AIAA Paper 89-1138, AIAA 12<sup>th</sup> Aeroacoustics Conference, San Antonio, TX., 1989.
7. Tam, C.K.W and Ahuja, K.K., "Theoretical model of discrete tone generation by impinging jets", *Journal of Fluid Mechanics*, Vol. 214, pp. 67-87, 1990.
8. Henderson, B. and Powell, A., "Experiments concerning tones produced by and axisymmetric choked jet impinging on flat plates", *Journal of Sound and Vibration*, Vol. 168, Pt. 2, pp. 307-326, 1993.
9. Kuo, C. and Dowling, A. P., "Oscillations of a moderately underexpanded choked jet impinging upon a flat plate", *Journal of Fluid Mechanics*, Vol. 315, pp. 267-291, 1996.
10. Krothapalli, A., Rajkuperan, E., Alvi, F., and Lourenco, L., "Flow field and noise characteristics of a supersonic impinging jet", *Journal of Fluid Mechanics*, Vol. 392, pp. 155-181, 1999.
11. Alvi, F.S. and Iyer, K.G., "Mean and Unsteady Flow field Properties of Supersonic Jets with Lift Plates", AIAA Paper 99-1829, 5<sup>th</sup> AIAA/CEAS Aeroacoustics Conference, Bellevue, WA, 1999.
12. Henderson, B., "The connection between sound production and jet structure of the supersonic impinging jet", *Journal of the Acoustical Society of America*, Vol. 111, No. 2, pp. 735-746, 2001.

13. Henderson, B., Bridges, J., and Wernet, M., "An Investigation of the Flow Structure of Tone Producing Supersonic Impinging Jets", AIAA Paper 2002-2529, 8<sup>th</sup> AIAA/CEAS Aeroacoustic Conference, Breckenridge, CO., 2002.
14. Henderson, B., Bridges, J., and Wernet, M., "An experimental study of the oscillatory flow structure of tone-producing supersonic impinging jets", *Journal of Fluid Mechanics*, Vol. 542, pp. 115-137, 2005.
15. Launder, B.E., Reece, G.J., and Rodi, W., "Progress in the Development of a Reynolds-Stress Turbulence Closure," *Journal of Fluid Mechanics*, Vol. 68, Pt. 3, pp. 537-566, 1975.
16. Lee, K. and Hong, S., "Supersonic Jet Impingement Navier-Stokes Computations for Vertical Launching System Design Applications", *Journal of Spacecraft and Rockets*, Vol. 41, No. 5, pp. 735-744, 2004.
17. Dauplain, A., Cuenot, B., and Gicquel, L.Y.M., "Large Eddy Simulation of Stable Supersonic Jet Impinging on Flat Plate", *AIAA Journal*, Vol. 48, No. 10, pp. 2325-2338, 2010.
18. Tsuboi, N., Hayashi, A.K., Fujiwara, T., Arashi, K., Kodama, M., "Numerical Simulation of a Supersonic Jet Impingement on a Ground", SAE 912014, 1991.
19. Yaga, M., Ueda, K., Ohshiro, T., Senaha, I., Oyakawa, K., "Experimental and Three-Dimensional Numerical Study on Under-Expanded Impinging Jets", *Journal of Thermal Science*, Vol. 9, No. 4, 2000.
20. Kim, S.I., Park, S.O., "Oscillatory behavior of supersonic impinging jet flows", *Shock Waves* Vol. 14, No.4 pp. 259-272, Springer-Verlag, 2005.
21. Hong, S.K. and Jeon, H.J., "Computational Study of Supersonic Jet Impingement on Flat and Complex Surfaces", AIAA-94-2326, Colorado, Springs, CO, 1994.
22. Hu, P. and Dittakavi, N., "Modeling and Simulation of a Jet Impingement on Aircraft Structure", AIAA 2011-2141, Denver, CO, 2011.
23. Lee, K., Hong, S.K., Park, S., "Supersonic Jet Impingement Navier-Stokes Computations for Vertical Launch System Design Applications", *Journal of Spacecraft and Rockets*, Vol. 41, No. 5, 2004.
24. Pope, S.B., *Turbulent Flows*, Cambridge University Press, New York, 2003.
25. Warsi, Z.U.A., "Fluid Dynamics: Theoretical and Computational Approaches", CRC Press Inc., Boca Raton, FL, 2000.

26. Wilcox, D.C., "Reassessment of the Scale-Determining Equation for Advanced Turbulence Models", *AIAA Journal*, Vol. 26, No. 11, pp. 1299-1310, 1986.
27. Nicols, R.H., "Turbulence Models and Their Applications to Complex Flows", University of Alabama at Birmingham, 2006.
28. Menter, F.R. and Rumsey, C.L., "Assessment of Two-Equation Turbulence Models for Transonic Flows", AIAA-94-2342, 1994.
29. Suzen, Y.B., Hoffmann, K.A., "Investigation of Supersonic Jet Exhaust Flow by One- and Two-Equation Turbulence Models," AIAA-98-032, January 1998.
30. Nichols, R.H., Tramel, R.W., and Buning, P.G., "Solver and Turbulence Model Upgrades to OVERFLOW 2 for Unsteady and High-Speed Applications", AIAA-2006-2824, San Francisco, CA, 2006.
31. Nicols, R.H., Tramel, R.W., and Buning, P.G., "Evaluation of Two High Order WENO Schemes," AIAA-2007-3920, June 2007.
32. Nicols, R.H., "A Comparison of Hybrid RANS/LES Turbulence Models on a Circular Cylinder at High Reynolds Number," AIAA-2005-498, Jan. 2005.
33. Nicols, R.H., "A Comparison of Hybrid RANS/LES Turbulence Models for a Generic Weapons Bay With and Without a Spoiler," AIAA-2008-6229, Aug. 2008.
34. Tramel, R., Rock, S., Ellis, J., and Sharpes, D., "Comparison of Large Cavity Aeroacoustic Computations with Flight Test Results," AIAA-2005-2800, May 2005.
35. Lackey, S., *Weapons bay acoustic suppression using a novel rod in Crossflow Configuration*, The University of Alabama in Huntsville, 2010.
36. Nichols, R.H., Buning, P.G., "Users Manual for Overflow", University of Alabama and NASA Langley Research Center, 2008
37. Lomax, H., Pulliam, T.H., and Zingg, D.W., *Fundamentals of Computational Fluid Dynamics*, Springer-Verlag, New York, 2003.
38. Ahuja, K.K., "The Role of the Feedback Phenomena in Many Aeroacoustics Problems of Current Interest", AIAA 2001-0077, Reno, NV. 2001.
39. Tam, C. K. W., "Excitation of instability waves in a two-dimensional shear layer by sound", *Journal of Fluid Mechanics*, Vol. 89, part 2, pp. 357-371, 1978.
40. Sherman, F.S., *Viscous Flow*, McGraw-Hill, Inc., New York, 1990.

41. Lesieur, M., Metais, O., and Comte, P., *Large-Eddy Simulation of Turbulence*, Cambridge University Press, New York, 2005.
42. Resenthal, P. Xion, Y., Nagib, H.M., “The Preferred Mode in an Axisymmetric Jet With and Without Feedback”, AIAA 91-0315, January, 1991.
43. Liu, J., Kailasnath, K., Ramamurti, R., Munday, D., Ephraim, G., Lohner, R., “Large-Eddy Simulation of a Supersonic Jet and Its Near-Field Acoustic Properties”, *AIAA Journal*, Vol. 47, No. 8, pp.1849-1864, August 2009

## APPENDIX A

# Supersonic Jet Impingement on a Flat Plate

Michael R. Brown<sup>1</sup>

*Kratos/Digital Fusion Solutions, Inc., Huntsville, AL.*

Abdelkader Frendi<sup>2</sup>

*University of Alabama in Huntsville, Huntsville, AL*

**Numerical simulations of a supersonic air jet impinging on a flat plate are carried out using the Detached Eddy Simulation turbulence model. This study models an ideally expanded Mach 1.5 jet impinging normally on a large flat plate. The jet issues from a converging-diverging nozzle imbedded in a lift plate. The effects of separation distance between the nozzle exit and the impingement plate are investigated. It is found that as the separation distance increases, the dominant frequencies in the spectrum decrease. In addition, the relative strength of the various frequencies to each other changes with changing distance, indicating the changing modes of the jet. Our CFD results indicate a strong interaction between the acoustic waves emanating from the impingement plate and the jet plume. This**

---

<sup>1</sup> Principal Engineer, Kratos/Digital Fusion Solutions, Inc., Aerosciences and Engineering Analysis Branch, Huntsville, AL. Ricky.Brown@kratosdefense.com

<sup>2</sup> Professor, Mechanical and Aerospace Engineering, UAHuntsville, and AIAA Associate Fellow.

feedback mechanism is responsible for destabilizing the jet shear layer leading to the jet changing modes. The computed near field spectra and convection velocities of the jet vortical structures are in good agreement with experimental measurements.

## I. Nomenclature

$\rho$	=	density
$\bar{\rho}$	=	time average density
$\tilde{u}_i$	=	mass average velocity component with $i = 1,2,3$
$u_i''$	=	fluctuating turbulent velocity component with $i = 1,2,3$
$p$	=	pressure
$\bar{p}$	=	average pressure
$x_i$	=	spatial direction with $i = 1,2,3$
$t$	=	time
$\tilde{h}$	=	mass averaged specific enthalpy
$\tilde{H}$	=	mass averaged total enthalpy
$h''$	=	fluctuating turbulent specific enthalpy
$\delta_{ij}$	=	Kronecker delta
$\mu$	=	molecular viscosity
$\lambda$	=	thermal conductivity
$\mu_t$	=	turbulent eddy viscosity

$\nu_t$	=	turbulent kinematic eddy viscosity
$\Omega$	=	vorticity vector magnitude
$k$	=	turbulent kinetic energy
$\varepsilon$	=	turbulent dissipation
$\sigma_k, \sigma_\omega, \sigma_{\omega 2}, \beta^*, \gamma$	=	turbulence model constants
$\alpha_1, \alpha_2, \alpha_3, a_1$	=	turbulence model constants
$F_1, F_2$	=	turbulence model functions
$C_{DES}, C_{DES}^{k-\varepsilon}, C_{DES}^{k-\omega}$	=	turbulence model constant
$C_\mu$	=	turbulence model constant
$C_p$	=	specific heat at constant pressure
Pr	=	Prandtl number
$\Delta$	=	grid spacing
$L_t$	=	turbulence length scale
$L_g$	=	maximum grid length
$y$	=	normal distance to the nearest wall
$\theta$	=	generic function
$f$	=	generic function
$R$	=	ideal gas constant
$M_t$	=	turbulent Mach number
$T$	=	temperature
$\chi$	=	ratio of specific heats

## II. Introduction

Over the last few decades the time to design and field new military aircraft has greatly increased with a corresponding increase in cost. As a consequence, next generation military aircraft designs are incorporating design features to simultaneously meet the mission requirements of multiple branches of the military. This includes the incorporation of vertical take off and landing (VTOL) capabilities to into aircraft designs. However, these aircraft have problems of their own. In particular, during landing these aircrafts experience lift loss as they approach the ground which can be dangerous to the aircraft and crew. In addition, during take-off and landing, the subsonic or supersonic jet exhaust plume impinges on the ground resulting in higher noise levels in the vicinity of the aircraft. All of these issues have led to an increase in basic and applied research to understand the various physical mechanisms and devise ways to improve the noise environments and the aircraft's performance and safety.

Lamont and Hunt<sup>1</sup> investigated the flow structure of underexpanded turbulent jets impinging on a flat plate at various degrees of inclination. Schlieren images showed some oscillation in the shock wave at the surface of the plate. The oscillations were determined to be caused by the large, flat nozzle base which served as a reflective surface for the acoustic waves resulting in standing waves in the flow field. Ho and Nosseir<sup>2</sup> performed testing with turbulent impinging jets with high subsonic exit Mach numbers. Although these tests were for subsonic jets, the feedback mechanisms identified are relevant to supersonic impinging jets. Test data showed that for high subsonic speeds ( $M > 0.7$ ) and nozzle exit to plate separation distances of less than 7.5 exit diameters, the measured pressure signal on the plate had a sine shape indicating resonance. Nosseir and



Ho<sup>3</sup> examined the noise radiated by the jets studied in their previous work.<sup>2</sup> Cross correlations of the pressure data showed that the primary source of noise was the plate for a jet in resonance. A zero time delay was observed indicating that the impinging coherent structures were axi-symmetric. A high frequency component was observed but it had a lower intensity compared to the plate source. When the jet was not in resonance, the high frequency component had a similar intensity as the plate source. Krothapalli<sup>4</sup> investigated jet impingement for underexpanded choked jets from a rectangular nozzle. Observations showed the presence of two discreet tones that were identified as an impingement tone and a higher frequency screech tone that is typically associated with underexpanded jets. Staging behavior of the impingement tone was observed that depended on the ratio of jet height above the plate to the nozzle exit diameter. Oscillations in the impinging jet were seen and varied with nozzle pressure ratio and height of the nozzle exit above the plate. Data showed a feedback mechanism where acoustic waves at the impingement point travelled upstream toward the nozzle exit and induced instabilities in the shear layer. Powell<sup>5</sup> investigated normal impingement of underexpanded, round sonic jets on various sizes of flat plates. Investigation of impingement tones on large plates looked at a normalized height to nozzle exit ratios between 0.75 and 7.0. Seven stages of impingement tones were indentified in this height range and the feedback mechanism was identified as the probable cause of the observed staging. Norum<sup>6</sup> investigated impingement of supersonic, rectangular jets on a flat plate and recorded staging behaviors for the primary impingement tones for nozzle height to diameter ratios between 3 and 10. A model of the feedback mechanism was developed that was highly dependent on the estimated average convection velocity in the subsonic

portion of the jet. Tam and Ahuja<sup>7</sup> suggested that the feedback loop for the impingement tones is not external to the jet as put forth by Nosseir and Ho.<sup>2,3</sup> Tam and Ahuja proposed that the waves travelling upstream from the plate to the nozzle exit were neutral waves having the same characteristics as Kelvin-Helmholtz instability waves. These waves propagate within the jet and close the feedback loop which produced the characteristic impingement tones. Henderson and Powell<sup>8</sup> performed tests for normal impingement of an axisymmetric choked jet on a large flat plate with nozzle height to exit diameter ratios between 0.5 and 10. Data analysis showed that these tones fell onto three parallel lines on a logarithmic plot and identified as L1, L2 and L3 tones (the L notation was used to designate large plate). The L1 tones were symmetrical while the L2 and L3 tones were helical. Kuo and Dowling<sup>9</sup> investigated the shock oscillations for a moderately underexpanded jet impinging on a flat plate. They developed a linear stability theory to predict shock oscillation frequency and damping rate for a given nozzle to plate distance, nozzle pressure ratio and shock stand-off distance. Their study found that the shock oscillations resulted in pressure and entropy fluctuations in the stagnation region of the plate. Krothapalli, et. al.<sup>10</sup> performed studies on the acoustics of perfectly expanded and underexpanded supersonic axisymmetric jet impinging on a flat plate. Tests were performed with a nozzle imbedded in a lift plate and such that the exit was flush with the bottom of the lift plate. Pressure data was taken on the lift plate to determine the downward force on the plate as a function of nozzle exit height above the plate. Near field acoustic data was taken ten throat diameters from the nozzle exit. Data was taken for height to nozzle throat diameter ratios of 3.75, 4 and 4.25. The nozzle

pressure ratio (NPR) for the perfectly expanded cases was 3.7 while the NPR of the underexpanded cases was 5. Results from the study showed that the lift loss increased as the separation distance between the nozzle exit and the ground plane decreased.

On the computational side of the research effort several computations have been carried-out to help understand the experimental observations. However, a large number of these computations used either the RANS approach, which leads to steady state results, or modeled the fluid as inviscid, which affects the jet shear layer. In recent years, with the increase in computational power, more and more unsteady highly resolved computations are being carried out. In particular, Dauplain, Cuenot and Gicquel<sup>11</sup> performed a numerical study of supersonic jet impingement on a flat plate using large eddy simulation (LES). They modeled a supersonic jet from a converging nozzle with an NPR of 4.03 impinging on a flat plate at a distance of 4.16 nozzle exit diameters. Comparisons were made between the CFD results and the experimental data of Henderson, Bridges and Wernet.<sup>12</sup> Computed mean and fluctuating quantities showed good agreement with the data. Since the jet was from an underexpanded converging nozzle only a weak impingement tone was produced with most of the acoustics exhibiting a broadband noise. Hu and Dittakavi<sup>13</sup> carried out an LES computation of a supersonic jet impingement on a flat plate using high order schemes. Their preliminary results were in good qualitative agreement with experimental data.

Based on the literature review, there still remain many unanswered questions regarding the flow physics of supersonic jet impingement on a flat plate. The present work attempts to follow the experimental study carried-out by Krothapalli et. al.<sup>10</sup>. Using a highly

resolved Detached Eddy Simulation, unsteady computations of a supersonic impinging jet are performed.

### III. Mathematical Model and Method of Solution

Decomposing every flow variable,  $f$ , as  $f = \tilde{f} + f''$  where  $\tilde{f} = \frac{\overline{\rho f}}{\rho}$  is a Favre average (also known as mass average) and  $f''$  is the turbulent fluctuation. Introducing this decomposition into the conservation equations leads to the well-known Favre averaged equations given by<sup>14</sup>

$$\frac{\partial \bar{p}}{\partial t} + \frac{\partial}{\partial x_j} (\bar{\rho} \tilde{u}_j) = 0 \quad (1)$$

$$\frac{\partial}{\partial t} (\bar{\rho} \tilde{u}_i) + \frac{\partial}{\partial x_j} (\bar{\rho} \tilde{u}_j \tilde{u}_i) = - \frac{\partial \bar{p}}{\partial x_i} + \frac{\partial}{\partial x_j} \left[ (\mu + \mu_t) \left( \frac{\partial \tilde{u}_i}{\partial x_j} + \frac{\partial \tilde{u}_j}{\partial x_i} - \frac{2}{3} \mu \frac{\partial \tilde{u}_k}{\partial x_k} \cdot \delta_{ij} \right) \right] \quad (2)$$

$$\begin{aligned} \frac{\partial}{\partial t} (\bar{\rho} \tilde{H} - \bar{p}) + \frac{\partial}{\partial x_j} (\bar{\rho} \tilde{u}_j \tilde{H}) &= \frac{\partial}{\partial x_j} \left[ \left( \frac{\mu}{\text{Pr}_L} + \frac{\mu_t}{\text{Pr}_t} \right) \frac{\partial \tilde{h}}{\partial x_j} \right] + \\ \frac{\partial}{\partial x_j} \left[ \tilde{u}_i (\mu + \mu_t) \left( \frac{\partial \tilde{u}_i}{\partial x_j} + \frac{\partial \tilde{u}_j}{\partial x_i} - \frac{2}{3} \mu \frac{\partial \tilde{u}_k}{\partial x_k} \cdot \delta_{ij} \right) \right] &+ \frac{\partial}{\partial x_j} \left[ \left( \mu + \frac{\mu_t}{\sigma_k} \right) \frac{\partial k}{\partial x_j} \right] \end{aligned} \quad (3)$$

Einstein's summation convention is used throughout this paper with  $\delta_{ij}$  being the Kronecker delta. In Eq. (3)  $\text{Pr} = \frac{C_p \mu}{\lambda}$  is the Prandtl number,  $\tilde{H} = \tilde{h} + \frac{1}{2} \overline{u_i u_i}$  the total

enthalpy with  $\tilde{h}$  being the specific enthalpy and  $k = \frac{1}{2} \overline{u_i'' u_i''}$  the turbulent kinetic energy.

The turbulent transport of heat is modeled as

$$-\overline{\rho u_j'' h''} = \frac{\mu_t}{Pr_t} \frac{\partial \tilde{h}}{\partial x_j} \quad (4)$$

Lastly, the molecular diffusion and turbulent transport of  $k$  are modeled as

$$\overline{u_i'' \tau_{ij}''} - \overline{\rho u_j'' \left( \frac{1}{2} u_i'' u_i'' \right)} = \left( \mu + \frac{\mu_t}{\sigma_k} \right) \frac{\partial k}{\partial x_j} \quad \text{where } \sigma_k = \text{constant} \quad (5)$$

In Eq. (2), the Boussinesq's hypothesis for relating Reynolds stresses to the mean rate of strain in form of

$$-\overline{\rho u_i'' u_j''} + \frac{2}{3} \rho k \cdot \delta_{ij} = \mu_t \left( \frac{\partial \tilde{u}_i}{\partial x_j} + \frac{\partial \tilde{u}_j}{\partial x_i} \right) - \frac{2}{3} \mu_t \frac{\partial \tilde{u}_k}{\partial x_k} \cdot \delta_{ij} \quad (6)$$

has been used. In the above equations,  $\mu_t$  is the turbulent eddy viscosity and  $\mu$  the molecular viscosity. For closure, Mentor shear stress transport (SST) model is used.<sup>15</sup> The model combines the strengths of two well known two equation models, namely k- $\epsilon$  and k- $\omega$ , the former being accurate away from wall boundaries and the later doing a much better job near walls. The new blended model is given below

$$\begin{aligned} \frac{\partial \rho k}{\partial t} + \frac{\partial \rho u_i k}{\partial x_i} = & -\overline{\rho u_i'' u_j''} \frac{\partial u_i}{\partial x_j} - \rho \omega \beta^* k [1 + \alpha_1 M_t^2 (1 - F_1)] + (1 - F_1) \overline{p'' d''} \\ & + \frac{\partial}{\partial x_i} \left[ (\mu + \sigma_k \mu_t) \frac{\partial k}{\partial x_j} \right] \end{aligned} \quad (7)$$

$$\begin{aligned} \frac{\partial \rho \omega}{\partial t} + \frac{\partial \rho u_i \omega}{\partial x_i} = & -\frac{\gamma}{\nu_t} \overline{\rho u_i'' u_j''} \frac{\partial u_i}{\partial x_j} - (1 - F_1) \frac{\overline{p'' d''}}{\nu_t} - \beta \rho \omega^2 \\ & + (1 - F_1) \beta^* \alpha_1 M_t^2 \rho \omega^2 + 2 \rho \sigma_{\omega 2} \frac{1}{\omega} (1 - F_1) \frac{\partial k}{\partial x_i} \frac{\partial \omega}{\partial x_i} + \frac{\partial}{\partial x_i} \left[ (\mu + \sigma_{\omega} \mu_t) \frac{\partial \omega}{\partial x_i} \right] \end{aligned} \quad (8)$$

where the pressure dilatation term is

$$\overline{p'' d''} = \alpha_2 \overline{\rho u_i'' u_j''} \frac{\partial \tilde{u}_i}{\partial x_j} M_t^2 + \alpha_3 \rho \varepsilon M_t^2 \quad (9)$$

with  $\alpha_1 = 1.0$ ,  $\alpha_2 = 0.4$  and  $\alpha_3 = 0.2$ . In Eqs. (7)-(9),  $M_t$  is given by

$$M_t = \sqrt{\frac{2k}{\chi RT}} \quad (10)$$

is the local turbulence Mach number.

In Eqs. (7) and (8),  $\sigma_k = 0.5$ , and  $F_1$  is a blending function given by

$$F_1 = \tanh \left( \left[ \min \left[ \max \left( \frac{\sqrt{k}}{C_{\mu} \omega y}, \frac{500 \nu}{y^2 \omega} \right), \frac{4 \rho \sigma_{\omega 2} k}{CD_{k\omega} y^2} \right] \right]^4 \right) \quad (11)$$

where  $y$  is the normal distance to the wall and  $CD_{k\omega}$  is the positive portion of

$$CD_{k\omega} = \max \left( 2 \sigma_{\omega 2} \frac{1}{\omega} \frac{\partial \rho k}{\partial x_i} \frac{\partial \rho \omega}{\partial x_i}, 10^{-20} \right) \quad (12)$$

$$\theta = F_1 \theta_1 + (1 - F_1) \theta_2 \quad (13)$$

The coefficients in Eq. (8) are computed using Eq. (13) to blend the coefficients corresponding to the  $k$ - $\omega$ ,  $\theta_1$ , with the coefficients from the  $k$ - $\varepsilon$  model,  $\theta_2$ .<sup>16</sup> The eddy viscosity is computed using

$$\nu_t = \frac{a_1 k}{\max(a_1 \omega, \Omega F_2)} \quad (14)$$

where  $a_1=0.31$ ,  $\Omega$  is the magnitude of the vorticity vector and  $F_2$  is calculated from

$$F_2 = \tanh \left[ \max \left( \frac{2\sqrt{k}}{C_\mu \omega y}, \frac{500\nu}{y^2 \omega} \right) \right] \quad (15)$$

The DES modifications to the SST model replaces the dissipation term in Eq. (7) with<sup>16</sup>

$$\varepsilon = \frac{\omega}{\beta^* k} = \frac{\varepsilon}{\min \left( 1.0, C_{DES} \frac{L_g}{L_t} \right)} \quad (16)$$

where  $L_g$  is the maximum grid length,  $L_t$  is the turbulence length scale and  $C_{DES}$  is the DES coefficient. Turbulence length scale and the  $C_{DES}$  are calculated using<sup>16</sup>

$$L_t = \frac{\sqrt{k}}{\beta^* \omega} = \frac{k^{3/2}}{\varepsilon} \quad (17)$$

$$C_{DES} = (1 - F_1) C_{DES}^{k-\varepsilon} + F_1 C_{DES}^{k-\omega} \quad (18)$$

In Eqs. (16) and (17),  $\beta^*=0.09$ ,  $C_{DES}^{k-\varepsilon}=0.6$ ,  $C_{DES}^{k-\omega}=0.78$  and  $F_1$  is the blending coefficient calculated using Eq.(10).<sup>16</sup> This model adjusts the eddy dissipation if the grid length scale is less than the turbulent length scale which reduces the eddy dissipation in these regions. Turbulent length scales not resolved on the computational grid are modeled using the RANS model which behaves like a subgrid model in LES.

The system of equations (1)-(3) together with (7) and (8) were solved using the OVERFLOW 2 CFD code<sup>17</sup>. This code was used successfully to analyze a variety of unsteady fluid dynamic phenomena<sup>18-20</sup>. The code uses structured overset grids, which allows computations in complex geometries.

#### **IV. Results and Discussions**

The geometry analyzed in this study is an ideally expanded, supersonic jet impinging on a flat plate. The geometric parameters in the CFD analysis match those presented in the test setup found in reference [10]. In the test, the supersonic jet was produced from a converging-diverging nozzle with an area ratio that gives ideally expanded flow at the nozzle exit (pressure at exit equal to atmospheric pressure). As shown on Fig. 1, the exit of the converging-diverging nozzle was flush mounted to a 25.4 cm diameter lift plate that was used to measure the downward force induced by air entrainment into the jet. A square impingement plate measuring 2.44 m x 2.44 m was placed at different distances below the nozzle exit depending on the test configuration being investigated. The computational model did not extend to the edges of the impingement plate so the plate covers the entire bottom of the computational domain. The converging-diverging nozzle is described as having a converging section based on a third order polynomial and a conic diverging section with a constant angle of three degrees. The nozzle throat and exit diameters are 2.54 cm and 2.75 cm, respectively, which gives an area ratio resulting in a perfectly expanded exit Mach number of 1.5 for a nozzle pressure ratio (NPR) of 3.7.



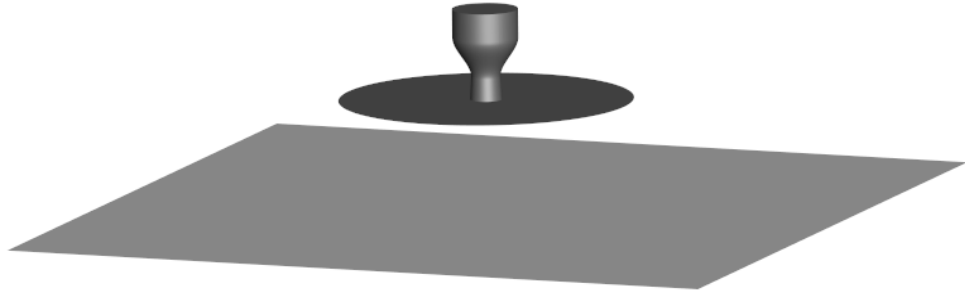


Fig. 1 Computational Model

The nozzle grids are wall fitted grids that wrap around the nozzle exit and onto the lift plate, Fig. 2. The spacing of the nozzle grids was fine enough at the wall to resolve the laminar boundary layer on the nozzle wall. Wall grid spacing varied from  $2 \times 10^{-6}$  m at the combustion chamber section,  $3.4 \times 10^{-7}$  at the nozzle throat, and  $1 \times 10^{-5}$  m at the nozzle exit. The flow in the nozzle was modeled as laminar based on the test observations.<sup>10</sup> A boundary layer grid was placed on the lift plate. Fine grids were placed on the impingement plate but no attempt was made to fully resolve the boundary layer and wall functions were used in this region. The spacing at the impingement plate is  $2 \times 10^{-4}$  m. The grid between the nozzle exit and the impingement plate is a uniform mesh with a spacing of  $6 \times 10^{-4}$  m. A uniform mesh was used to eliminate phase error associated with grid stretching. The grid spacing was calculated to minimize phase error in the solution by ensuring at least 80 points per wavelength<sup>20</sup> for the maximum, primary tone frequencies of 7000 Hz measured in the tests. The speed of sound for this

calculation was assumed to be the ambient value of 346 m/s. The size of the various grids used varied between 75 and 85 million grid points.

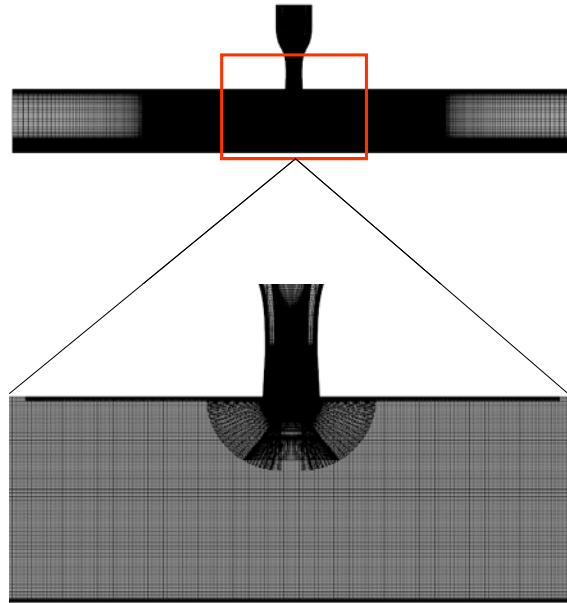


Fig. 2 Computational Grid

### A. Comparisons to Experimental Data

As mentioned in the previous section, the CFD computations presented in this paper are based on the experimental work of Krothapalli, et. al.<sup>10</sup>, therefore, extensive comparisons will be made to the data published in reference [10]. One such comparison is shown on Fig. 3 for the near field frequency spectra for a jet exit to impingement plate distance of  $3.75d$ , where  $d$  is the nozzle throat diameter. It is important to mention that the CFD near field location is slightly closer to the jet centerline than the microphone location. This was done due to the limited computational resources available and knowing that this will not affect the frequency content but the SPL levels will be slightly higher. Figure 3 shows the CFD results to be in good agreement with the measured

spectrum. In particular, both experimental and CFD results show the presence of three dominant modes labeled as L1, L2 and L3.<sup>8</sup> The CFD predicted frequencies of the various modes lag slightly the experimental ones and the sound pressure levels are higher as expected. The CFD results show a rapid roll-off in frequency past 20 kHz due to grid and time step resolution, which was also expected since both the grid and time step resolution were chosen to resolve frequencies in the 7 kHz range. The CFD results show a clear dominance of the L3 tone, which is symmetric, whereas the experimental data shows the three tones to be of nearly equal strength with the L3 tone being only slightly stronger.

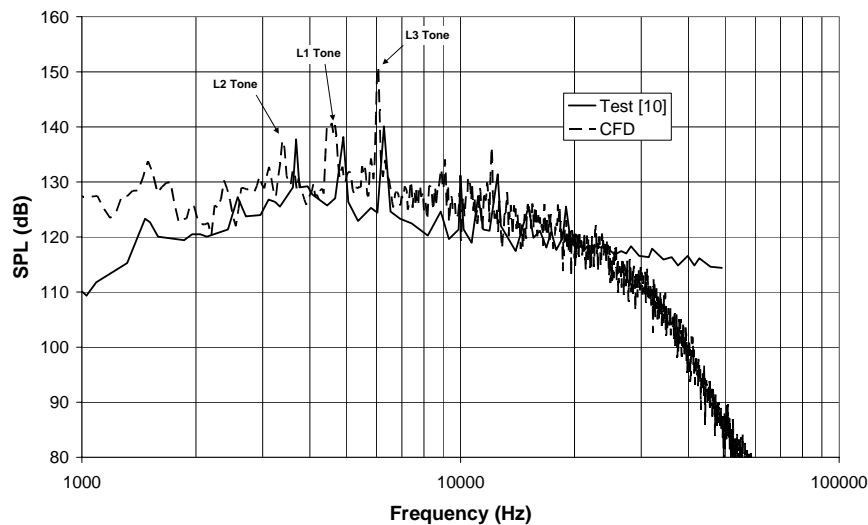


Fig. 3 Comparison of the near field frequency spectra for a nozzle exit to impingement plate distance of 3.75d.

Figure 4 shows the near field frequency spectra for a nozzle exit to impingement plate distance of 4.0d. The CFD results still show L3 to be the dominant tone, however, L1 is also strong and competing with L3. The experimental data shows L1 to be the strong tone with a competition from L3. The agreement between the CFD and

experimental data is good. Figure 5 shows the frequency spectra for a nozzle exit to impingement plate distance of 4.25d. Both the experimental data and the CFD results show the L3 tone to be dominant. A strong harmonic of the L3 tone is shown on the experimental spectrum while the CFD results show a weaker harmonic. The CFD results show the L1 and L2 tones to be stronger than they are in the experimental data. Overall the agreement between the CFD results and the experimental data is very good. As indicated earlier the sound pressure levels are slightly higher in the CFD results because the observation point is closer to the jet axis than in the experiments.

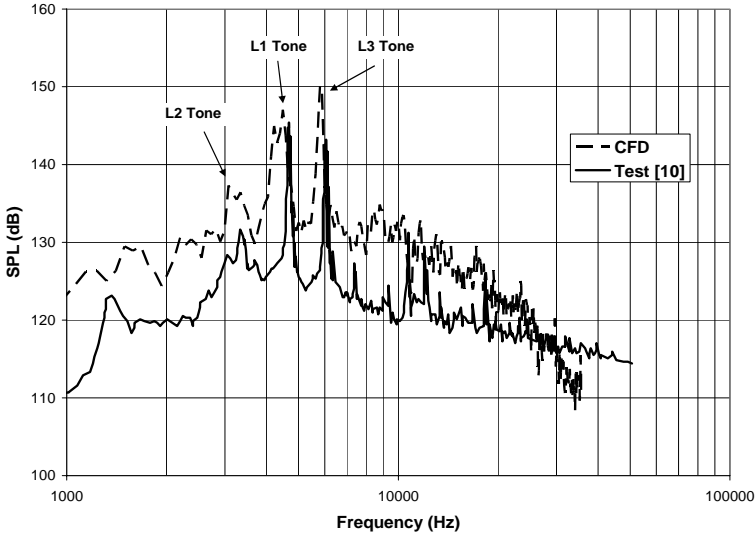


Fig. 4 Comparison of the near field frequency spectra for a nozzle exit to impingement plate distance of 4.0d.

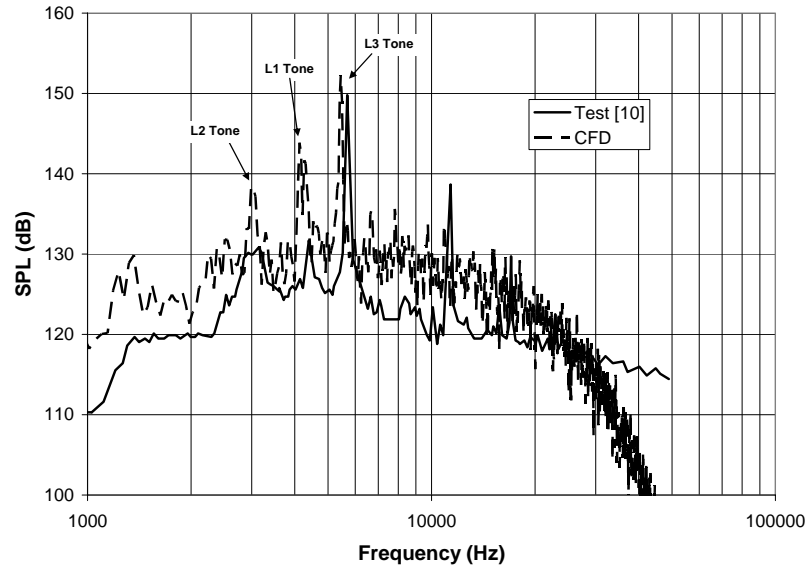


Fig. 5 Comparison of the near field frequency spectra for a nozzle exit to impingement plate distance of 4.25d.

Figure 6 shows the effect of the distance between the nozzle exit and the impingement plate on the frequency spectra measured experimentally. Note that only the spectrum for a distance of 3.75d has the correct SPL, that for 4.0d is offset by 20dB and the one for 4.25d is offset by 40dB. The figure shows that as the distance increases, all the tonal frequencies decrease. In particular, at a distance of 4.25d the L1 and L2 tones are much weaker than the L3 tone. Figure 7 shows the effect of separation distance between the nozzle exit and the impingement plate obtained from the CFD computations. In agreement with experimental data, the CFD results show the frequencies to shift lower with increasing distance from the nozzle exit. The CFD results also show that for a nozzle to impingement plate distance of 4.25d, the L1 and L2 tones are stronger than those measured. In addition, the predicted L3 tone is the strongest for all three distances. In

general the agreement with experimental data is good given the complex nonlinear nature of the various phenomena taking place.

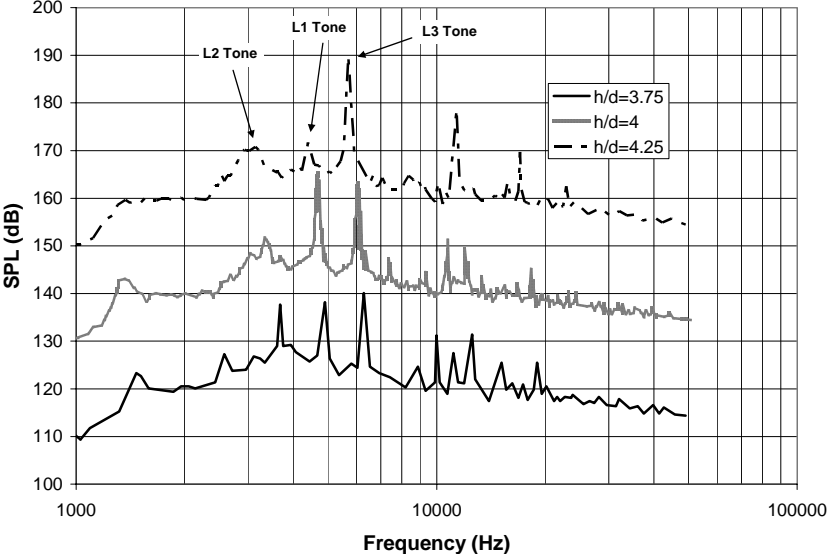


Fig. 6 Effect of separation distance between the nozzle exit and the impingement plate on the measured near field frequency spectra .

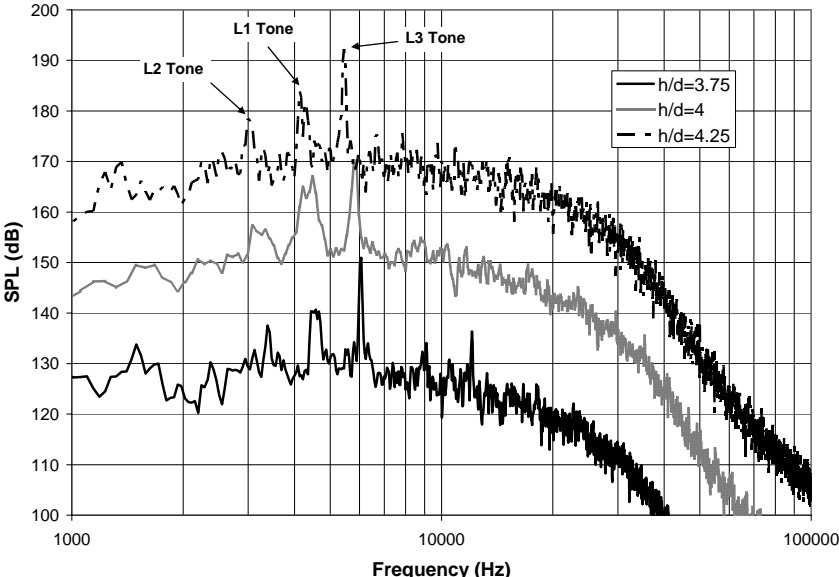


Fig. 7 Effect of separation distance between the nozzle exit and the impingement plate on the computed near field frequency spectra

In addition to the near field spectral comparisons shown above, a comparison of the convection velocity of the vortical structures in the jet shear layer is made. Figure 8 shows an instantaneous cross-section of the density gradient magnitude contours. In addition to prominent acoustic waves, the vortical structures are clearly identified on the figure. Similar to the experimental procedure, these vortical structures are identified then tracked through the shear layer and their convection velocities computed. Figure 9 shows a comparison for the convection velocities computed to those measured by Krothapalli, et. al.<sup>10</sup> for a nozzle exit to impingement plate distance of 4.0d. The convection velocities are normalized by the jet exit velocity of 427 m/s and plotted as a function of the distance between the nozzle exit and the impingement plate. Both the experimental data and computed results show the convection velocities to be scattered. The experimental mean is shown by the solid line and is 0.52 while the computed mean is shown by the dashed line and is 0.54. Once again, the CFD results are in excellent agreement with the measured data.

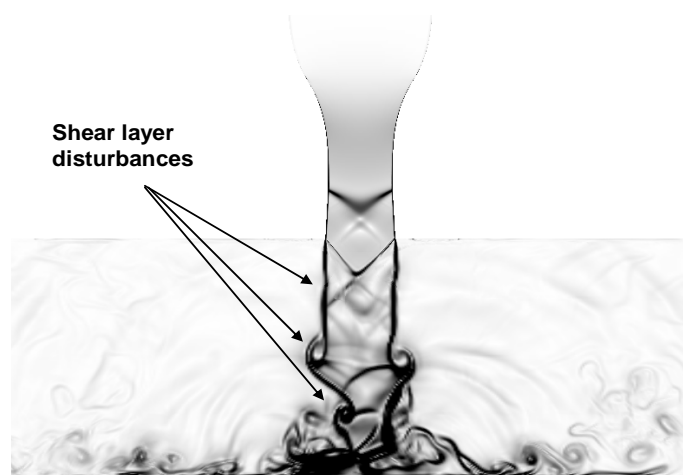


Fig. 8 Instantaneous density gradient magnitude contours for a nozzle exit to impingement plate distance of 4.0d.

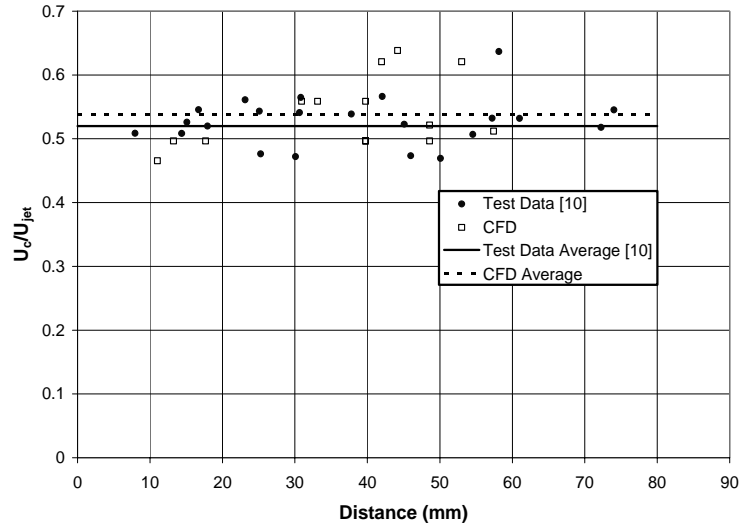


Fig. 9 Comparison of the measured and computed convection velocities of the jet shear layer vortical structures of a separation distance of 4.0d.

The frequency spectra presented in Figs. 3-5 show the computed results predict the L3 tone to be the dominant tone for all separation distances studied while the experimental results show competition between the L1 and L3 tones. Moreover, since the time history used for taking the statistics in the CFD results is much shorter than that used in the experiments, an in-depth time-frequency analysis is carried out. Figure 10 shows the computed pressure fluctuation time history for the separation distance case of 4.0d. The box shown on the figure highlights the windowing technique used to calculate the frequency spectra as a function of time. Each window contains 8192 data points representing a time sample of approximately 0.011 sec.



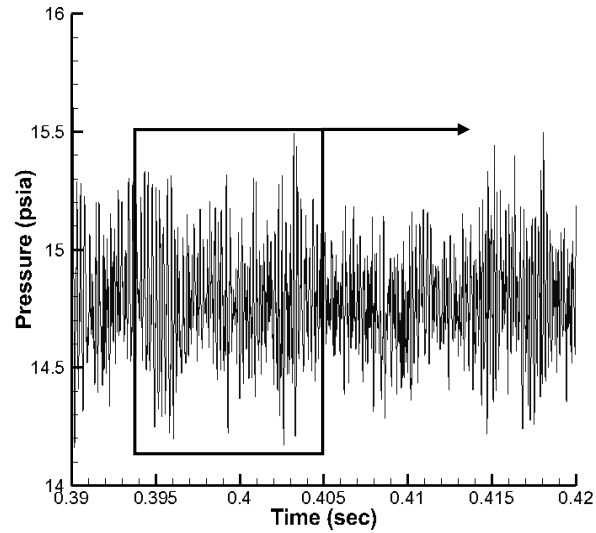


Fig. 10 Time history of the fluctuating pressure for a separation distance of 4.0d.

Figure 11 shows a three dimensional plot of the SPL as a function of time and frequency. The time axis is nondimensionalized by the sample window width shown by the box on Fig. 10. It is clear from the figure that there is a strong competition between the L1 and L3 tones and that at times the L1 tone is dominant and at other times the L3 tone is dominant. This result indicates the importance of the data sample size used in the analysis and the jet oscillations between two strong tones at this separation distance. This distance was also identified in the experiments of Krothapalli, et. al.<sup>10</sup> as a transitional and unstable distance for the jet.

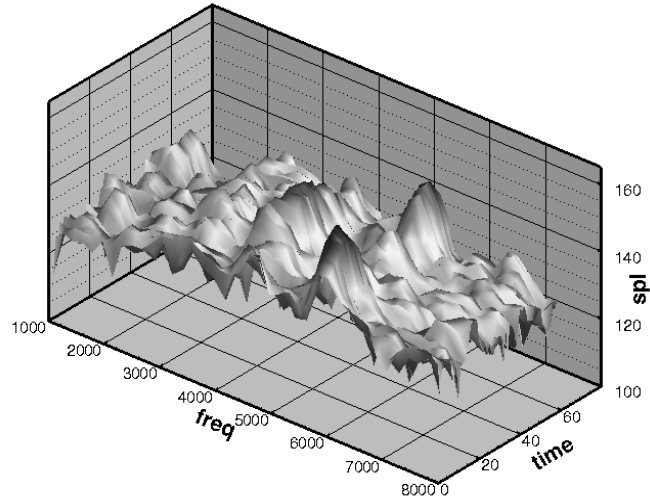


Fig. 11 Sound Pressure Level variation with time and frequency for a separation distance of 4.0d.

For a separation distance of 3.75d a similar but less pronounced competition between L1 and L3 is shown on Fig. 12. The figure shows L3 to be the dominant tone most of the time with L1 a strong second tone. All three tones are clearly identified on the figure. For a separation distance of 4.25d the L3 tone remains dominant the entire time with L1 and L2 weaker with a fluctuating SPL level, Fig. 13. The fact that L3 is dominant for this distance indicates the stability of the jet.

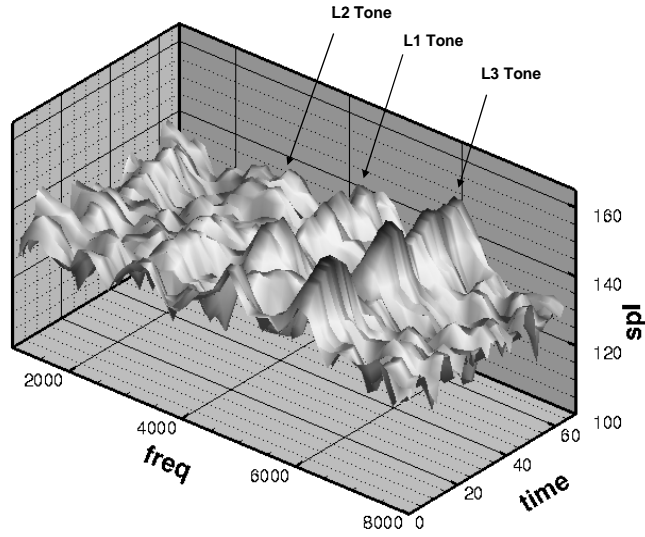


Fig. 12 Sound Pressure Level variation with time and frequency for a separation distance of 3.75d.

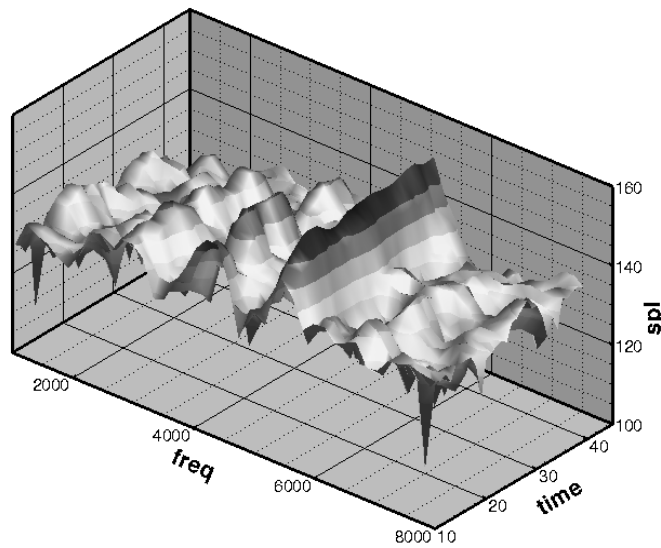


Fig. 13 Sound Pressure Level variation with time and frequency for a separation distance of 4.25d.

Figure 14 shows instantaneous Mach=0.5 isosurface colored by density at four different times and for a separation distance of 3.75d. The complex nature of the jet flow is highlighted by the figure where two jet modes can be simultaneously observed. The jet

shows a symmetric pulsing mode near the nozzle exit but a close examination shows that there is a helical component present as well. The pulsing motion corresponds to disturbances propagating in the jet. Figs. 14(a) shows an asymmetry in the jet near the nozzle exit. Figs. 14(b)-(d) show subsequent disturbances at the nozzle exit. The asymmetry is present at each time but the asymmetric part of the disturbance is slightly rotated about the jet axis at each time showing the presence of the helical mode of the jet. These disturbances can be seen as dark contours propagating into the wall jet on the plate resulting in very complex flow structures with long vortices clearly visible.

Figure 15 shows contours of the overall sound pressure levels in the jet plume for the three separation distances studied; 3.75d, 4.0d and 4.25d. A similar contour pattern is shown for all three distances, with the highest SPLs being in the stagnation region near the impingement surface. A standing wave pattern is also shown by the figure. In addition, high noise levels are seen in the wall jet area near the impingement surface.

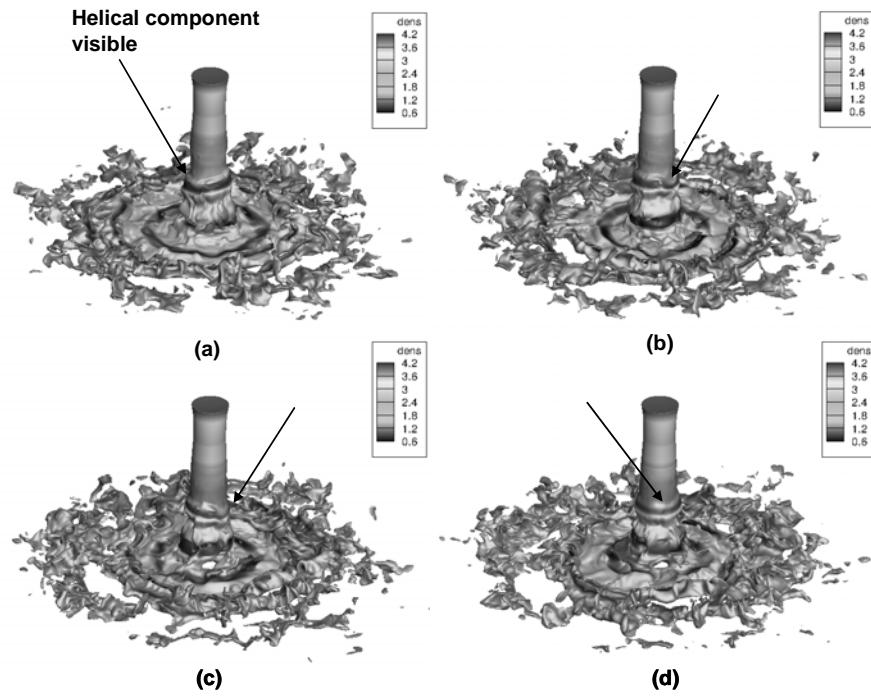


Fig. 14 Instantaneous Mach=0.5 isosurface colored by density for a separation distance of 3.75d and at four different times

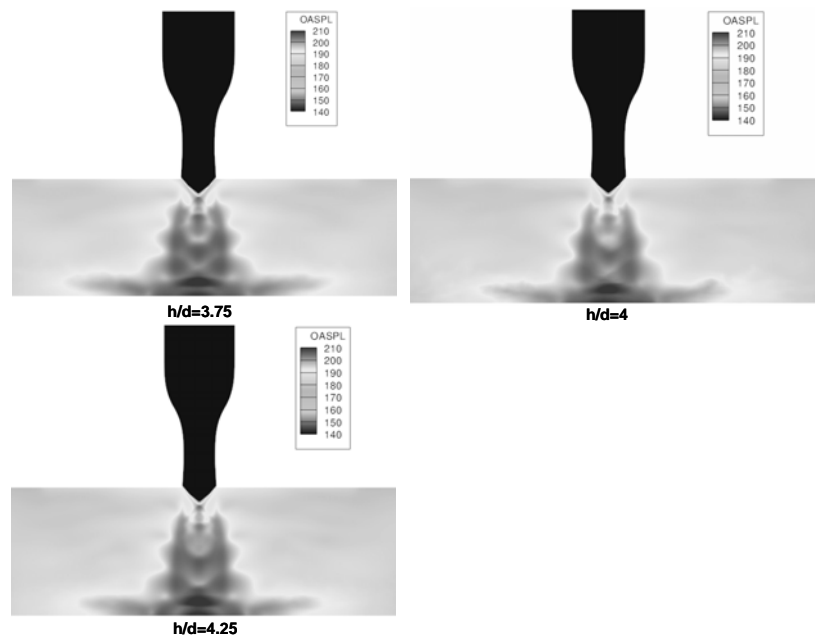


Fig. 15 Overall sound pressure levels in the jet plume for three separation distances.

Locations of high levels of turbulent kinetic energy are used to identify noise sources in the flow field. Figure 16 shows a cross-section of the time averaged turbulent kinetic energy for the three separation distances studied. All the figures show clearly that the region around the stagnation point on the impingement surface as well as the wall jet and the main jet shear layers are the major contributors to noise generation.

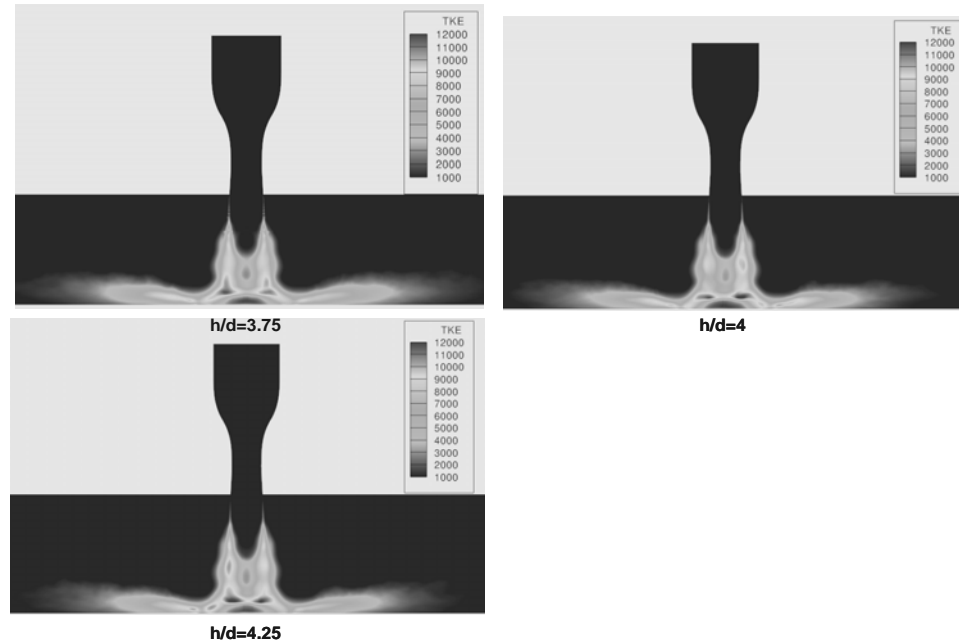


Fig. 16 Time averaged turbulent kinetic energy in a cross-section of the jet flow field.

Figure 17 shows a sequence of instantaneous density gradient magnitude contours along the jet cross-section for a separation distance of  $4.0d$ . Acoustic waves are clearly shown to propagate away from the impingement point on the horizontal surface. As they travel up the jet, they interact with the shear layer enhancing and/or creating disturbances that then propagate down the jet to the impingement plate. These disturbances grow into large vortices in the shear layer. The figure also shows vortical structures propagating along the

wall jet. In the main jet, the vortices on either side of the jet plume are offset indicating the dominance of a helical jet mode.

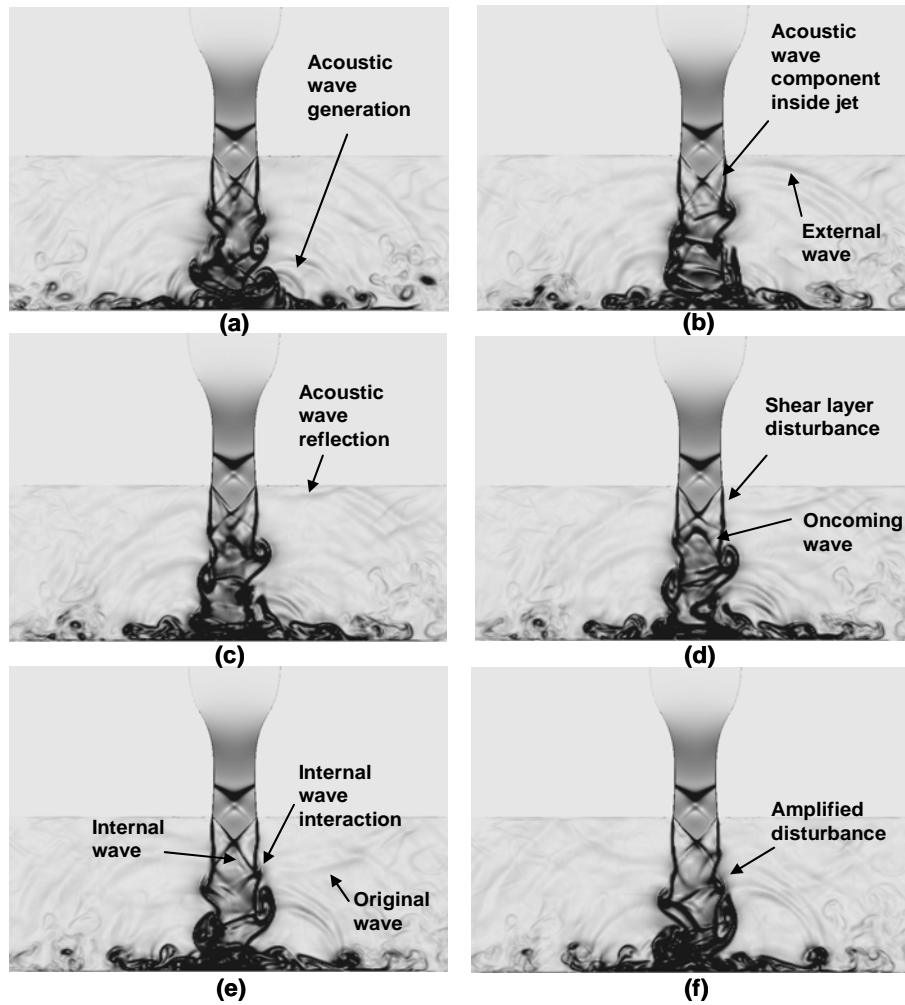


Fig. 17 Instantaneous density gradient magnitude contours in the jet flow field cross section for a separation distance of  $4.0d$ .

## V. Conclusions

Results from highly resolved DES computations of a supersonic impinging jet on a flat surface have been presented. Similar to the experimental work of Krothapalli, et. al.<sup>10</sup>, three separation distances between the nozzle exit and the impingement surface are studied,  $3.75d$ ,  $4.0d$  and  $4.25d$ . The computed frequency spectra for the three

separation distances were in good agreement with the measurement. In addition, the convection velocities of the vortical structures in the jet shear layer were also in very good agreement with those measured in tests. Our CFD results showed the importance of a time-frequency analysis that highlighted the competition between the various modes of the jet that was not evident from the experimental spectra. In addition, the CFD results successfully identified the sources of noise to be in the stagnation region on the impingement plate as well as the various shear layers. The complex interaction between the acoustic waves and the jet core and shear layers have been captured using density gradient contour plots.

## **VI. Acknowledgments**

The first author would like to acknowledge the support of Kratos/Digital Fusion Solutions, Inc. during the course of his PhD program. The first author would also like to acknowledge the support of his coworkers in the Aerosciences and Engineering Analysis branch whose support made this work possible.



## VII. References

- <sup>1</sup> Lamont, P. J. and Hunt, B. L., “The impingement of underexpanded, axisymmetric jets on perpendicular and inclined flat plates”, *Journal of Fluid Mechanics*, Vol. 100, Pt. 3, pp. 471-511, 1980.
- <sup>2</sup> Ho, C. and Nosseir, N. S., “Dynamics of an impinging jet. Part 1. The feedback Phenomenon”, *Journal of Fluid Mechanics*, Vol. 105, pp. 119-142, 1981.
- <sup>3</sup> Nosseir, N.S. and Ho, C., “Dynamics of an impinging jet. Part 2. The noise generation”, *Journal of Fluid Mechanics*, Vol. 116, pp. 379-391, 1982.
- <sup>4</sup> Krothapalli, A., “Discrete Tones Generated by an Impinging Underexpanded Rectangular Jet”, *AIAA Journal*, Vol. 23, No. 12, pp. 1910-1915, 1985.
- <sup>5</sup> Powel, A., “The sound-producing oscillations of round underexpanded jets impinging on normal plates”, *Journal of the Acoustical Society of America*, Vol. 83, No. 2, pp. 515-533, 1988.
- <sup>6</sup> Norum, T.D., “Supersonic Rectangular Jet Impingement Noise Experiments”, AIAA Paper 89-1138, AIAA 12<sup>th</sup> Aeroacoustics Conference, San Antonio, TX., 1989.
- <sup>7</sup> Tam, C.K.W and Ahuja, K.K., “Theoretical model of discrete tone generation by impinging jets”, *Journal of Fluid Mechanics*, Vol. 214, pp. 67-87, 1990.
- <sup>8</sup> Henderson, B. and Powell, A., “Experiments concerning tones produced by and axisymmetric choked jet impinging on flat plates”, *Journal of Sound and Vibration*, Vol. 168, Pt. 2, pp. 307-326, 1993.
- <sup>9</sup> Kuo, C. and Dowling, A. P., “Oscillations of a moderately underexpanded choked jet impinging upon a flat plate”, *Journal of Fluid Mechanics*, Vol. 315, pp. 267-291, 1996.

- <sup>10</sup>Krothapalli, A., Rajkuperan, E., Alvi, F., and Lourenco, L., “Flow field and noise characteristics of a supersonic impinging jet”, *Journal of Fluid Mechanics*, Vol. 392, pp. 155-181, 1999.
- <sup>11</sup>Dauplain, A., Cuenot, B., and Gicquel, L.Y.M., “Large Eddy Simulation of Stable Supersonic Jet Impinging on Flat Plate”, *AIAA Journal*, Vol. 48, No. 10, 2010, pp. 2325-2338.
- <sup>12</sup>Henderson, B., Bridges, J., and Wernet, M., “An Investigation of the Flow Structure of Tone Producing Supersonic Impinging Jets”, AIAA Paper 2002-2529, 8<sup>th</sup> AIAA/CEAS Aeroacoustic Conference, Breckenridge, CO., 2002.
- <sup>13</sup>Hu, P. and Dittakavi, N., “Modeling and Simulation of a Jet Impingement on Aircraft Structure”, AIAA 2011-2141, Denver, CO, 2011.
- <sup>14</sup> Warsi, Z.U.A., “Fluid Dynamics: Theoretical and Computational Approaches”, CRC Press Inc., Boca Raton, FL, 2000.
- <sup>15</sup>Menter, F.R. and Rumsey, C.L., “Assessment of Two-Equation Turbulence Models for Transonic Flows”, AIAA-94-2342, 1994.
- <sup>16</sup>Nichols, R.H., “Turbulence Models and Their Applications to Complex Flows”, University of Alabama at Birmingham, 2006.
- <sup>17</sup>Nichols, R.H., Tramel, R.W., and Buning, P.G., “Solver and Turbulence Model Upgrades to OVERLOW 2 for Unsteady and High-Speed Applications”, AIAA-2006-2824, San Francisco, CA, 2006.

- <sup>18</sup>Nicols, R.H., Tramel, R.W., and Buning, P.G., “Evaluation of Two High Order WENO Schemes,” AIAA-2007-3920, June 2007.
- <sup>16</sup>Nicols, R.H., “A Comparison of Hybrid RANS/LES Turbulence Models on a Circular Cylinder at High Reynolds Number,” AIAA-2005-498, Jan. 2005.
- <sup>19</sup>Nicols, R.H., “A Comparison of Hybrid RANS/LES Turbulence Models for a Generic Weapons Bay With and Without a Spoiler,” AIAA-2008-6229, Aug. 2008.
- <sup>20</sup>Tramel, R., Rock, S., Ellis, J., and Sharpes, D., “Comparison of Large Cavity Aeroacoustic Computations with Flight Test Results,” AIAA-2005-2800, May 2005.